Università degli Studi di Firenze
Dipartimento di Fisica e Astronomia

Scuola di Dottorato in Scienze
Dottorato di Ricerca in Fisica - XXIII ciclo
SSD FIS/03 Fisica della Materia

Dissertation in Physics

to Obtain the Degree of

Dottore di Ricerca
in Fisica

Title:

Development of a Transportable Strontium Optical Clock

presented by

Marco Schioppo

Supervisor Guglielmo M. Tino

Coordinator Alessandro Cuccoli

December 2010

Contents

Introduction

New kinds of clocks are today revolutionizing time keeping with enormous consequences for science and technology. They are called "optical clocks" and they are a new generation of atomic clocks based on optical transitions. This thesis describes the design and the ongoing realization of the first transportable optical clock based on neutral laser-cooled strontium atoms trapped in an optical lattice. Transportability is the key feature to take full advantage of the expected performance allowing a wide range of applications on Earth and also in Space in the near future. A transportable optical clock can be used on Earth to characterize other optical clocks placed in stationary laboratories, toward the future re-definition of the SI second based on optical standard. Future space optical clocks can test the general relativity at an unprecedented precision level, measure the gravitational redshift and map the gravitational Earth field. Additionally they can provide many technological applications such as a new type of relativity-based-geodesy and a new generation of high precision navigation and positioning systems. Strontium is one of the best candidates for these applications as it is the most mature within the optical lattice clocks with many clock-laboratories under development around the world. In order to move from the laboratory systems of today to space-qualified instruments the key challenge of this work has been to outline the main physical and technological requests for a transportable optical lattice clock and match them with novel solutions. Design and characterization have been mainly focused on the production of cold strontium atoms that represent the core of an optical lattice clock. A transportable laser-cooled strontium source has been completed and characterized, it can provide a sample of about 10^7 atoms at $1\,\mu$K temperature. Novel approaches and solutions to reduce dimension, weight and power consumption of the experimental setup, maintaining a high level of operation reliability, are presented in detail. This activity is part of an european project called "Space Optical Clocks" funded by the *European Space Agency* (*ESA*).

The contents of this thesis are organized as following:

Chapter 1 provides an historical background of the evolution of time measurement. Optical clocks are presented together with the their wide range of applications and the request of a transportable version is also discussed.

Chapter 2 introduces theoretical concepts for laser cooling and trapping of neutral atoms.

Chapter 3 presents the operating principle of a strontium optical lattice clock. The strontium atom and its peculiar features are discussed. The theoretical background introduced in the previous chapter is here applied to this kind of atom.

Chapter 4 is dedicated to the transportable system for ultra-cold strontium production. Design and realization of each component are shown in detail. Novel solutions adopted to reduce volume, mass and power consumption are also presented.

Chapter 5 presents the preliminary experimental results achieved with the transportable setup.

Chapter 1

Introduction to Optical Clocks

1.1 Historical Background

The measurement of time has always been fundamental in the mankind's everyday life. A clock is what does this measurement by "keeping time" in terms of time units or cycles of periodic phenomena. Any physical phenomenon that repeats itself with a certain constant frequency ("oscillator") can be used to measure time intervals by counting and keeping track of the occurred number of cycles. Thus, a clock is essentially composed by two main parts: an *oscillator* and a *counter* which keeps track of the oscillator cycles (see Fig.1.1).

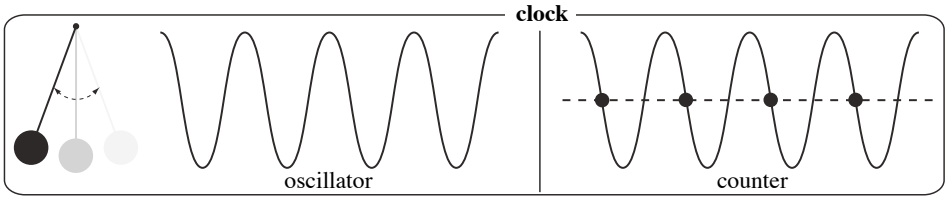

Figure 1.1: Conceptual scheme of a clock.

1.1.1 Astronomical and Mechanical Era

There are many periodical phenomena in nature that can be used as oscillators. The most common and ancient is provided by the motion of the Earth and the Sun. When ancient people put a stick in the ground to observe the movement of its shadow from sunrise to sunset and marked off "noon" they implemented the counter and hence the first clock of human history, the

sundial (see Fig.1.2). Measuring the time with astronomical events has been a natural technique to synchronize on time scales of months, days or even hours important human activities like agriculture, trade and religious practices. Unfortunately the operation of these early clocks depended on weather conditions and in order to overcome this limit the first man-made clocks were developed (see Fig.1.3). Initially they were based on sand and water flow and they were used to interpolate or keep track of time between astronomical checks (between sunset and sunrise for example). In centuries with the increasingly complexity of the human activities hourly precision became insufficient. The basic concept to improve the resolution of time keeping is to use a periodic event which occurs more frequently, such that the time can be divided into smaller intervals. For this purpose, in the 14th century, first all-mechanical clocks were built. They were based on "verge-escapement" mechanisms powered by a weight attached to a cord and they had an oscillation frequency higher than that of sand or water clocks keeping time to within about 15 minutes a day. But no two clocks kept the same time because the frequency was very dependent upon the friction between parts, the weight that drove the clock, and the exact mechanical arrangement of the parts of the clock. What was needed was some sort of periodic device whose frequency was essentially a property of the device itself and did not depend on external factors. In the 17th century, the Galileo pendulum was found to be such a device by the scientist Christian Huygens. His pendulum clock was accurate within 10 seconds a day, a dramatic improvement over the "verge-escapement" clock.

Figure 1.2: The sundial, the first clock of human history.

With the development of the navigation across uncharted oceans further improvements in time keeping became necessary in order to localize ships. In particular there was the crucial need to have a clock aboard ships telling the accurate time at Greenwich, England, in order to find their position east or west of the zero meridian. The pendulum clock had been an enormous improvement but it was no use at all at sea since the rolling and pitching of the ship made it inoperative. A different approach was needed and it was the English clock maker John Harrison who, in 1761 successfully tested the first marine chronometer based on a "balance-spring" mechanism, showing to keep time with accuracy within 1 second a day, enough to precisely determine longitude. After these successes many further refinements were made

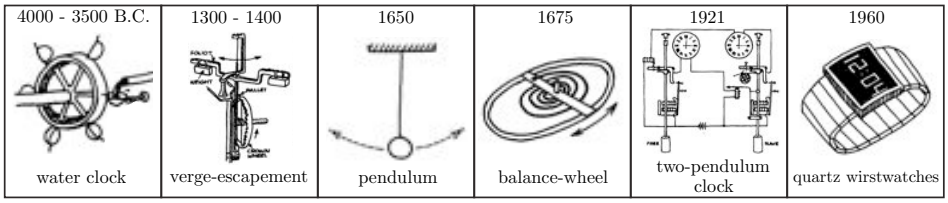

Figure 1.3: Evolution of mechanical clocks [1] .

to pendulum reaching the limit of this technology in 1921 with the “two pendulum clock” developed by William Hamilton Shortt. This type of clock kept time within 1 millisecond per day. Nevertheless the pendulum clock could not be used as an absolute timescale because of its limited reproducibility in design and implementation. In fact the period of the pendulum depends upon its length. Even if clocks makers could agree on a fixed length, limited tolerances in length measurements, machining and thermal expansion limits the reproducibility of the oscillation period in different clocks.

The first big step in a new direction was taken by the American scientist Warren A. Marrison with the development of the quartz-crystal clock in 1929. The operation of this new clock is based on the natural piezoelectric quality of quartz crystal that resonates, or “ring”, with a frequency that depends on its dimensions, producing a voltage across points of its surface. If it is placed in on oscillating electric circuit that has nearly the same resonant frequency, the crystal will vibrate at its natural frequency, and the frequency of the circuit will become the same as that of the crystal. The internal friction of the quartz crystal is so very low that the crystal’s vibration may range from a few thousand to many millions of cycles per second, depending on how it is cut. The best crystal clocks can keep time within less than 1 millisecond per month. Billions of quartz oscillators are manufactured annually for use inside clocks, watches, cell phones, computers, radios, and nearly every type of electronic circuit. Even so, quartz oscillators are not ideal frequency standards. Their resonance frequency depends on the size and shape of the crystal and no two crystals can be exactly alike or produce exactly the same frequency. In addition, the frequency of a quartz oscillator changes slowly over time due to aging, and can change more rapidly due to environmental factors, such as temperature, humidity, pressure and vibrations. These limitations make them unsuitable for being a “time standard” and the quest for better accuracy has led to the development of a new kind of clocks called “atomic clocks".

1.1.2 Quantum Revolution

In the last century, with the discovery and development of quantum mechanics came the possibility of using oscillators more precise than any mechanical or celestial reference previously known to man. These oscillators are based on atoms and molecules. The laws of quantum mechanics dictate, indeed, that atoms and molecules can have only certain discrete values of energy and they can make transitions between two different energy levels (E_1 and E_2) by absorption or emission of energy in the form of electromagnetic radiation having the precise frequency

$$\nu_0 = \frac{|E_2 - E_1|}{h} ,$$

where h is the *Planck* constant. In many atomic systems, the energy levels are very insensitive to external perturbations, such that the radiation frequency ν_0 is robust and reliable. On the basis of these considerations the basic principle of an "atomic oscillator" is simple: an opportune robust and reliable natural transition frequency ν_0 serves as a reference to which a laboratory radiation source, with frequency ν, can be compared and stabilized. The architecture of an atomic clock is then completed by a counter that keeps track of the oscillations of the stabilized frequency (see Fig.1.4). The enormous advance of using an atomic frequency standard is that the clock frequency should be independent of the man-made components of the oscillator. Every copy of a given atom is identical, such that a clock using a certain atom will operate at the same frequency as an independent clock based on the same atom placed anywhere in the universe. In a word this means that, once defined the kind of atom and the clock transition, this clock can be used as a "time standard".

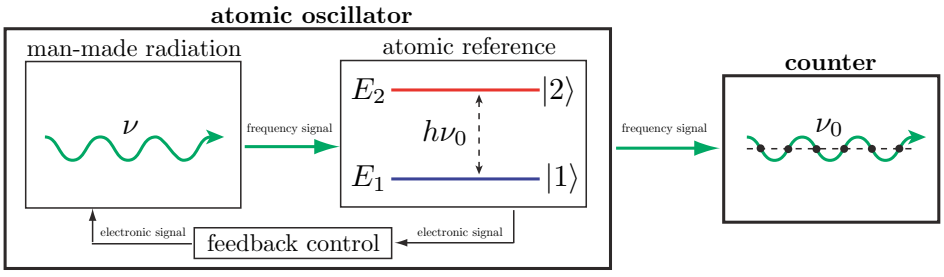

Figure 1.4: Architecture of the atomic clock.

1.1.3 Clock Performance

To better understand the evolution of atomic clocks and their application as "time standard" it's necessary to introduce some basic concepts that are used to measure their performance.

Quality Factor (Q)

The concept of "Quality Factor" or "Q" is referred to oscillators. An ideal oscillator would be one that, given a single initial push, would run forever. But of course this is not possible in nature; because of friction everything eventually runs down. Some oscillators, however, are better than others, and it is useful to have some way to discriminate their performance. One such measure is provided by Q, that is defined as

$$Q = 2\pi \cdot \frac{\text{energy stored}}{\text{energy dissipated per cycle}} \ .$$

A damped oscillator has the following equation of motion:

$$m\ddot{x} + b\dot{x} + kx = 0 \ ,$$

where m is the mass of the oscillating body, x is its position, b is the damping coefficient and k is the spring constant.

In the "underdamped regime" ($\omega_0 \tau > 1$) the solution has the form

$$x(t) = Ae^{-t/\tau} \cos(\omega_0 t + \phi) \ ,$$

where $\tau = 2m/b$ is the decay time, $\omega_0 = \sqrt{k/m}$ is the resonance frequency, and A and ϕ are given by the initial conditions. Applying the definition of

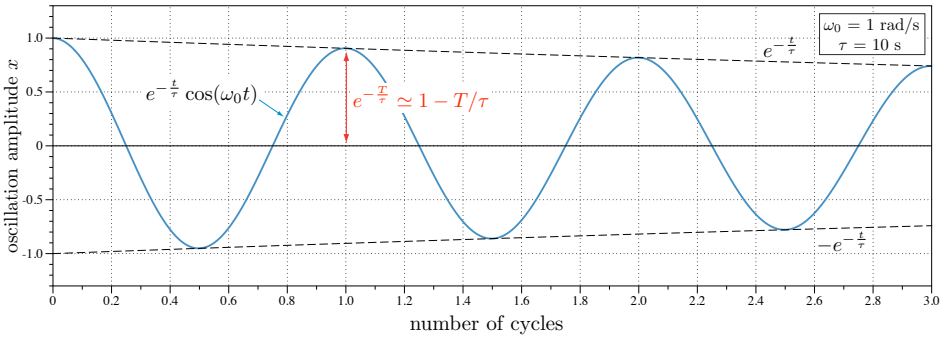

Figure 1.5: Damped oscillator in the "underdamped regime" ($\omega_0 \tau > 1$).

Q we find:

$$Q = 2\pi \frac{x(0)^2}{x(0)^2 - x(T)^2} = 2\pi \frac{1}{1 - e^{-2T/\tau}} \simeq \omega_0 \cdot \frac{\tau}{2} \,, \tag{1.1}$$

with period $T = 2\pi/\omega_0$ (see Fig.1.5). Eq.1.1 points out that Q is related to the decay time of the oscillator; the longer the decay time (or equivalently the smaller the friction), the higher the Q. One of the obvious advantages of a high-Q oscillator is that we don't have to perturb its natural or resonant frequency ($\nu_0 = \omega_0/2\pi$) very often with injections of energy. But there is another important advantage in terms of frequency response. Consider a damped oscillator in terms of its energy spectral density

$$\mathcal{E}(\omega) \propto \left| \int_0^{+\infty} x(t) e^{-i\omega t} dt \right|^2 \propto \frac{1}{(\omega - \omega_0)^2 + (1/\tau)^2} \,;$$

its frequency spectrum is described by a Lorentzian function with a "full width half maximum" $\Delta\omega$ given by

$$\Delta\omega = \frac{2}{\tau} \,, \tag{1.2}$$

showing that there is an exact relation between the decay time and the sharpness of the resonance curve (see Fig.1.6). Equations (1.1) and (1.2) provide, hence, another important meaning of Q, summarized by the expression

$$Q = \frac{\omega_0}{\Delta\omega} \left(= \frac{\nu_0}{\Delta\nu} \right) \,, \tag{1.3}$$

indicating that, in terms of frequency response, high Q oscillators have sharply peaked resonance curves. So the big advantage to have a high-Q

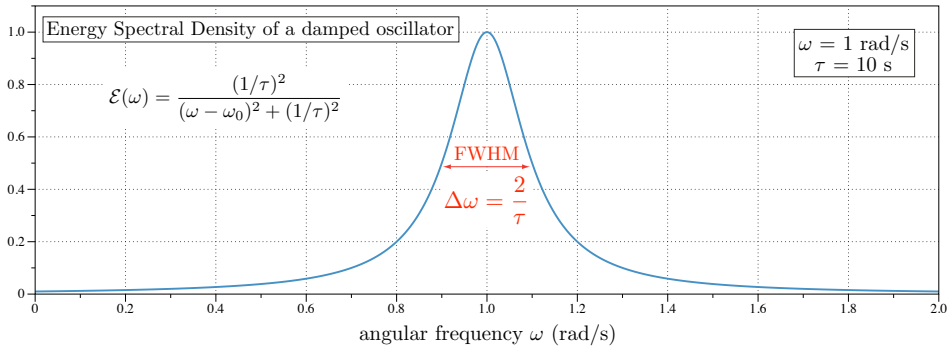

Figure 1.6: Energy spectral density of a damped oscillator.

oscillator is that it doesn't want oscillate at all unless it is swinging at or "near" (within the frequency bandwidth $\Delta\nu$) its natural frequency ν_0. This feature provides an important rule to choose the atomic reference: atoms with a high frequency transition and a narrow linewidth are needed. Together with Q, there are two other important quantities to fully characterize the performance of an atomic clock: *accuracy* and *stability*.

Accuracy

The accuracy of an atomic clock is determined by how well the measured frequency matches that of the atoms natural frequency ν_0. In general, the accuracy will depend on the atomic species used and on how well it can be isolated from environmental effects during spectroscopy.

Stability

Stability represents the repeatability of the measured clock frequency over a given averaging time τ. This is typically given in terms of the fractional frequency instability which at the ultimate limit set by the quantum-projection-noise (QPN) has the expression [2, 3, 4]

$$\sigma_y(\tau) \propto \frac{1}{Q}\sqrt{\frac{T_c}{N_{at}\tau}}\,, \tag{1.4}$$

where τ is the averaging time in seconds, N_{at} is the number of interrogated atoms, T_c is the clock cycle duration ($T_c < \tau$) and Q is the quality factor of the transition. From this expression we see that atomic clocks will generally benefit from operating at high-Q atomic transitions (high frequency and narrow linewidth) and from a high number of interrogated atoms.

An accurate clock is necessarily stable over long intervals, but not all stable clocks are accurate (see Fig.1.7).

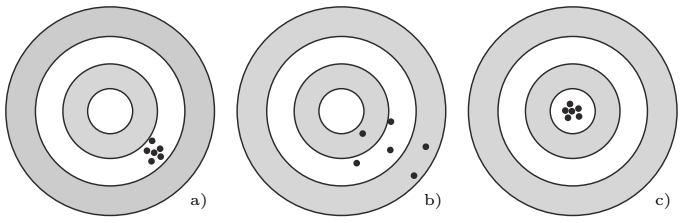

Figure 1.7: Examples of stability without accuracy (a), no stability and no accuracy (b), stability with accuracy (c).

1.1.4 Microwave Clocks and the SI second

The first atomic clocks were based on atomic transitions in the microwave region of the frequency spectrum because of the development of the microwave electronics before and during the Second World War. They provided a major breakthrough in both accuracy and stability, easily surpassing the performance of all previous standards (see Fig.1.8). In particular, by the early 1950's, work had begun in several national laboratories to build atomic frequency standards based on cesium. Cesium, in fact, has several properties that made it a good choice as the source of atomic resonance for a primary standard. Cesium atoms are relatively heavy (133 amu), and, as a result, they move at a relatively slow speed of about 130 m/s at room temperature. This allows cesium atoms to stay in the interaction zone with the interrogation microwave field longer than hydrogen atoms, for example, which travel at a speed of about 1600 m/s at room temperature. Cesium also has a relatively high hyperfine frequency ($\sim$ 9.2 GHz) when compared to atoms used in other atomic oscillators, such as rubidium ($\sim$ 6.8 GHz) and hydrogen ($\sim$ 1.4 GHz). In 1955, the first cesium clock was realized in England, at the National Physical Laboratory (NPL), obtaining an inaccuracy of 1×10^{-9}. The unrivaled precision and accuracy in time keeping provided by the Cs clocks led to a new definition of time in 1967. The second is now defined as "the duration of 9,192,631,770 periods of the radiation corresponding to the transition between the two hyperfine levels of the ground state of the

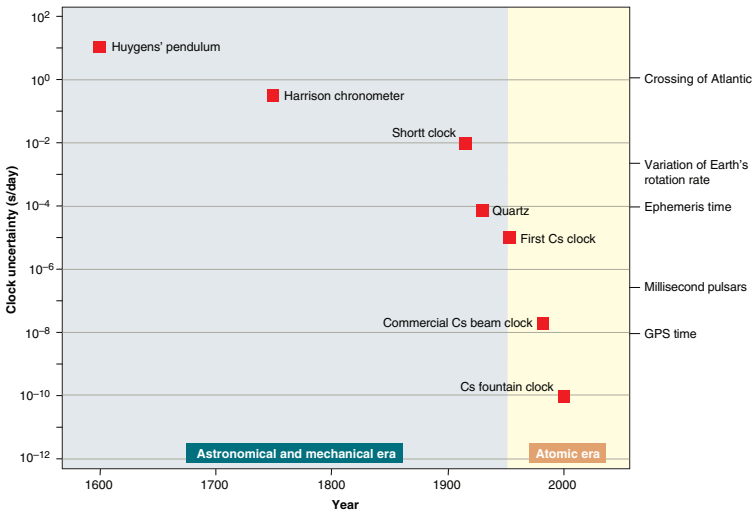

Figure 1.8: Evolution of clocks performance over the past 400 years [5].

caesium 133 atom" [6]. The use of atomic clocks has made the second the most accurately realized unit of measurement, such that many other units are now being defined in terms of time like the meter, the ampere and the candela for example.

After more than 50 years of development [1, 5, 7], the cesium fountain clocks of today [8, 9, 10] are now approaching an incredible (in)accuracy level of a few parts in 10^{16}. Such a clock is able to keep time losing only one second every 100 million years!

1.2 Optical Clocks

Although the accuracy of present-day microwave clocks is already very high, outstanding advances in laser and quantum technology have opened the way to a new approach to time-keeping based on optical atomic transitions. Because optical frequencies ($\sim 10^{15}$ Hz) are much larger than microwave frequencies ($\sim 10^{10}$ Hz), optical clocks hold the potential of being enormously more accurate and stable than the cesium clock. The advantages of optical clocks due their potential high-Q level (assuming a linewidth $\Delta\nu$ comparable with that achieved by microwave standards) were recognized in the early days of frequency standards, but several crucial steps have occurred to realize them. First of all, a coherent light source was needed to interrogate the atomic transitions. So only after the first demonstrations of lasers in early 1960s [11] and with advent of tunable lasers came the possibility to perform high-resolution spectroscopy of atoms and molecules, today also throughout the visible spectrum. Another important step has been the development of laser cooling techniques that made possible to use the light-matter interaction to cool a variety of atoms and ions to milli-Kelvin temperature and below [12, 13, 14]. Laser cooling is fundamental to reduce the Doppler shifts in frequency response of atoms and ions due to their finite velocity along the direction of the interrogation light and enables the extended interaction times required to observe a narrow transition linewidth. Finally there is the readout of the optical frequency. This operation is very difficult since optical oscillation is orders of magnitude faster than electronics can measure. Historically the first measurements of optical frequencies were realized by using a long chain of phase-locked oscillators that scaled optical frequencies down to the measurable microwave domain. These frequency chains took up whole rooms and required a number of skilled people to operate them [15]. Only in the last few years, the development of self-referenced optical

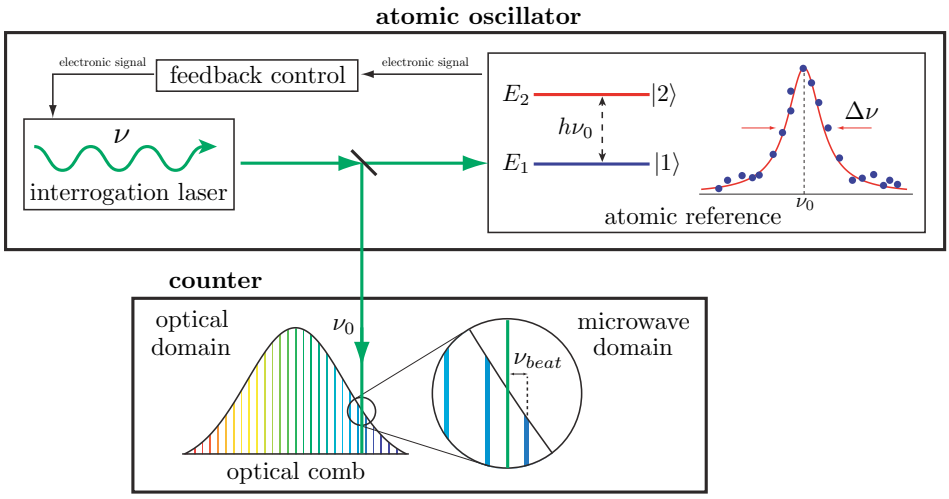

Figure 1.9: Schematic view of an optical clock.

synthesizers (frequency combs) allowed in one step the precise comparison of frequencies ranging from the microwave domain to the visible and ultraviolet domain providing a coherent link between these different frequency regions [16, 17, 18, 19, 20]. Today, optical frequency measurements can be performed with a single optical synthesizer that takes up less than one square meter of space and with little operator input. The general design of an optical clock of today is shown in Fig.1.9. Here the light produced by the interrogation laser is used to probe an electromagnetic resonance ν_0 in an atom (or molecule or ion). The laser frequency is then actively kept on the center of the absorption resonance by a feedback control loop, acquiring the stability of the atomic transition. The laser frequency so stabilized is sent to an optical comb. By beating the laser frequency with one of the comb's teeth it is possible to transfer from the optical to the microwave domain the counting of the absolute frequency ν of the stabilized laser.

The advances in laser technology, laser cooling and optical combs have provided a fundamental boost to the realization of many kinds of optical atomic clocks (see Fig.1.10) within an increasing number of laboratories spread around the world. In particular we can distinguish among three types of optical atomic clock: free falling neutral atoms clocks (Ca, Mg), single trapped ion clocks (In^+, Sr^+, Al^+, Hg^+, Yb^+) and finally optical lattice clocks (Sr, Yb, Hg).

Free falling neutral atoms clocks, although having demonstrated excellent stability and reproducibility, offer a limited interaction time thus limiting the

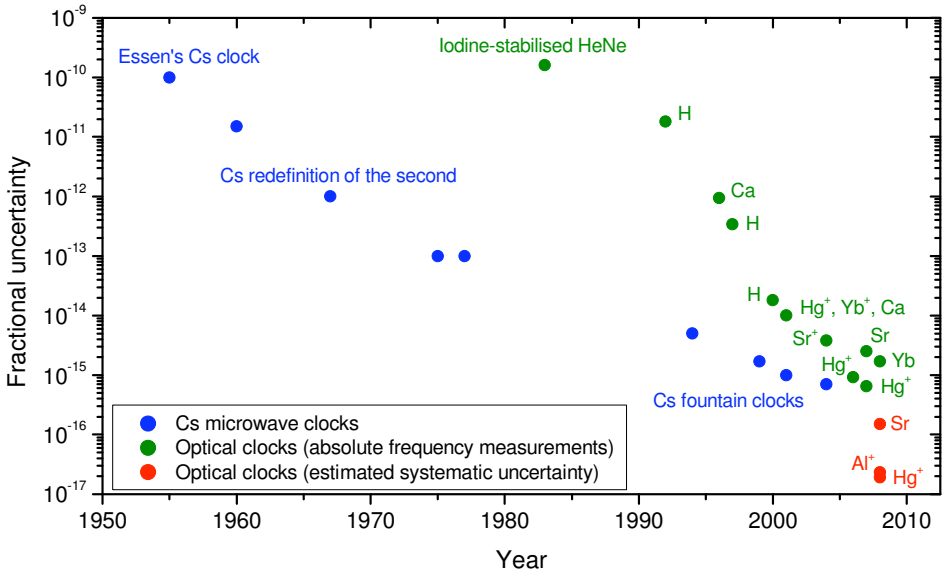

Figure 1.10: History of optical and microwave atomic frequency standards. Optical clocks started to progress rapidly with the development of optical frequency combs around the year 2000. The red points represents the last optical clock achievement reported in [21, 22]

effective Q. More importantly their accuracy is limited because of Doppler and recoil frequency shifts.

References based on single ion trapped in Paul RF quadrupole traps do not suffer of Doppler and recoil frequency shifts and have already demonstrated a fractional systematic frequency uncertainty at the 10^{-17} level [22] and below [23]. Although this kind of clocks has a very low signal-to-noise ratio because of the limited number of interrogated atoms ($N \sim 1$), optical clocks based on this technology have today the best fractional accuracy.

Finally, following the scheme of the high accuracy ion clocks, neutral atoms can be tightly trapped in an optical lattice, combining the benefit of long interaction time with that of high number of interrogated atoms. The optical trap can be carefully designed such that the AC Stark shifts induced by the lattice field can be canceled, leading to very low quantum noise instability and lattice shift uncertainty [24, 25, 26]. Clocks based on this scheme are called “optical lattice clocks". They have already provided demonstrations of uncertainty at the 10^{-16} fractional level [21, 27] and they have the potential to reach the highest levels of accuracy and stability [28]. The study of this kind of atomic clocks together with their possible applications are the starting points of this thesis.

1.3 Importance of Atomic Clocks Today

Atomic clocks are fundamental tools in modern society. They are essential in science, they have also many practical applications in our everyday life, and are even present in satellites, especially for navigation systems such as GPS. Each of the twenty-four GPS satellites has onboard an atomic clock that transmits synchronized coded signals so that any observer receiving and analyzing these signals from four or more satellites can determine his position to within 20 meters with inexpensive receivers. Much better results can be achieved by using dedicated receivers and by averaging the measurements over long time with an impressive capability to locate the position of a stationary object with 1 mm of accuracy. This incredible positioning capability of GPS has revolutionized navigation of airplanes, boats and even personal cars. The atomic clock based timing of GPS signals regulates many of our everyday systems providing the synchronization of large-scale electric power grids, cell phone networks, large computer networks for banking and the internet.

Atomic clocks are also powerful tools for a large range of scientific fields. For instance the positioning capability of GPS is providing great benefits to all Earth sciences and in particular to study the Earth's crustal dynamics and continental drift.

The possibility to use optical clocks to precisely synchronize data signals coming from different places is applied to radio astronomy to synchronize different radio telescopes placed in different places on Earth looking at the same star. This approach, called "Very Large Baseline Interferometry", allowed to reach an effective angular resolution equivalent to have a single telescope with an aperture diameter of the size of the Earth.

Precision spectroscopy is another scientific field tightly linked to the development of atomic clocks. Indeed, to push the limits of clock performance, new spectroscopic techniques and technologies have been developed, like for instance laser cooling and optical combs. Furthermore many of the technical advances for making better atomic clocks have been directly applied to the improvement of the spectroscopy techniques.

Pushing time measurements to new limits is leading also to a profound impact on fundamental research. The new generation of atomic clocks, optical clocks, offers indeed a powerful tool for investigating the two main theories of the XX$^{\text{th}}$ century: general relativity and quantum theory. The fact that these two theories are notoriously difficult to conciliate makes opti-

cal clocks even more important for fundamental research. For example, some modern cosmological models imply that fundamental constants had different values in the early Universe, and that they might still be changing. Optical clocks have been recently used to provide upper limits on present-day variations of fundamental constants with an unprecedented level of precision [29, 22].

1.4 Transportable Optical Clocks

The unprecedented accuracy and stability level offered by optical clocks makes them very difficult to fully characterize. The performance of a single atomic clock is indeed unprovable in absence of an absolute reference with the same or higher level of performance. The only solution is to build a second clock as good as the first. This is exactly what many groups are doing today, by comparing different optical clocks placed in the same metrology laboratory or up to kilometers away. The link between optical clocks is not trivial, since it doesn't have to limit their performances. Nevertheless many advances have been recently made, showing the possibility of using standard telecommunication optical fibers to compare remote optical clocks and disseminate optical frequencies over hundreds of kilometers [30]. This approach is very rapidly developing but still remains a technological and scientific effort.

In this thesis we want to discuss a different approach. Here is proposed and partially realized the first prototype of transportable optical clock. The idea is to use this apparatus as an "optical clock tester", moving it to other stationary optical clocks placed in metrological laboratories around the world. One of the motivations of this work is indeed to provide a new tool to make comparison campaigns between different optical clocks. In this way it is possible to verify the effective reproducibility of different optical frequency references and to collect all the technological and scientific informations needed for the future redefinition of the SI second, based on optical standards.

Strontium atoms seem to be good candidates for this application, because of their easily accessible transitions of interest, mostly covered by commercial laser diodes. This fact has led strontium clock to become the most mature of lattice clocks in terms of technological readiness and scientific results, with many strontium clocks under development around the world [31, 32, 33, 21, 34, 35, 36, 37].

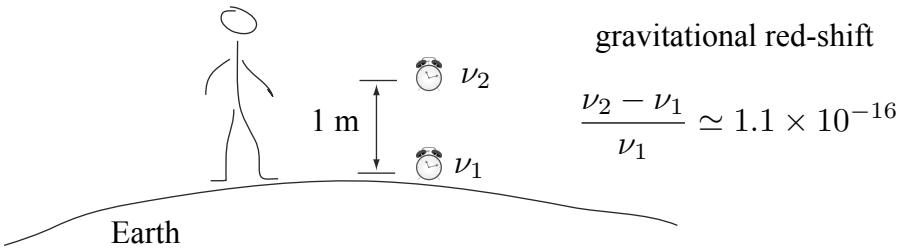

Figure 1.11: Illustration showing how new kinds of clocks with fractional frequency inaccuracy below 10^{-16} can be used to measure the time delay due to the gravitational redshift at a personal scale of less than one meter.

In a recent demonstration, a strontium lattice clock has achieved an absolute fractional frequency uncertainty (for ^{87}Sr) at 1×10^{-16} level [21]. This level of precision opens the way to new kind of applications, since the effects of general relativity, that mix time with gravity, previously measured by comparing clock on Earth's surface and a high-flying rocket [38], start now to be observable at a personal scale of meters and centimeters [39]. For example, two identical clocks with equal frequency ν, placed on Earth at 1 meter different elevations (see Fig.1.11), corresponding to a variation of gravitational Earth potential of

$$\Delta U = U(R_\oplus + 1\,\mathrm{m}) - U(R_\oplus) \simeq g \cdot 1\,\mathrm{m} \simeq 9.8\ \mathrm{J/Kg}\ ,$$

(where $R_\oplus$ and g are respectively the mean radius of the Earth and the gravitational acceleration) experience a gravitational red-shift given, in the post-Newtonian approximation (PPN), by the expression

$$\frac{\nu(R_\oplus + 1\,\mathrm{m}) - \nu(R_\oplus)}{\nu} = \frac{\Delta U}{c^2} \simeq 1.1 \times 10^{-16}\ , \tag{1.5}$$

where c is the speed of light in vacuum. The equation (1.5) shows that the clock placed 1 meter above goes faster by about 1 part in 10^{16}, that is at same level of the up-to-date precision of strontium lattice clocks. This can open new fields of application like a new kind of relativity-based-geodesy. In this scenario a transportable optical clock can be used to map the gravitational field of the Earth by comparing its frequency with that of the closest identical stationary optical clock. Strontium could be a good choice for this application mostly because of the already proven high level of agreement upon different strontium optical references developed in independent laboratories [29]. This fact makes the Sr lattice clock a promising candidate for future redefinition of the SI second with an expected increasingly

number of such frequency references available for comparison measurements with a transportable Sr clock. For this kind of application the possibility to link a transportable optical clock with stationary systems by using standard telecommunication optical-fiber infrastructures is essential, for this reason transportable clocks and optical links for the dissemination of clock frequencies have to be developed in parallel.

1.5 Future Optical Clocks in Space

The performance of optical clocks has strongly improved in recent years, and accuracies and instabilities of 1 part in 10^{18} are aspected in the near future. The operation of such clocks on Earth's surface, because of gravitational redshift, will be unavoidably dependent on their elevation (as has been recently shown by comparing two Al^+ clocks in [39]) on a length scale given by:

$$\delta z = \underbrace{\frac{\Delta\nu}{\nu}}_{10^{-18}} \cdot \frac{c^2}{g} \simeq 1\,\mathrm{cm}\,.$$

This means that to compare two clocks to a part in 10^{18} is necessary to know their altitudes with 1 cm of precision. More precisely, what are actually needed are not the clock altitudes, given by their distances to mean sea level, but their distances to the geoid, that is defined as the hypothetical surface of constant gravitational potential. The main problem is that the Earth's geoid doesn't lie at rest but it fluctuates on centimeter scale because of a number of processes as solid Earth tides, oceanic tides, effects of atmospheric pressure on ocean levels and redistribution of water due to climate changes [40] (see Fig.1.12a). Additionally other longer-term effects as glacial melting and the drift of tectonic plates introduce further uncontrollable fluctuations. Indeed the comparison at a part in 10^{18} of two future optical clocks placed in two different tectonic plates will be sensitive to the doppler effect due to their relative velocity starting from a minimum drift velocity given by

$$v_{\min} = c \cdot \underbrace{\frac{\Delta\nu}{\nu}}_{10^{-18}} \simeq 1\ \mathrm{cm/year}\,. \tag{1.6}$$

The relative drift velocity of the plates varies but is typically 0-10 cm per year (see Fig.1.12b), so can be higher than the minimum sensitivity-threshold given by the eq.1.6, thus limiting the comparison of future optical clocks. Together, all these effects cause the rates of frequency standards and clocks to

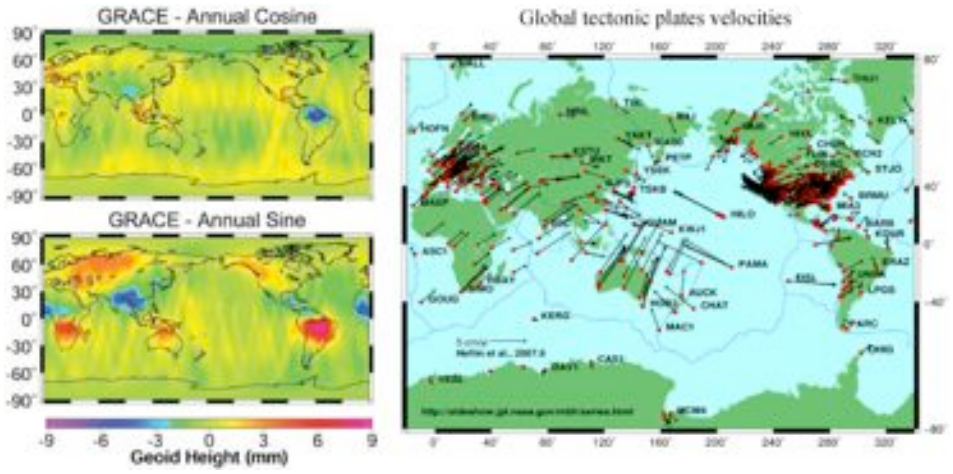

a) b)

Figure 1.12: a) Comparison of annual variation in the Earth's geoid height estimated by the twin Gravity Recovery and Climate Experiment (GRACE) satellites [40]. The cosine (i.e., winter-summer) and sine (i.e, spring-fall) Earth's geoid height is shown as a function of geographic location. The annual cycle geoid variation is up to 10 millimeters in some regions, predominantly peaked in the spring and fall seasons. b) Global tectonic plates velocities determined by measuring the position variation of over 1000 GPS stations. Data have been analyzed at the Jet Propulsion Laboratory, California Institute of Technology [47]. Horizontal velocities, mostly due to motion of Earth's tectonic plates and deformation in plate boundary zones, are represented on the maps by arrows extending from each site.

uncontrollably fluctuate by several parts in 10^{17} [41]. In other words Earth has a too much noisy "space-time environment" to take full advantage of the performances expected by near future optical clocks. A much cleaner environment is offered by Space instead, where spatial and temporal variations of the Earth's gravitational field can be smoothed out by using high altitude orbits and where otherwise these effects can be determined with high precision by continuously measuring the orbit parameters [42, 43, 44, 45]. The operation in Space of future optical clocks opens a new scenario for technological applications and scientific research [46].

- **Accurate time-keeping:** a future Earth-orbiting optical clock can be used as "master clock" for distribution of time and frequency on Earth. Such a clock will provide the means to compare and synchronize the highest performance clocks on Earth in order to create an international optical atomic time scale.

- **Earth Observation:** an unprecedented high-precision mapping of the Earth's gravity field will be possible by frequency comparison of terrestrial transportable clocks with a master space clock. The sensitivity of space optical clock-based geodesy will make possible to monitor the motion of the surface of the Earth with such outstanding precision that a new level of understanding, and possibly, prediction, of geophysical effects may be obtained, including earthquakes and volcano eruptions.

- **Navigation:** arrays of orbiting optical atomic clocks may be used to realize a future global satellite-based navigation system with a potential improvement in position prediction precision of up to two-three orders of magnitude. Such a future optical-clock based navigation system would revolutionize the positioning of planes, boats and individual persons, but also the navigation of probes in deep Space.

- **Fundamental physics:** space optical clocks can provide a powerful tool to test the limits of the two fundamental theories that have revolutionized our understanding of the universe: general relativity and quantum mechanics. In particular the comparison of one space optical clock on a highly elliptical orbit, with a second optical clock located on Earth, would allow an unprecedented precision level test of gravitational redshift (mission concept EGE [48]). Such a test is devoted to verify the Einstein's Theory of General Relativity and to search for eventual deviations or hints of quantum effects in gravity, providing the first experimental evidence to support emerging theories aimed at unifying all fundamental forces of nature.

1.6 The "Space Optical Clocks" (SOC) project

In order to fill the gap between clock laboratory systems of today and future space-qualified optical clocks, in 2004 an European team including our group in Florence proposed to *European Space Agency* (ESA) a project for the first experimental study of the feasibility of optical clocks for space applications. Following evaluation, this project, called "Space Optical Clocks" (SOC), has been funded by ESA and it started in 2007-2008. SOC is a 3-year project and concentrates on optical lattice clocks of neutral strontium and ytterbium atoms [49]. The project included both activities on laboratory (stationary) lattice clocks as well as on the development of completely new hardware for a transportable lattice clock. The work done in this thesis represents my personal contribution to this latter part of the SOC project. In particular the design and realization of a transportable apparatus to produce a sample of ultra-cold strontium atoms is here presented. The main requests of compact design, low power consumption and operation reliability have been matched by using novel solutions [50]. The main goal of the SOC project is the development of a fully transportable optical clock by means of the integration of the subsystems built by each member of the team. All this work will provide important technological and scientific informations toward a near-future engineered optical lattice clock for application on Earth and in Space.

Chapter 2

Laser Cooling and Trapping of Neutral Atoms

The possibility of using neutral atoms as frequency references depends on the capability of experimentalists to manipulate them and to access to their natural spectral features avoiding any disturbing effects as frequency shift and broadening. In the ideal case a sample of atoms is at rest in the laboratory reference frame, corresponding to an absolute temperature of the atomic sample approaching to the zero Kelvin limit. In contrast, at room temperature ($\mathrm{T} \simeq 300\,\mathrm{K}$) atoms move with a most probable velocity v_0 given by

$$v_0 = \sqrt{\frac{2k_B T}{M}}\ , \tag{2.1}$$

where k_B is the Boltzmann constant and M is the atomic mass. The finite temperature and hence the finite velocity of atoms with respect to laboratory causes a number of undesirable effects.

First of all, the motion of an atom along the direction of an incoming interrogation light leads to a shift in the measurement of the natural angular frequency $\omega_0 = 2\pi\nu_0$, given by the Doppler shift

$$\omega_0' = \omega_0 + \mathbf{k}\cdot\mathbf{v}\ ,$$

with ω_0' natural angular frequency measured in the laboratory frame of reference, $\mathbf{v}$ velocity of the atom with respect to the interrogation light, $\mathbf{k}$ wavevector of the interrogation light.

Additionally, the finite velocity v of an atom, crossing perpendicularly a probing laser beam with diameter d, limits the light-atom interaction time

τ, leading to a *transit-time* frequency broadening $\Delta\nu_{tt}$ given by

$$\Delta\nu_{tt} \simeq \frac{1}{\tau} = \frac{v}{d} \tag{2.2}$$

that can cover the natural width $\Delta\nu_0$ of the transition, thus limiting the effective Q factor (eq.1.3) of the transition ($Q_{\text{eff}} \sim \nu_0/\Delta\nu_{tt}$).

Finally, a sample of atoms at certain finite temperature T has a Maxwellian velocity distribution given by

$$f(v)dv = \frac{1}{v_0\sqrt{\pi}} \exp\left(-\frac{v^2}{v_0^2}\right) dv \ ,$$

where $v_0 = \sqrt{2k_{\text{B}}T/M}$ is the most probable velocity and $f(v)dv$ provides the number of atoms with speed in the range v to $v + dv$. In presence of an interrogation radiation each velocity class of the atomic sample has a frequency response given by the Doppler shift of eq.2.1. It results that the total frequency response has a Gaussian line shape function with a Doppler-broadening (full width half maximum) given by

$$\frac{\Delta\nu_{\text{D}}}{\nu_0} = 2\sqrt{\ln 2} \cdot \frac{v_0}{c} \ . \tag{2.3}$$

In conclusion to access to the natural linewidth of atomic transition and to avoid any shift it's necessary to cool and trap atoms. Neutral atoms are very difficult to manipulate because are insensitive to stationary electric fields. The dramatic development of laser technology has provided, since the 1980s, a new powerful tool to control the atomic motion by using the atom-light interaction. In particular two kinds of so called "radiative forces" can be distinguished: dissipative force (scattering force) and conservative force (dipole force) [51, 52, 53].

2.1 Dissipative Force (Scattering Force)

Let's consider a simplified atom with only two quantum states in presence of resonant photons. It follows from the conservation of momentum that when the atom absorbs a photon and goes into the excited state, it takes the momentum

$$\Delta p = \hbar k_L \ ,$$

where k_L is the photon wavevector. Immediately after the atom absorbs a photon it cannot absorb another until it emits a photon by spontaneous

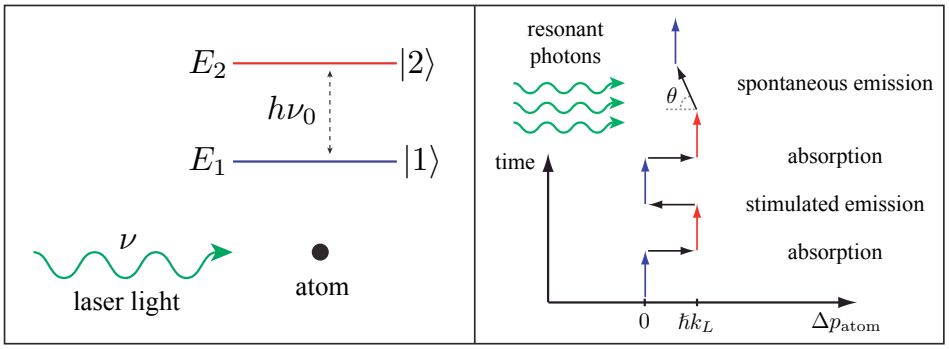

Figure 2.1: Operating principle of the scattering force. An atom in presence of a resonant laser beam after many cycles of photon absorption, spontaneous and stimulated emission will acquire a non zero momentum along the light direction.

or stimulated emission (see Fig.2.1). Spontaneously-emitted photons go in random directions, so after many cycles (N_{scat}) of absorption, spontaneous and stimulated emission, the momentum transfered to the atom is non zero and is given by

$$\Delta p_{\text{tot}} = \sum_{i=1}^{N_{\text{scat}}} \hbar k_L (1 - \cos\theta_i) \simeq N_{\text{scat}} \hbar k_L \ ,$$

where θ_i is the angle of spontaneous emission of the i-th photon (random distributed so that $\sum_i \cos\theta_i \ \rightarrow \ 0$) and N_{scat} is the number of scattered photons . Therefore the resulting force, also called "scattering force", is given by the scattering rate $\Gamma_{\text{scat}} \equiv N_{\text{scat}}/\Delta t$ at which the absorbed photons impart their momentum to the atom:

$$\mathrm{F}_{\text{scat}} \equiv \frac{\Delta p_{\text{tot}}}{\Delta t} = \underbrace{\frac{N_{\text{scat}}}{\Delta t}}_{\Gamma_{\text{scat}}} \hbar k_L \ . \tag{2.4}$$

The scattering rate Γ_{scat} depends on the type of atom and transition and is given by

$$\Gamma_{\text{scat}} = \frac{\Gamma}{2} \frac{I/I_{\text{sat}}}{1 + I/I_{\text{sat}} + 4\delta_L^2/\Gamma^2} \ , \tag{2.5}$$

where $\Gamma = 2\pi\gamma$, with γ natural linewidth of the transition. The frequency *detuning* from resonance $\delta_L = \omega_L - \omega_0$ equals the difference between the laser angular frequency ω_L and the atomic resonance angular frequency ω_0. I and I_{sat} are respectively the intensity of the laser light and the saturation

intensity of the atomic transition. From eq.2.4 and eq.2.5 we have for the scattering force the complete expression:

$$\mathbf{F_{scatt}} = \hbar \mathbf{k_L} \frac{\Gamma}{2} \frac{I/I_{\rm sat}}{1 + I/I_{\rm sat} + 4\delta_L^2/\Gamma^2} \ . \tag{2.6}$$

2.1.1 Zeeman slower

The scattering force can be used to slow down an atomic beam produced by an atomic oven. Equation 2.6 states, in fact, that the radiation force can exert a maximum deceleration of

$$a_{\rm max} = \frac{\rm F_{max}}{\rm M} = \frac{\hbar k_L}{M} \cdot \frac{\Gamma}{2} \ , \tag{2.7}$$

where M is the mass of the atom. In order for the laser light to be resonantly absorbed by a counter propagating atom moving with a certain velocity v, the angular frequency ω_L of the light must be

$$\omega_L = \omega_0 - k_L \cdot v \ .$$

As the atom repeatedly absorbs photons, slowing as desired, the Doppler shift $k_L \cdot v(z)$ changes and atom goes out of resonance with the light. In order to keep the atom in resonance with light and thus have a constant deceleration throughout the slowing process we have to compensate this change in Doppler shift. William Phillips and co-workers used the ingenious method [54, 55] shown in Fig. 2.2 in which the atomic beam travels along the axis of a tapered solenoid; the Zeeman effect of the varying magnetic field B(z)

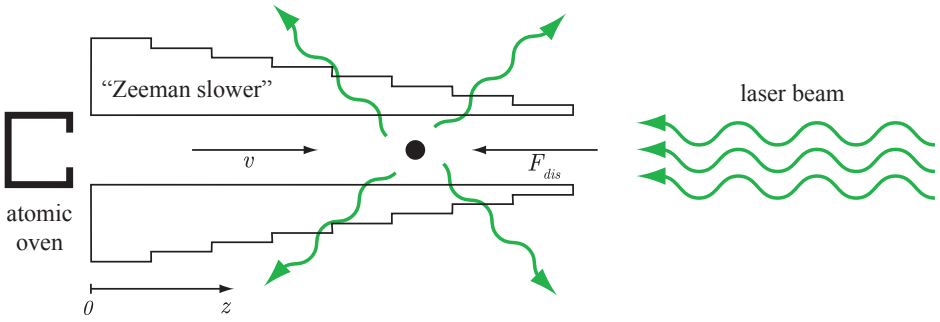

Figure 2.2: Schematic view of the Zeeman slowing mechanism. The atomic beam is slowed down by a counter propagating laser beam. A properly designed solenoid produces a magnetic field that shifts the atomic energy levels to compensate for the change in the Doppler shift as atoms decelerate.

perturbs the atomic energy levels so that the variation in Doppler shift is compensated by a properly designed magnetic field obeying the condition:

$$\omega_L = \omega_0 - k_L \cdot v(z) + \frac{\mu \mathrm{B}(z)}{\hbar} \ , \tag{2.8}$$

where μ is the atomic magnetic moment. For constant deceleration a from an initial velocity v_i at $z = 0$, the velocity as function of distance is given by

$$v(z) = v_\mathrm{i}\sqrt{1 - \frac{z}{\mathrm{L}_0}} \ , \tag{2.9}$$

where

$$\mathrm{L}_0 = v_\mathrm{i}^2/2a \tag{2.10}$$

is the stopping distance. Hence we find from eq.2.8 and eq.2.9 that the required magnetic field shape is

$$\mathrm{B}(z) = \mathrm{B}_0\sqrt{\left(1 - \frac{z}{\mathrm{L}_0}\right)} + \mathrm{B}_\mathrm{bias}$$

for $0 \leq z \leq \mathrm{L}_0$ and with

$$\mathrm{B}_0 = \frac{\hbar k_L v_\mathrm{i}}{\mu} \quad , \quad \mathrm{B}_\mathrm{bias} = \frac{\hbar(\omega_L - \omega_0)}{\mu} \ .$$

For a given change in magnetic field (B_0), corresponding to a certain decrease in velocity ($\frac{\mu \mathrm{B}_0}{\hbar k_L}$), the configuration with magnetic field inversion ($\mathrm{B}_\mathrm{bias} < 0$) shown in Fig. 2.3 has some experimental advantages in comparison with the $\mathrm{B}_\mathrm{bias} > 0$ variant. First of all, the field has a lower maximum value so that less current (or less current-turns) is needed. Additionally, the value of the magnetic field at positions downstream $z > \mathrm{L}_0$ tends to cancel out because of the contribution from the coils with current in opposite direction. Finally, the abrupt change in the field at the exit makes more definite the final exit velocity of the atoms.

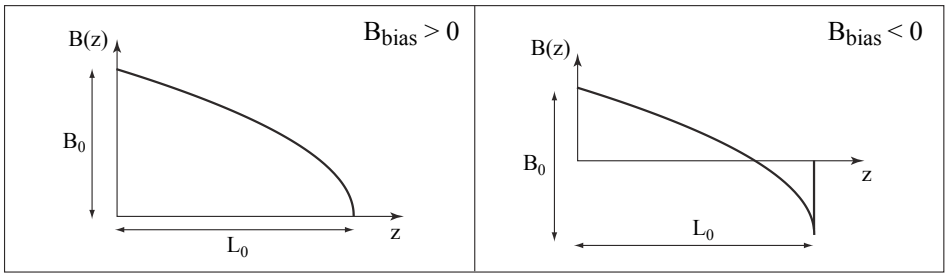

Figure 2.3: Different configurations of the magnetic field for Zeeman slowing.

2.1.2 Optical Molasses

We have already seen how a single laser beam is able to slow down a counter-propagating atomic beam. But in a gas atoms move in all directions and to reduce the temperature we have to reduce the mean square velocity along all the three Cartesian axes. For this purpose in their seminal proposal [56] Hänsch and Schawlow suggested (in a simplified 1D model) to use two counter propagating laser beams (Fig. 2.4), tuned slightly below the atomic resonance frequency. In this way an atom moving to the right sees that the laser beam opposing its motion (laser beam n.2) is Doppler shifted toward the atomic resonance. Conversely, the atom sees that the laser beam directed along its motion (laser beam n.1) is Doppler shifted further from its resonance. The atom therefore absorbs more strongly from the laser beam that opposes its motion and it slows down. The same thing happens to an atom moving to the left so the atom experiences an overall scattering force that slows down its motion according to:

$$\mathrm{F}_{\mathrm{scat}} = \mathrm{F}_1(\omega_L - \omega_0 - k_L \cdot v) - \mathrm{F}_2(\omega_L - \omega_0 + k_L \cdot v) \underset{k_L v \ll \Gamma}{\simeq} -\alpha v \ , \quad (2.11)$$

with damping coefficient

$$\alpha = -2k_L \frac{\partial \mathrm{F}_{\mathrm{scat}}}{\partial \omega_L} \underset{k_L v \ll \Gamma}{\simeq} 4\hbar k_L^2 \frac{I}{I_{\mathrm{sat}}} \frac{-2\delta_L/\Gamma}{\left[1 + (2\delta_L/\Gamma)^2\right]^2} \ . \quad (2.12)$$

So this configuration of laser beams ($\delta_L < 0 \Rightarrow \alpha > 0$) exerts a frictional, or damping, force on the atom just like that on a particle in a viscous fluid and from this came the name of "optical molasses". With pairs of laser beams added along the other coordinate axes, one obtains slowing in three dimensions and thus cooling [57] (see Fig.2.5). Because of the role of the Doppler effect in the process, this technique is called "Doppler cooling". The final temperature results from an equilibrium between a heating and cooling process:

$$\dot{\mathrm{E}}_{\mathrm{heating}} + \dot{\mathrm{E}}_{\mathrm{cooling}} = 0 \ . \quad (2.13)$$

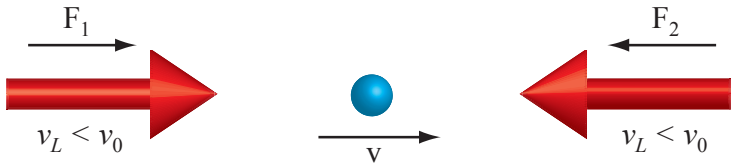

Figure 2.4: 1D molasses realized by means of two counter propagating red-detuned laser beams.

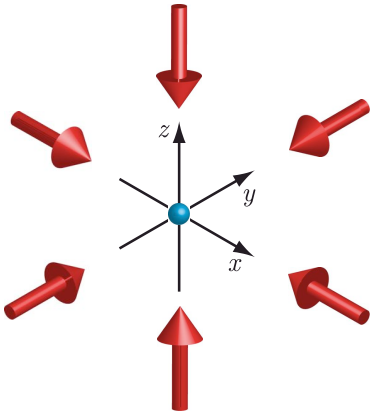

Figure 2.5: Three dimensional optical molasses.

The heating term $\dot{\mathrm{E}}_{\mathrm{heating}}$ is due to the random kicks an atom randomly receives by both absorbed and emitted photons. The mean square momentum grows with time t as a random walk in momentum space:

$$\left\langle p^2 \right\rangle = 2\eta\Gamma_{\mathrm{scat}}(\hbar k_L)^2 t \;, \tag{2.14}$$

where the factor 2 takes into account the contribution of both absorbed and emitted photons, Γ_{scat} is the scattering rate for a single laser beam given by eq.2.5 and $\eta = 6$ takes into account the three-dimensional configuration with three pairs of laser beams. From eq.2.14 comes the heating term:

$$\dot{\mathrm{E}}_{\mathrm{heating}} = \frac{d}{dt}\left(\frac{\left\langle p^2 \right\rangle}{2M}\right) = \frac{12\Gamma_{\mathrm{scat}}(\hbar k_L)^2}{2M} \;. \tag{2.15}$$

This heating is countered by the cooling force $\mathbf{F_{scat}} = -\alpha\mathbf{v}$ from eq.2.11, opposing atomic motions, that gives the cooling term:

$$\dot{\mathrm{E}}_{\mathrm{cooling}} = \mathbf{F_{scat}} \cdot \mathbf{v} = -\alpha\left(\left\langle v_x^2 \right\rangle + \left\langle v_y^2 \right\rangle + \left\langle v_z^2 \right\rangle\right) \;.$$

According to the equipartition theorem $\frac{1}{2}M\left\langle v^2 \right\rangle = \frac{1}{2}k_{\mathrm{B}}T$ the cooling rate can be expressed in terms of the temperature:

$$\dot{\mathrm{E}}_{\mathrm{cooling}} = -\alpha \cdot \frac{3k_{\mathrm{B}}T}{M} \;. \tag{2.16}$$

Inserting eq.2.15 and eq.2.16 in eq.2.13 and by substitution of α (eq.2.12) and Γ_{scat} (eq.2.5) one can finally find the equilibrium temperature ("Doppler temperature")

$$k_{\mathrm{B}}T = \frac{\hbar\Gamma}{4} \cdot \frac{1 + (2\delta_L/\Gamma)^2}{-2\delta_L/\Gamma} \;. \tag{2.17}$$

This expression is valid for 3D Doppler cooling in the limit of low intensity $I \ll I_{\rm sat}$ and when the recoil energy $\hbar^2 k_L^2/2M \ll \hbar\Gamma$. The key result is that eq.2.17 has a minimum at $\delta_L = -\Gamma/2$ of

$$k_{\rm B} T_{\rm D} = \frac{\hbar\Gamma}{2} \,, \tag{2.18}$$

that represents the lowest temperature expected in the optical molasses and is called "Doppler cooling limit" [58].

The Doppler cooling is valid only for atoms that can be approximated by a two-level system. Remarkably, atoms having degenerate sub-levels can reach lower temperature by means of a further cooling mechanism called *Sisyphus cooling* [59]. The limit of this *sub-Doppler cooling* is set by the recoil energy acquired in spontaneous emission

$$E_{\rm r} = \hbar^2 k_L^2/(2M) \,, \tag{2.19}$$

which can be expressed in terms of *recoil temperature* $T_{\rm r}$ defined as

$$\frac{1}{2} k_{\rm B} T_{\rm r} = E_{\rm r} \,. \tag{2.20}$$

The lowest attainable temperature with sub-Doppler cooling is given by $T_{\rm r}/2$ [60].

2.1.3 Magneto Optical Trap (MOT)

Although the molasses technique allows to cool atoms and to stuck them in a diffusive motion regime within the region where laser beams intersect, it does not provide a restoring force that would trap the atoms pushing them in a certain position. Nevertheless, with the correct choice of polarizations for the laser beams, optical molasses can be turned into a trap by the addition of a magnetic field gradient [61]. The operating principle of this so called *magneto-optical-trap* (MOT) is shown in Fig.2.6 for a simple 1D case with a $J = 0$ to $J = 1$ transition. For an external magnetic field

$$B(z) = bz \;\; (b > 0) \,, \tag{2.21}$$

the resulting shift Zeeman of the m_J sub-levels is

$$\Delta E(z) = \mu m_J B(z) \quad \Rightarrow \quad \omega_0(z) = \omega_0 + m_J \beta z \,, \tag{2.22}$$

where $\beta = \mu b/\hbar$.

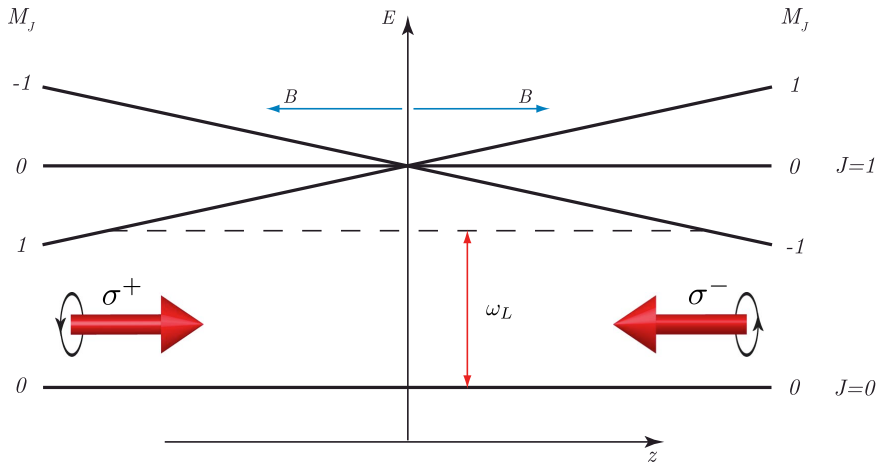

Figure 2.6: One dimensional magneto-optical trap illustrated for the case of an atom with a $J = 0$ to $J = 1$ transition.

The atom is illuminated by two counter-propagating laser beams tuned below the atomic resonance frequency and with opposite circularly polarization. The Zeeman shift and the selection rules lead to an imbalance in the radiative force from the laser beams that pushes the atom back towards the center of the trap $z = 0$. In fact an atom (in ground state $J = 0$) at $z > 0$ sees the $\Delta m_J = -1$ transition closer to resonance and the selection rules lead to absorption of photons from the beam with polarization σ^-. This gives a scattering force the pushes the atom towards the trap center $z = 0$. A similar process occurs for an atom at $z < 0$; it sees the $\Delta m_J = +1$ transition closer to resonance and the selection rules lead to absorption of photons from the beam with polarization σ^+ thus pushing the atom back towards $z = 0$. Mathematically the force experienced by the atom in the MOT in described by

$$\begin{aligned} \mathrm{F}_{\mathrm{MOT}} &= \mathrm{F}^{\sigma^+}_{\mathrm{scatt}}\left(\omega_L - k_L v - (\omega_0 + \beta z)\right) - \mathrm{F}^{\sigma^-}_{\mathrm{scatt}}\left(\omega_L - k_L v - (\omega_0 - \beta z)\right) \\ &\simeq -\alpha v - kz \,, \end{aligned} \tag{2.23}$$

where $k = \alpha\beta/k_L$. This expression is valid for small Zeeman shift $\beta z \ll \Gamma$ and small atom velocity $k_L v \ll \Gamma$. Therefore atoms entering in a MOT are slowed as in the optical molasses and the position dependent force pushes the cold atoms to the trap center. Atoms undergo an over-damped simple harmonic motion described by

$$\ddot{z} + \frac{\alpha}{M}\dot{z} + \frac{k}{M}z = 0 \,.$$

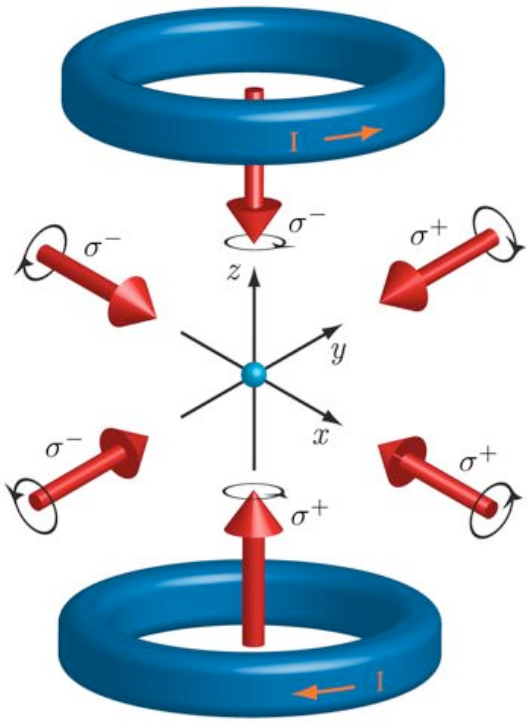

Figure 2.7: Three dimensional magneto optical trap.

This 1D scheme can be easily extended in three dimensions by using three orthogonal pairs of laser beams, as in the optical molasses, with a certain configuration of polarizations and intersecting at the center of a pair of coils with opposite currents (see Fig.2.7). The magnetic field produced with this configuration is zero at the center of the coils and its magnitude increases linearly in every direction for small displacements from the zero point. This comes from the Maxwell equation $\overrightarrow{\nabla} \cdot \overrightarrow{B} = 0$ that implies

$$\frac{dB_x}{dx} = \frac{dB_y}{dy} = -\frac{1}{2}\frac{dB_z}{dz} \ ,$$

so the gradient in any radial direction is half of that along the z-direction. This trap is very robust and does not depend critically on balanced light beams, purity of the circular polarization, or laser frequency. Additionally this technique gives more atoms and at higher density than the optical molasses technique. The velocity capture of a MOT can be estimated taking the radius r of laser beams as the stopping distance of a captured atom

according to the equation

$$\left(v_c^{MOT}\right)^2 = 2ra_{\text{eff}} \,,$$

where a_{eff} is the effective deceleration experienced by the atom. This is generally expressed as half of the acceleration at $I = I_{\text{sat}}$ to take into account the fluctuation of the force arising from the randomness in the number of photons scattered:

$$a_{\text{eff}} = \frac{1}{2}a(I = I_{\text{sat}}) = \frac{a_{\max}}{4} \,,$$

where $a_{\max}$ is given by eq.2.7. Finally the MOT velocity capture has the expression

$$v_c^{MOT} = \sqrt{\frac{\hbar k_L}{M}\frac{\Gamma}{4}r} \,. \tag{2.24}$$

Atoms in the MOT have a higher temperature than in the optical molasses for two main reasons. First, the sub-Doppler cooling mechanism is depressed because the strong magnetic field breaks the energy degeneracy of the Zeeman sublevels. Additionally in condition of high atomic density an atom in a MOT absorbs resonant photons spontaneously emitted by the dense cloud of cold atoms.

Typically the MOT technique is employed to collect cold atoms from a slowed atomic beam. Such cold sample is then used to perform further experiments such as loading atoms on conservative optical traps.

2.2 Conservative Force (Dipole Force)

In addition to the scattering force there is another kind of radiative force. A perturbing radiation also changes the energy of the atomic levels (see Fig.2.8). This effect is called *a.c. Stark shift* and is most important at large frequency detuning $|\omega_L - \omega_0| \gg \Gamma$ where the effect of absorption is negligible. The a.c. Stark shift is given by

$$\Delta E \simeq \frac{\hbar\Omega^2}{4(\omega_L - \omega_0)} , \tag{2.25}$$

where $\Omega = (\Gamma/2)\sqrt{I/I_s}$ is the *Rabi frequency*. Eq.2.25 is valid for light intensity such that $|\omega_L - \omega_0| \gg \Omega$ and it states that the a.c. Stark shift, for an atom in the ground state acts as a potential U_{dipole} in which the atom moves. More generally, in three dimensions

$$\mathbf{F}_{\text{dipole}} = -\overrightarrow{\nabla} U_{\text{dipole}} ,$$

where

$$U_{\text{dipole}} \simeq \frac{\hbar\Omega^2}{4\delta_L} \equiv \frac{\hbar\Gamma}{8}\frac{\Gamma}{\omega_L - \omega_0}\frac{I(\vec{r})}{I_{\text{sat}}} . \tag{2.26}$$

This conservative force and its potential are also called respectively *dipole force* and *dipole potential* since they arise from the interaction of the induced atomic dipole moment with the intensity gradient of the light field [62]. Eq.2.26 states that atoms can be trapped in the minima of a potential related with the intensity pattern $I(\vec{r})$ of a far-detuned laser beam. This provides a very versatile technique to design a variety of trapping geometries. In particular three main points can be outlined to design an optical trap.

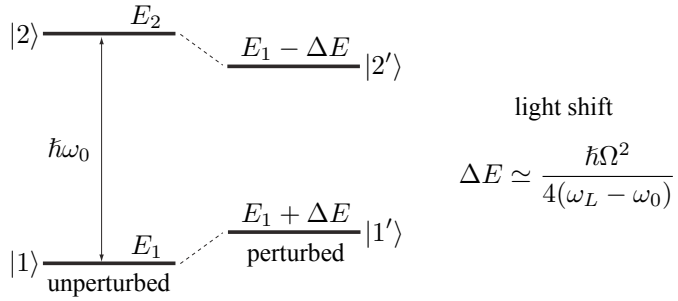

Figure 2.8: Energies of two states unperturbed (light field off) and perturbed by an external light field oscillating at the frequency ω_L far-off transition resonance ω_0. The two states are shifted due to the atom-light interaction, and the shift is called light shift.

- **Trap depth:** In order to efficiently trap atoms with a certain temperature T the depth of the optical trap (U_{depth}) must be higher than the thermal energy of atoms:

$$U_{\text{depth}} \gg k_{\text{B}}T \, .$$

- **Scaling with intensity and detuning:** The ratio between the optical potential and the heating energy due to the absorption of photons is given by

$$\frac{U_{\text{dipole}}}{\hbar\Gamma_{\text{scatt}}} \simeq \frac{\omega_L - \omega_0}{\Gamma} \, .$$

  So in order to keep as low as possible the scattering rate in an optical trap with a certain depth it is necessary to operate at large detuning.

- **Sign of detuning:** The sign of the dipole potential eq.2.26 depends on detuning. For “red" detuning $\omega_L < \omega_0$ potential minima occurs at positions with maximum intensity. Conversely, for “blue" detuning $\omega_L > \omega_0$ potential minima correspond to minima of the intensity. According to this distinction, dipole traps can be divided into two main classes, red-detuned traps and blue-detuned traps.

2.2.1 Focused Beam Trap

The simplest way to realize a dipole trap is by means of a focused Gaussian laser beam tuned far below the atomic resonance ($\omega_L \ll \omega_0$). An optical trap can be easily realized by focusing a laser beam into a cloud of atoms which were previously collected and cooled by a MOT. The spatial intensity distribution of a focused Gaussian beam with maximum intensity I_0 and propagating along the z axis is given by

$$I_G(r,z) = I_0 \left(\frac{w_0}{w(z)}\right)^2 \frac{2P}{\pi w^2(z)} \exp\left(-2\frac{r^2}{w^2(z)}\right) \, ,$$

where r is the radial coordinate and $w^2(z)$ represents the $1/e^2$ radius of the beam as a function of the axial coordinate z. The latter is described by

$$w(z) = w_0 \sqrt{1 + \left(\frac{z}{z_R}\right)^2} \, ,$$

where w_0 is called *waist* and denotes the minimum radius and $z_R = \pi w_0^2/\lambda_L$ is the *Rayleigh* length (see Fig.2.9). If the thermal energy $k_{\text{B}}T$ is much

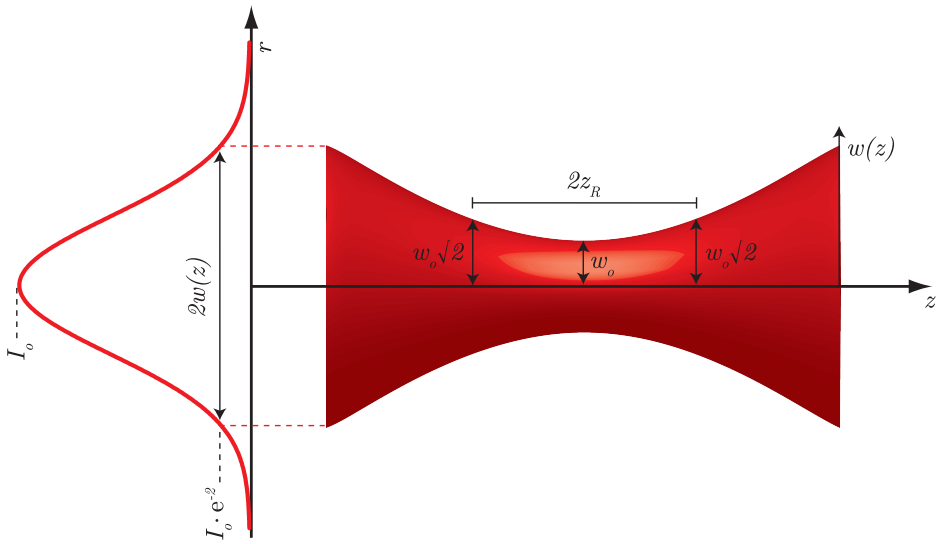

Figure 2.9: Relevant parameters of a gaussian beam.

smaller than the potential depth U_{depth}, the atomic sample can be considered trapped close to the minimum of the trap. In this case, the optical potential experienced by atoms can be well approximated around its minimum

$$U_{\text{dipole}}(r,z) \underset{(r,z)\to(0,0)}{\simeq} U_{\text{depth}} \left[-1 + 2\left(\frac{r}{w_0}\right)^2 + \left(\frac{z}{z_R}\right)^2 \right] , \tag{2.27}$$

where the depth of dipole trap, according to eq.2.26, is given by

$$U_{\text{depth}} = \frac{\hbar\Gamma}{8} \frac{\Gamma}{\omega_0 - \omega_L} \frac{I_0}{I_{\text{sat}}} . \tag{2.28}$$

The cylindrically symmetric harmonic potential in eq.2.27 has two different trapping frequencies along the radial (ω_r) and axial direction (ω_z):

$$\omega_r = \sqrt{\frac{4U_{\text{depth}}}{M w_0^2}}$$

$$\omega_z = \sqrt{\frac{2U_{\text{depth}}}{M z_R^2}} .$$

The ratio between radial and axial trapping frequencies is $\omega_r/\omega_z = \pi\sqrt{2}w_0/\lambda_L$, where $w_0 > \lambda_L$. Therefore the potential in the radial direction is much steeper than in the axial direction. For this reason focused beam traps are mostly aligned along the horizontal axis such that the strong radial force $\sim U_{\text{depth}}/w_0$ minimizes the perturbing effects of gravity.

2.2.2 Optical Lattice

An optical lattice can be realized by simply retroreflecting a gaussian laser beam while conserving the curvature of the wave fronts and the polarization. In this case the two counter-propagating beams interfere as two plane waves:

$$\begin{aligned} E &= E_0 \cos(\omega_L t - k_L z) + E_0 \cos(\omega_L t + k_L z) \\ &= 2E_0 \cos(k_L z)\, cos(\omega_L t) \ , \end{aligned}$$

producing a spatial modulated intensity

$$I(z) = 4I_0 \cos^2(k_L z) \ .$$

Therefore, assuming small extension of the atomic cloud, the potential experienced by atoms in a retroreflected gaussian beam has the form

$$U_{\text{lattice}}(r,z) \underset{(r,z)\to(0,0)}{\simeq} U_{\text{depth}} \cos^2(k_L z) \left[-1 + 2\left(\frac{r}{w_0}\right)^2 + \left(\frac{z}{z_R}\right)^2 \right] \ ,$$

with

$$U_{\text{depth}} = 4 \times \frac{\hbar\Gamma}{8} \frac{\Gamma}{\omega_0 - \omega_L} \frac{I_0}{I_{\text{sat}}} \ .$$

The potential depth is four times larger than the corresponding trap depth for a single focused beam in eq.2.28. As for a single focused beam, radial confinement is provided by a restoring force $\sim U_{\text{depth}}/w_0$. The potential is spatially modulated along the axial direction with a period of $\lambda_L/2$. Therefore atoms are strongly confined in the antinodes if $\omega_L < \omega_0$ and in

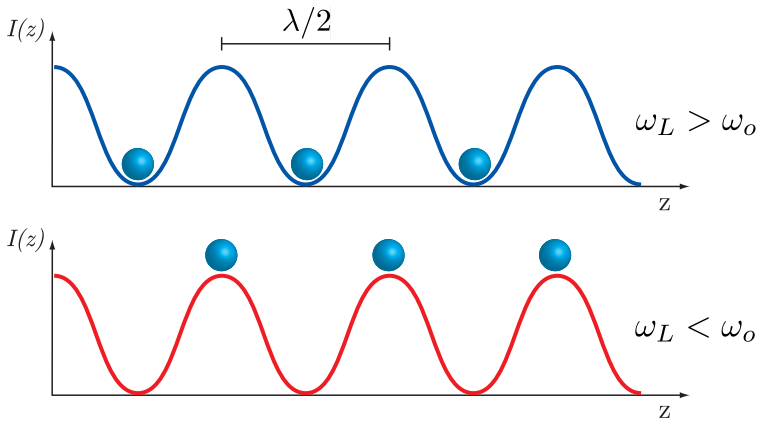

Figure 2.10: Schematic view of an optical lattice.

the nodes if $\omega_L > \omega_0$ (see Fig.2.10). The restoring force around the potential minima along the axial direction is $\sim U_{\text{depth}} k_L$ resulting in a regular one-dimensional lattice. The potential along the axial direction can be approximated around its minima by a harmonic potential having a trapping frequency given by

$$\omega_z = k_L \sqrt{\frac{2U_{\text{depth}}}{M}} \,. \tag{2.29}$$

Optical lattice in one dimension can be aligned vertically, since the axial confinement force greatly exceeds the gravitational force Mg.

Chapter 3

A Strontium Optical Lattice Clock

In this chapter the basic operating principle of a strontium optical lattice clock is presented. In particular the peculiar features of the strontium atom are discussed. The theoretical background introduced in the previous chapter is here applied to the case of strontium atom. The procedure for strontium laser cooling is briefly described together with the scheme for clock transition interrogation.

3.1 The Strontium Atom

An atom suitable for being used as an optical frequency reference must have some key features. First of all, it has to provide a high Q transition that can be interrogated with available laser technology. Furthermore this narrow transition has to be insensitive to any external perturbation from electric and magnetic fields. Finally, this atom must have strong transitions to efficiently perform the laser cooling and trapping needed for the preparation of the ultracold atomic sample. Because of these requests only few kinds of atoms are suitable for optical clock application. Today, the most promising and studied neutral atomic systems are the alkaline-earth-metal-like atoms such as Mg, Ca, Sr, Yb and recently Hg. These atoms have two electrons in the outer shell and the electron spins can be parallel and anti-parallel. This fact implies that energy levels of such atoms are grouped in two separate classes, one with total electronic spin $S = 1$ (triplet state) and one with total electronic spin $S = 0$ (singlet state). The transitions between

Isotope	Relative atomic mass	Relative abundance	Nuclear spin
^{88}Sr	87.905 6143(24)	82.58(1) %	0
^{86}Sr	85.909 2624(24)	9.86(1) %	0
^{87}Sr	86.908 8793(24)	7.00(1) %	9/2
^{84}Sr	83.913 425(4)	0.56(1) %	0

Table 3.1: Natural strontium isotopes (NIST data)

these two groups are forbidden by the selection rule $\Delta S = 0$ but actually they are weakly allowed because of the effect of the spin-orbit interaction that breaks the spin symmetry. It results that these transitions, also called "intercombination lines", are very narrow in frequency and therefore they are very interesting for metrological applications.

Among the alkaline-earth-metal-like atoms strontium ($Z = 38$) seems to summarize most of their useful properties. Strontium has four natural isotopes , whose properties are listed in Table 3.1. The bosonic (even) isotopes have zero nuclear spin, thus they are perfect scalar particles in the J = 0 states. This fact in very important for high-precision measurement since, in absence of nuclear spin, states with $J = 0$ do not have hyperfine sub-levels and they are therefore insensitive to stray magnetic fields. Another important source of perturbations is represented by the interatomic collisions. In this respect, the ^{88}Sr isotope exhibits excellent features due to its remarkably small collisional cross-section in its ground state. Immunity to external magnetic fields and collisions makes bosonic strontium an ideal quantum sensor for a number of applications [63, 64] showing the longest coherent evolution time of an atomic wave-function [65].

The energy levels of strontium are shown in Fig.3.1 where they are indicated in the usual *Russel-Saunders* notation of $^{2S+1}L_J$, where S is the total electronic spin (either 0 or 1), L is the orbital angular momentum of electrons, and J is the total angular momentum of the state. Much of the interest in strontium relies on the intercombination line $^1\mathrm{S}_0 - {}^3\mathrm{P}_0$ that is double forbidden by the selection rules $\Delta S = 0$ and $\Delta J \neq 0$ (if $J = 0$). This transition has a virtual zero linewidth for the even isotopes in absence of external fields and it has a linewidth of ~ 1 mHz for the ^{87}Sr isotope due to the hyperfine mixing. This ultra-narrow transition lies in the optical domain at 698 nm and it can be easily reached by using a compact solid-state laser source [66, 67].

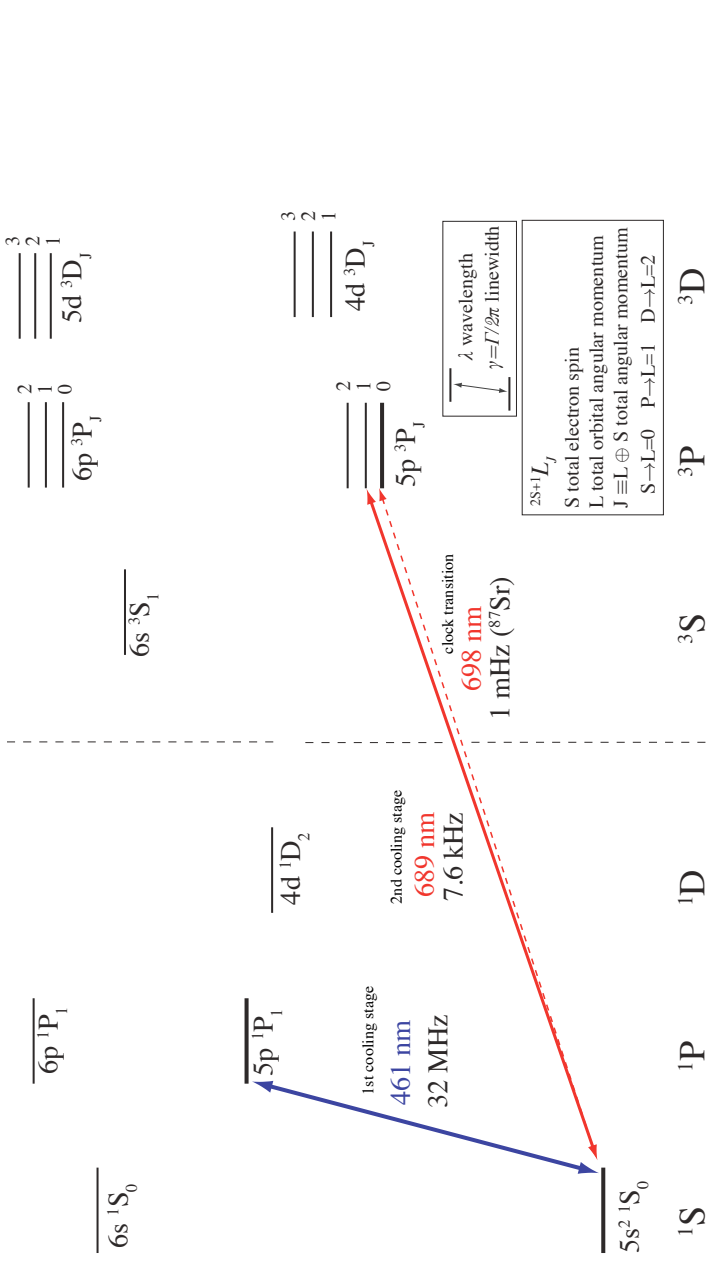

Figure 3.1: Electronic level structure of atomic strontium. The clock transition $^1S_0 - {}^3P_0$ and the relevant transitions for laser cooling ($^1S_0$-$^1P_1$ and $^1S_0$-$^3P_1$) are indicated with their wavelengths and linewidths. Remarkably all these transitions are easily accessible with the available solid state laser technology [68, 66, 67].

Trans.	λ (nm)	T_D	T_r	I_{sat}	a_{max} (m/s^2)
$^1S_0$-$^1P_1$	461	770 μK	1.03 μK	43 mW/cm^2	$\sim 10^6$
$^1S_0$-$^3P_1$	689	180 nK	460 nK	3 μW/cm^2	160

Table 3.2: Relevant parameters for laser cooling and trapping using the $^1S_0$-$^1P_1$ and $^1S_0$-$^3P_1$ transitions.

Beside the clock transition $^1S_0 - {}^3P_0$, other energy levels are involved in the cold atomic sample preparation. The strong dipole allowed $^1S_0 - {}^1P_1$ transition at 461 nm has a natural width of 32 MHz and it is used to slow thermal atoms and to trap them in a magneto optical trap (MOT). Atoms in this so called “Blue MOT" are Doppler cooled to a final temperature at ~ 1 mK level. The ultimate limit of this “first cooling stage" is set by the Doppler temperature (eq.2.18) which depends on the natural linewidth of the transition. A “second cooling stage" can be performed by using the intercombination transition $^1S_0 - {}^3P_1$ which has a natural linewidth of 7.6 kHz. Laser cooling on this narrow transition has the peculiarity to have a Doppler temperature $T_D = 180$ nK below the ultimate limit $T_r/2 = 230$ nK set by the photon recoil temperature T_r (eq.2.20). Table 3.2 summarizes the relevant parameters of each cooling stage, further details will be discussed in the following two sections. Remarkably both the transitions $^1S_0 - {}^1P_1$ and $^1S_0 - {}^3P_1$ for cold atomic sample preparation are easily accessible with the available solid state laser technology [68].

3.2 First Cooling Stage: slowing and Blue MOT

Radiation at 461 nm resonant with the dipole allowed transition $^1S_0 - {}^1P_1$ can exert on atoms a maximum acceleration (or deceleration) of $\sim 10^6$ m/s^2 (eq.2.7) which allows to efficiently slow down the thermal atoms produced by an hot Sr oven. Typical operation temperature for strontium oven is about $350 - 400\,^\circ$C, corresponding to a most probable velocity given by $v_i = \sqrt{3k_BT/M} \sim 430$ m/s. So the stopping distance (eq.2.10) at $I = I_{sat}$ ($a = a_{max}/2$) is around 20 cm. By properly designing the magnetic field for Zeeman slowing thermal atoms can be slowed down in such a distance and be efficiently trapped in a MOT working on the $^1S_0 - {}^1P_1$ transition. This Blue MOT at 461 nm is indeed very robust and for a typical choice of laser beams diameter of 10 mm it has a capture velocity of about 50 m/s (eq.2.24).

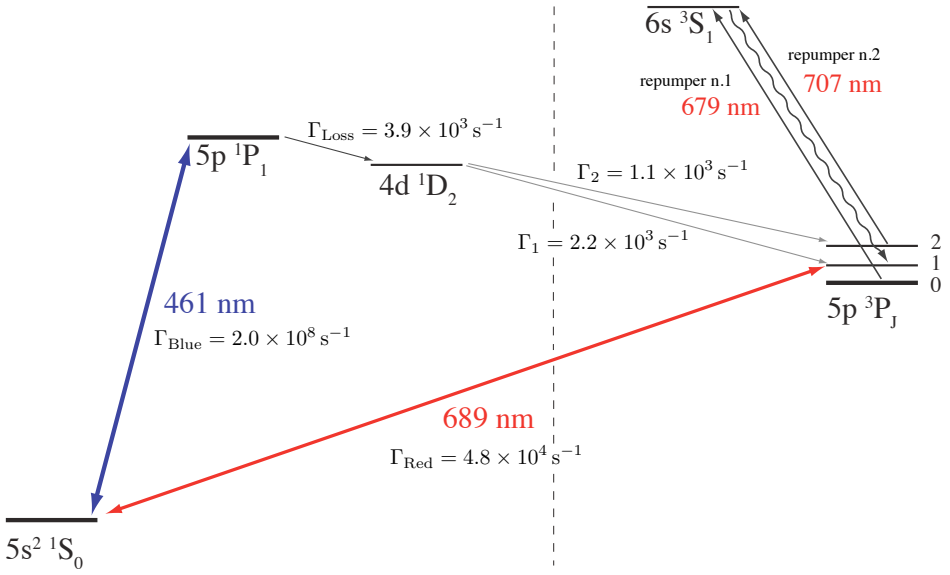

Figure 3.2: Partial electronic level structure of atomic strontium showing the loss channel $4d\,^1D_2 \rightarrow 5p\,^3P_2$ of the first cooling stage. Atoms pumped in the metastable state $5p\,^3P_2$ can be recycled by using two repumping lasers at 679 nm and 707 nm.

Atoms in the Blue MOT are cooled reaching a final temperature at the mK level [69].

The $^1S_0 - {}^1P_1$ transition is not perfectly closed, due to a small leakage towards the $4d\,^1D_2$ state (branching ratio $\Gamma_{Loss}/(\Gamma_{Loss}+\Gamma_{Blue}) \sim 10^{-5}$). The direct $^1D_2 - {}^1S_0$ decay channel is forbidden in dipole approximation, and atoms from the $4d\,^1D_2$ basically decay towards the $5p\,^3P_1$ (branching ratio $\Gamma_1/(\Gamma_1+\Gamma_2) \sim 67\%$) state and towards the metastable $5p\,^3P_2$ (branching ratio $\Gamma_2/(\Gamma_1+\Gamma_2) \sim 33\%$) state. In order to recycle the atoms stored in the metastable states $5p\,^3P_2$ and $5p\,^3P_0$ two pumping lasers, respectively at 707 nm and 679 nm, can be used to pump these atoms in the $6s\,^3S_1$ state, where they quickly decay in the $5p\,^3P_1$ state and then finally in the ground state $5s^2\,^1S_0$ through the strongest intercombination line $^1S_0 - {}^3P_1$. Typically the effect of the repumping lasers is to increase the number of atoms trapped into the Blue MOT by about one order of magnitude.

3.3 Second Cooling Stage: Red MOT

As anticipated cold atoms trapped into the Blue MOT are then loaded in a MOT operating on the strongest intercombination line $^1S_0 - {}^3P_1$. This

Trans.	γ	$\nu_r = E_r/h$	$s = I/I_{sat}$	$\gamma_E = \gamma\sqrt{1+s}$	$\Delta = \lvert\nu_L - \nu_0\rvert$
$^1S_0$-$^1P_1$	32 MHz	11 kHz	~ 1	~ 45 MHz	40 MHz
$^1S_0$-$^3P_1$	7.6 kHz	4.8 kHz	$\sim 10^3$	~ 240 kHz	400 kHz

Table 3.3: Relevant parameters for Blue and Red MOT operation.

so called “Red MOT" at 689 nm provides a second cooling stage which relies on a transition with a natural linewidth $\gamma = 7.6\,\text{kHz}$ comparable with the single-photon-recoil frequency shift

$$\nu_r = E_r/h = 4.8\,\text{kHz} \tag{3.1}$$

where h is the Planck's constant and E_r is the single-photon-recoil energy (eq.2.19). This means that the absorption (or emission) of a photon kicks an atom out of resonance. In this case laser cooling can not be described by the Doppler theory presented in chapter 2 and a fully quantum mechanical approach is needed. For laser frequency (ν_L) tuned below the atomic resonance (ν_0) this two-stages cooling process separates into three different regimes [70, 71, 72, 73] defined by the relative size of the absolute detuning $\Delta = |\nu_L - \nu_0|$, the single-photon-recoil frequency shift ν_r and the power-broadened linewidth $\gamma_E = \gamma\sqrt{1+s}$ determined by the saturation parameter $s = I/I_s$.

- **Regime (I) $\gamma_E \gg \nu_r$, $\Delta \leq \gamma_E$:** semiclassical approach used in the chapter 2 is a good approximation. Table 3.3 shows that Blue MOT operates in this regime. Additionally the gravitational force is negligible with respect to the maximum scattering force of radiation at 461 nm:

  $$\frac{F_{max}}{Mg} \sim 10^5\,,$$

  where $F_{max} = \hbar k_L \Gamma/2$ (eq.2.6) and M is the strontium atom mass. Therefore into the Blue MOT atomic dynamics consists of a damped harmonic motion with a dispersion-shaped radiation force occurring over the entire trap volume (see Fig.3.3). Consequently the trap potential energy assumes the U-shaped form shown in Fig.3.4 with the minimum in the center of the trap. In this regime temperature is well described by the Doppler theory, with the “Doppler cooling limit" achieved at $\Delta = \Gamma_E/2$ (eq.2.18).

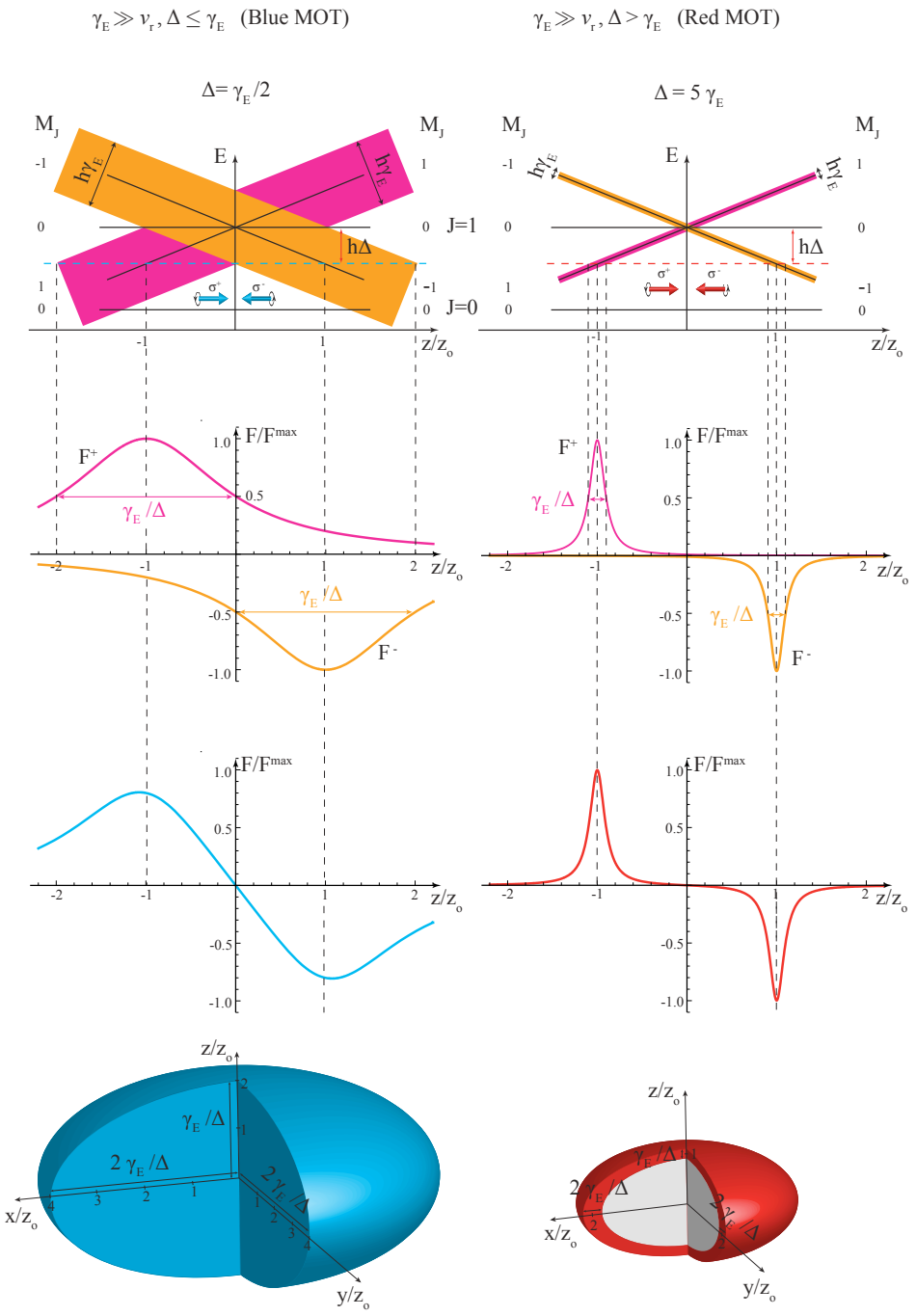

Figure 3.3: Schematic comparison between magneto-optical-trap with broad line ($\Delta \leq \gamma_E$, regime I) and narrow line ($\Delta > \gamma_E$, regime II) transitions.

- **Regime (II)** $\gamma_{\mathbf{E}} \gg \nu_{\mathbf{r}}$, $\Delta > \gamma_{\mathbf{E}}$ **:** regime of operation of the Red MOT for typical value of $s \sim 10^3$. The semiclassical model is valid and the resulting 3D radiative force acts only along a thin shell volume marking the outer trap boundary (see Fig.3.3). Here, the trap boundary roughly corresponds to positions where the radiative force is peaked. Along the vertical direction this boundary z_0 is defined as the position, from the center of the trap, where the magnetic field gradient compensates the light detuning

$$g_J \mu |m_J| \left(\frac{\partial B}{\partial z}\right)_{z=0} z_o = h\Delta \,.$$

Additionally the effect of gravity can not be neglected since

$$\frac{F_{\max}}{Mg} \sim 16 \,.$$

This situation, as shown by Fig.3.4, produces a box potential with a gravitationally induced z-axis tilt. Hence, in the $x-y$ plane, atomic motion consists of free-flight between hard wall boundaries while along the vertical z axis the atoms sink to the bottom of the trap where they interact with only the upward propagating trapping beam. The position of equilibrium z_{eq} is therefore given by the condition

$$F^+ \left(v_z = 0,\, z = z_{\mathrm{eq}}\right) - Mg = 0 \qquad (\text{for } F^+ \geq Mg) \,,$$

where F^+ is the force exerted by the upward propagating trapping beam:

$$F^+ = F^{\max} \frac{s}{1 + s + 4\left[-2\pi\Delta\left(1 + z/z_o\right) - k_L v_z\right]^2 / \Gamma^2} \,.$$

Trap thermodynamics is thus determined by the value of the damping coefficient α (eq.2.12) at $z = z_{\mathrm{eq}}$

$$\alpha = -\left(\frac{\partial F^+}{\partial v_z}\right)_{v_z=0,\, z=z_{\mathrm{eq}}} \,. \tag{3.2}$$

The final temperature is given by the equilibrium condition

$$\underbrace{-\alpha \left\langle v_z^2 \right\rangle}_{\text{cooling}} + \underbrace{\frac{2\Gamma_{\mathrm{scat}} \left(\hbar k_L\right)^2}{2M}}_{\text{heating}} = 0 \tag{3.3}$$

between a cooling term due to the viscous dynamics and an heating term due to absorption and emission of photons (eq.2.15) in presence of a single laser cooling beam.

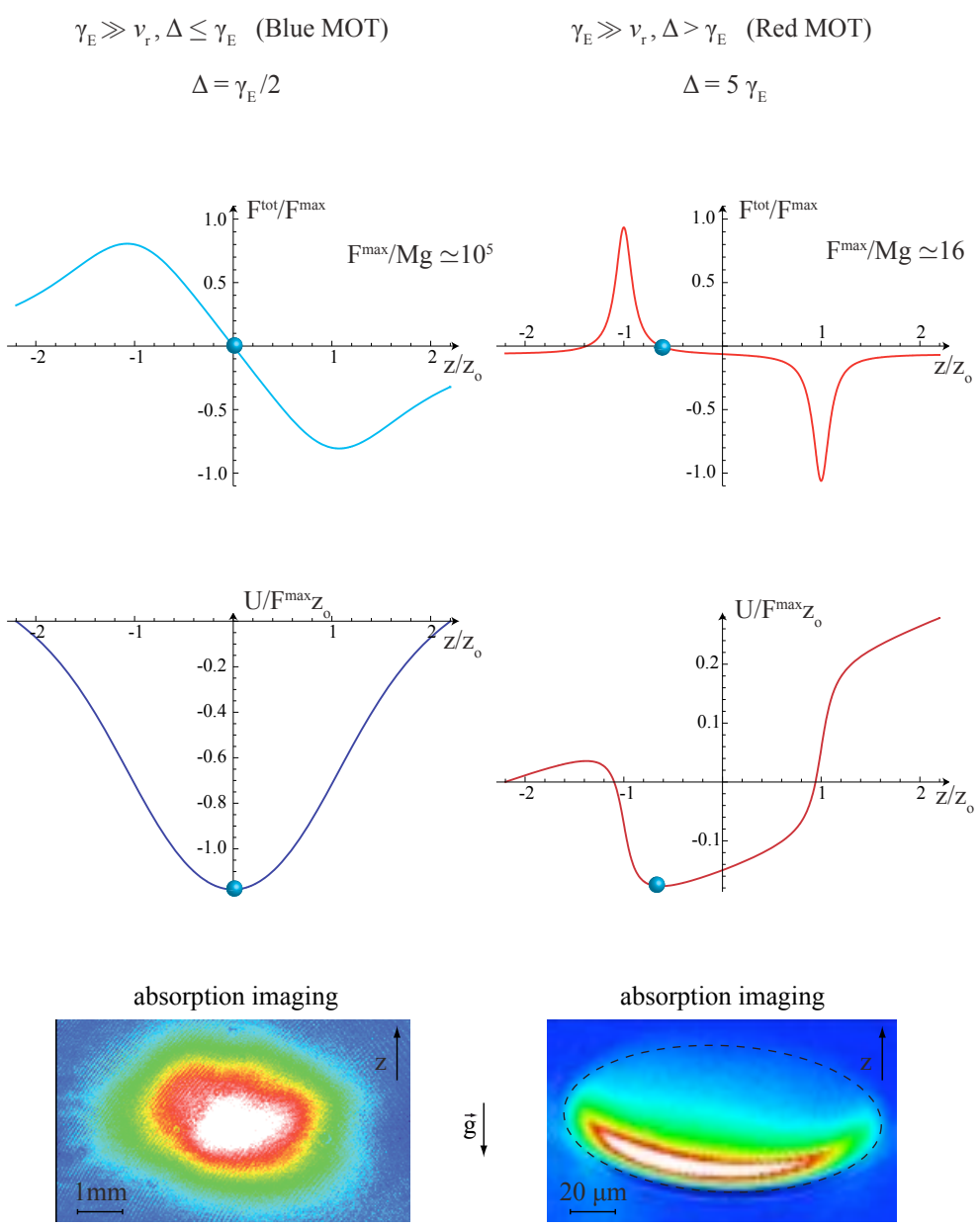

Figure 3.4: Effect of the gravitational force on magneto optical trapping for Blue and Red MOT.

In these conditions the scattering rate is

$$\Gamma_{\text{scat}} \simeq \frac{F^{+}\left(v_z = 0,\, z = z_{\text{eq}}\right)}{\hbar k_L} = \frac{Mg}{\hbar k_L}\,.$$

By using the equipartition theorem $\frac{1}{2}M\left\langle v^2\right\rangle = \frac{1}{2}k_{\text{B}}T$ from condition (eq.3.3) we obtain the equilibrium temperature

$$T = \frac{Mg\hbar k_L}{k_{\text{B}}\alpha}\,,$$

which for the definition of α (eq.3.2) finally becomes

$$T(s) \simeq \underbrace{\frac{h\gamma}{2k_B}}_{T_{\text{D}}=180\,\text{nK}} \sqrt{1+s}\,. \tag{3.4}$$

Remarkably (eq.3.4) states that in this regime the final temperature of the Red MOT is not predicted by the standard Doppler theory (eq.2.17), since it does not depend on frequency detuning Δ and it is determined only by the saturation parameter s. For typical values of s ranging from 10^3 to 10, compatible with the condition $F^{+} \geq Mg$, it is possible to reach final temperatures from $5.7\,\mu$K to 600 nK respectively.

- **Regime (III)** $\gamma_{\mathbf{E}} \sim \nu_{\mathbf{r}}$**:** this regime is realized in the Red MOT when s approaches unity ($\gamma_{\text{E}} \simeq \gamma \sim \nu_{\text{r}}$). The photon-recoil-driven impulsive force dominates, cooling dynamics becomes fully quantum-mechanical and the minimal attainable temperature is given by the photon-recoil limit $T_{\text{r}}/2 = 230\,\text{nK}$ [60].

3.4 Magnetically Induced Spectroscopy

As previously mentioned, the $^1S_0 - {}^3P_0$ transition is completely forbidden for bosonic strontium atoms. An external interaction has to be inserted in the system to properly engineering the atomic level structure and create a finite controllable $^1S_0 - {}^3P_0$ transition probability. These methods basically consist of coupling the metastable $^3P_0$ level to other electronic states by using either multiple near-resonant laser fields [74, 75] or simply a small static magnetic field [76]. The latter scheme was firstly experimentally demonstrated by the Ytterbium experiment team at NIST [77, 78] and it seems feasible to reach the 10^{-17} accuracy level [79]. It consists on placing the atoms in a proper static magnetic field $\mathbf{B}$ that couples the states $^3P_0$ and $^3P_1$. These states are split in energy by ΔE (see Fig.3.5) and have a coupling matrix element

$$\left\langle {}^3P_0 \right| \hat{\mu} \cdot \mathbf{B} \left| {}^3P_1 \right\rangle = \hbar \Omega_B \,,$$

where $\hat{\mu}$ is the magnetic-dipole operator. According to first-order perturbation theory with the condition $|\hbar\Omega_B/\Delta E| \ll 1$, the state $^3P_0$ acquires a small admixture of the state $^3P_1$ due to the presence of the static magnetic field:

$$\left| {}^3P_0\,' \right\rangle = \left| {}^3P_0 \right\rangle + \frac{\hbar\Omega_B}{\Delta E} \left| {}^3P_1 \right\rangle \,.$$

The result is that the clock transition between the unperturbed ground state $^1P_0$ and the excited state $^3P_0{}'$ becomes partially allowed. Therefore in pres-

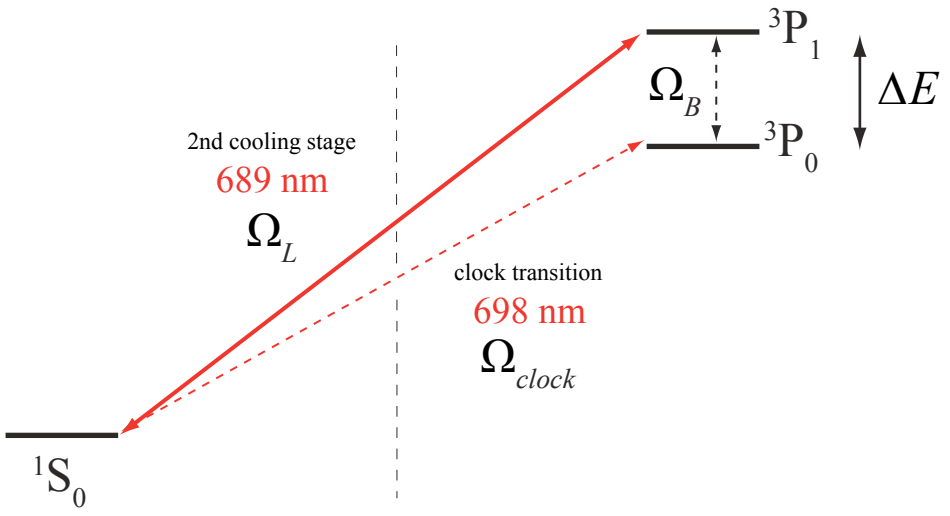

Figure 3.5: Diagram of relevant transitions for the magnetic field mixing of $^3P_0$ and $^3P_1$ states to allow excitation of the otherwise forbidden $^1S_0 - {}^3P_0$ transition.

ence of an optical field with amplitude $\mathbf{E}$ and wavelength λ a resonance will be observed on the forbidden transition when $\lambda = 698\,\mathrm{nm}$. The resulting Rabi frequency for excitation of clock transition is

$$\Omega_{clock} = \left\langle {}^3\mathrm{P}_0{}' \right| \hat{\mathbf{d}} \cdot \mathbf{E} \left| {}^1\mathrm{S}_0 \right\rangle / \hbar = \frac{\Omega_L \Omega_B}{\Delta E/\hbar}\,, \tag{3.5}$$

where

$$\Omega_L = \left\langle {}^3\mathrm{P}_1 \right| \hat{\mathbf{d}} \cdot \mathbf{E} \left| {}^1\mathrm{S}_0 \right\rangle / \hbar$$

is the Rabi frequency corresponding to the electric-dipole weakly allowed ${}^1\mathrm{S}_0 - {}^3\mathrm{P}_1$ transition. Equation 3.5 introduces a wide tunability of clock transition. Remarkably, in ${}^{88}\mathrm{Sr}$ with a laser intensity of $2\,\mathrm{mW/cm^2}$ and a magnetic field of about 2.3 mT it is possible to coherently transfer population from ground state ${}^1\mathrm{P}_0$ to ${}^3\mathrm{P}_0{}'$ in about 1 second.

3.5 Clock Spectroscopy in Optical Lattice

The previously presented Red MOT produces an atomic sample at about $1\,\mu\mathrm{K}$ temperature. However, even at this low temperature the spectroscopy of the clock transition ${}^1\mathrm{S}_0 - {}^3\mathrm{P}_0$ is limited by the Doppler effects due to the residual atomic motion [80]. Furthermore the absorption of a resonant photon at 698 nm leads to a recoil frequency shift of $\nu_r = 4.4\,\mathrm{kHz}$. Although both effects are well understood and can be partially reduced by using special techniques such as “Ramsey-Bordé spectroscopy" [81], they finally limit the ultimate accuracy of free-atoms optical clocks [82, 83, 84].

A possible solution to overcome these limiting effects is to tightly confine the cold atomic sample in a region of space. One obvious advantage of this approach is the long interrogation time which eliminates transit-time broadening effects (eq.2.2). For neutral atoms such confinement can be realized holding the atoms in a standing wave pattern of far off resonant laser light, known as optical lattice (subsection 2.2.2). For a potential lattice depth $U_{\mathrm{depth}} > k_{\mathrm{B}}T$ most of the atoms populates the lower vibrational levels (according to Boltzmann distribution), and the atomic motion can be well described in terms of an harmonic oscillator with quantized vibrational energy levels

$$E_n = h\nu_{\mathrm{vib}} \left(n + \frac{1}{2} \right)\,,$$

where ν_{vib} represents the axial trapping frequency (eq.2.29). Remarkably, in the so called “Lamb-Dicke regime" [85], corresponding to the tightly confine-

ment condition

$$\nu_{\mathrm{vib}} \gg \nu_{\mathrm{r}}$$

atoms can not take up photon recoil during the clock spectroscopy, since the minimum energy scale variation is given by $h\nu_{\mathrm{vib}}$. We must say that the total momentum is not lost: in the Lamb-Dicke regime the photon recoil energy and momentum is taken up less by the atom and more by the confining potential. Additionally, if we also assume the clock transition is narrow compared to the trap frequency

$$\gamma_{\mathrm{clock}} \ll \nu_{\mathrm{vib}}$$

then we realize the resolved sideband regime of spectroscopy where the motional sideband ($\Delta n = \pm 1$) are completely resolved from the carrier ($\Delta n = 0$) [86, 87, 88]. Fig.3.6 shows the high resolution spectrum of the $^1\mathrm{S}_0 - ^3\mathrm{P}_0$ clock transition taken by our group in Florence with a stationary ^{88}Sr system [89, 90]. The spectrum is obtained by scanning the frequency of the probe laser at 698 nm [66, 67]. For each clock-excitation frequency the fraction of

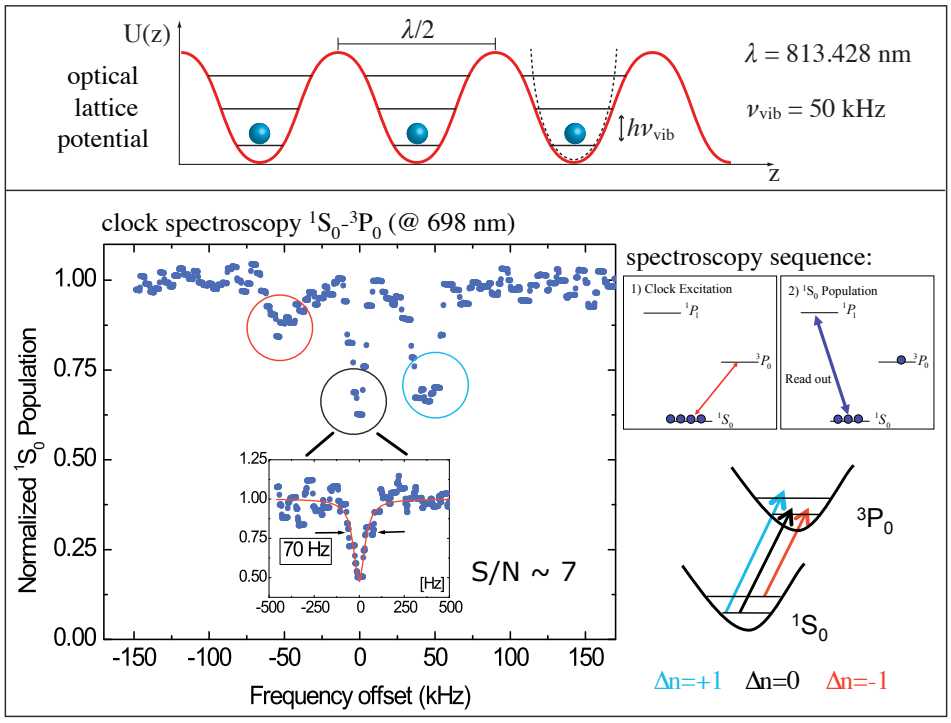

Figure 3.6: Spectrum of the $^1\mathrm{S}_0 - ^3\mathrm{P}_0$ clock transition at 698 nm of ^{88}Sr trapped in 1D optical lattice with $\lambda = 813$ nm taken by our group in Florence with a stationary ^{88}Sr system [89, 90].

atoms left in the ground state $^1S_0$ is measured. This is realized through the detection of the fluorescence produced by atoms illuminated with a resonant beam at 461 nm. The clock transition resonance corresponds to a depletion of the ground state population. The strongest transition is the one where the motional state does not change ($\Delta n = 0$), known as the carrier transition. Transitions where $\Delta n = -1$, known as "red side bands" are suppressed by a factor of $n \cdot \nu_r/\nu_{vib}$. Transitions where $\Delta n = +1$, known as "blue side bands" are suppressed by a factor of $(n+1) \cdot \nu_r/\nu_{vib}$. From the amplitude ratio of the carrier and the first red side band it is possible to measure the atomic sample temperature through

$$\frac{A_{\Delta n=-1}}{A_{\Delta n=0}} \simeq \exp\left(-\frac{h\nu_{vib}}{k_B T}\right),$$

which describes the vibrational ladders Boltzmann population. The spectrum shown in Fig.3.6 is obtained by inducing the clock transition with a static magnetic field $B = 13\,\mathrm{mT}$, with a probe intensity $I = 38\,\mathrm{W/cm^2}$ and with an interaction period $\tau = 100\,ms$. The separation between the carrier and the two sidebands indicates an axial trapping frequency $\nu_{vib} \simeq 50\,\mathrm{kHz}$ ($\gg \nu_r = 4.4\,\mathrm{kHz}$). From the amplitude ratio between the red side band and the carrier we estimated a temperature of $2.6\,\mu\mathrm{K}$. In the inset is shown a scan of the carrier with $B = 1.3\,\mathrm{mT}$, $I = 6\,\mathrm{W/cm^2}$ and the same interaction period. The observed 70 Hz linewidth is limited in this configuration by the induced Rabi frequency of 130 Hz. Remarkably, Lamb-Dicke and resolved sideband regimes allow to perform spectroscopy nearly free of any Doppler or recoil effects. In this way it is possible to access to the $10 \div 100\,\mathrm{Hz}$ induced linewidth of the clock transition in the optical domain at 698 nm and thus to realize a quality factor (eq.1.3) of

$$Q \equiv \frac{\nu_0}{\Delta\nu} = \frac{c}{698\,\mathrm{nm}}/70\,\mathrm{Hz} \sim 6.2 \times 10^{12}.$$

The best strontium lattice clocks have today reached $Q \sim 5 \times 10^{13}$ and (in)accuracy at 10^{-16} level [21, 36, 91] which represent the best performances for neutral atoms to date.

3.6 AC Stark Shift Cancellation

The lattice trapping field, however, can introduce a large perturbation (several hundreds of kHz) to the energy of the clock states $^1S_0$ and $^3P_0$ by the so-called "a.c. Stark shift" (eq.2.25). Therefore the clock transition frequency ν of atoms exposed to a lattice field with intensity I is given by the sum of the unperturbed transition frequency ν_0 and the light shift ν_{ac}

$$\nu(\lambda_L) = \nu_0 + \nu_{ac} = \nu_0 - \frac{\Delta\alpha(\lambda_L)}{2\epsilon_0 ch} I + O(I^2)\,,$$

where ϵ_0, c and h are the permittivity of free space, the speed of light and the Planck constant respectively, and

$$\Delta\alpha(\lambda_L) = \alpha_{^1S_0}(\lambda_L) - \alpha_{^3P_0}(\lambda_L)$$

is the difference between the a.c. polarizabilities of the $^1S_0$ and $^3P_0$ states. Remarkably, this difference depends on the lattice wavelength λ_L. The idea to find a wavelength for which $\Delta\alpha(\lambda_L) = 0$ was firstly proposed by the group of H. Katori in Tokyo [25, 26, 24]. Experimentally they found that ac Stark shift is canceled for $\lambda_L \simeq 813\,nm$ (see Fig.3.7). This solution is very reliable since wavelength is one of the most accurately measurable physical quantity, therefore around this so called "magic wavelength" the light shift can be controlled with 1 mHz precision by simply defining the lattice laser frequency within 1 MHz. Analytical and experimental results agree with the value $\lambda_L = 813.428\,\text{nm}$ [33, 92]. Notably, also this wavelength can be produced by semiconductor based laser technology.

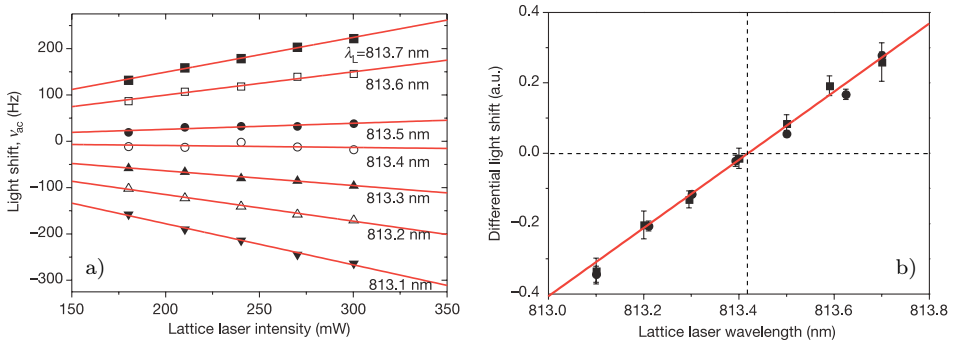

Figure 3.7: [33] a) The light shift ν_{ac} of the strontium clock transition measured as a function of the lattice laser intensity I at several wavelengths λ_L near 813.5 nm. b) The differential light shift $\propto \Delta\alpha(\lambda_L)$ as a function of the lattice laser wavelength λ_L.

Chapter 4

Transportable Apparatus

In this chapter a transportable setup for the production of an ultracold atomic sample of strontium is presented [50]. This work is carried out within the framework of the European project *Space Optical Clocks* (SOC) funded by the *European Space Agency* (ESA). The transportable ultracold strontium source here presented is the core of a full transportable Sr optical clock, which will be realized through the final integration of all the transportable subsystems developed by each member of the SOC team.

4.1 Requirements and Design Solutions

In order to build a transportable setup it is important to analyze which are the particular requests for this kind of application. Starting from this preliminary analysis we have summarized the requests in four main points that have inspired our design. These points are:

- Compact size (volume and weight)
- Hardware modularity
- Low power consumption
- Operation reliability

The need for a compact setup with reduced volume and weight with respect to a stationary system is crucial. In this respect we have organized the transportable system in four compact independent modules: vacuum system, module for laser beams preparation, dichroic fiber port cluster, laser

system for the first cooling stage. In Fig. 4.1 the preliminary design of the transportable system is shown. Here all the modules are fastened on the same optical breadboard (90 cm x 120 cm) but the modularity of the system allows to arrange them in different ways according to the features of the transport vector (truck, plane...).

Another important point is that such apparatus has to be able to operate not only in laboratory but also in remote places and in particular conditions as for instance in a plane for a parabolic flight. For such applications it's necessary to build a very robust system that also requires low electrical power consumption for its operation. For this reason we have developed a new high efficiency atomic dispenser working at high temperature ($> 350\,^{\circ}\mathrm{C}$) with very low power consumption ($\sim 15\,\mathrm{W}$). Additionally, the vacuum has been designed with solutions to reduce the power consumption for the production of magnetic fields needed for magneto-optical-trapping and Zeeman slowing.

Last but not least, this system has to provide a higher operation reliability in comparison with a standard stationary system. This means that it has to ensure a simpler day-to-day operation with high stability of the optical alignments, polarizations and optical power. Concerning this point our approach has been to confine all the needed opto-mechanics for the production of the laser-cooling beams in a compact breadboard. Here new ultra-stable optical mounts have been employed and optical paths have been reduced as much as possible. In this way we have obtained an efficient and stable opto-mechanical device for laser-cooling beams manipulation (power, detuning). All the laser beams are then sent to the atoms by means of optical fibers. These are connected to beam-expanders that are tightly fastened on the vacuum system to ensure the best alignment stability. Following the same approach we have developed a novel “fiber port cluster" to couple into the same fibers the light needed for the first (461 nm) and the second (689 nm) cooling stage.

All this work has been carried out through a careful design process by using 3D software (*SolidWorks*) to study different setup configurations and numerical simulations to optimize magnetic fields for atoms cooling and trapping. In the following sections the realized modules and the adopted novel solutions are presented in detail.

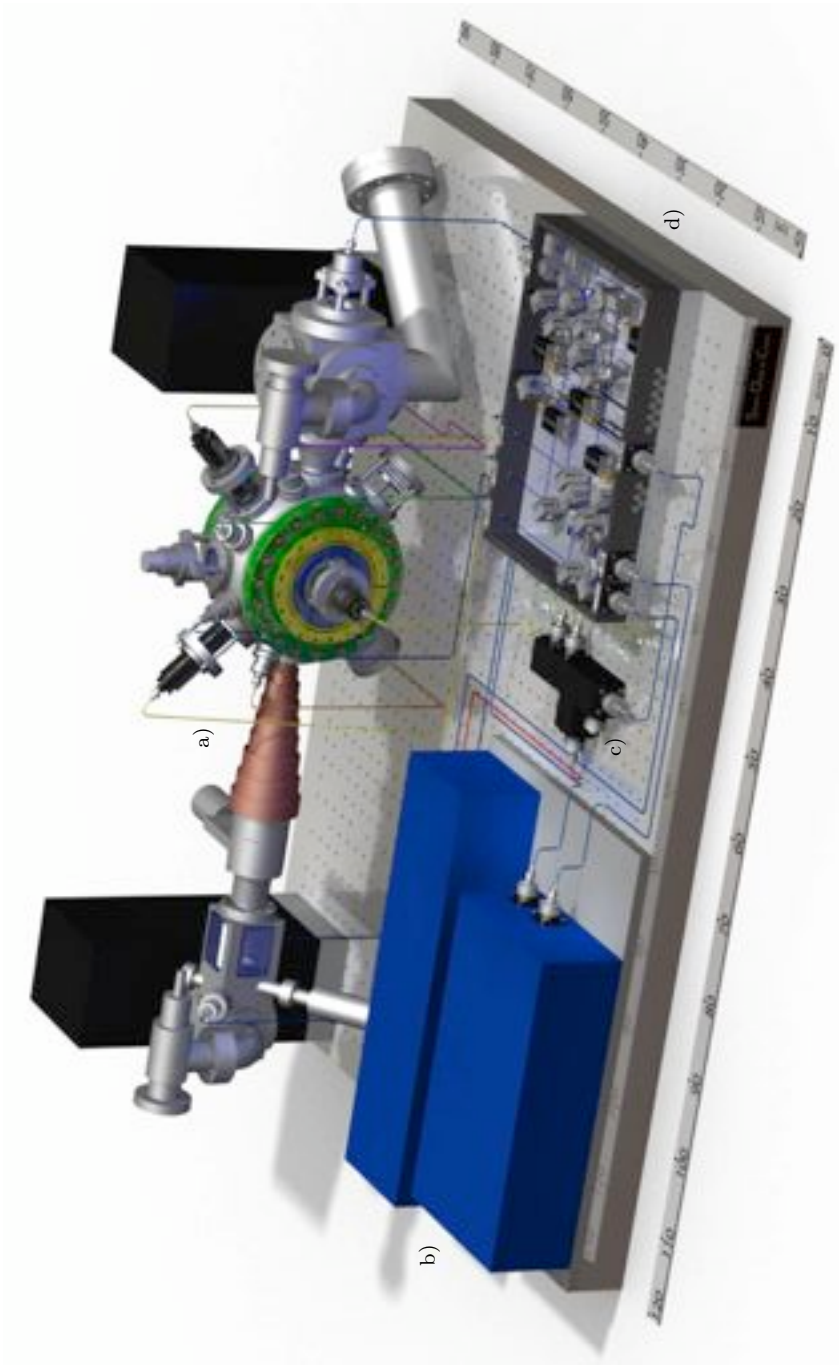

Figure 4.1: Preliminary 3D design of the transportable apparatus for the production of ultracold strontium. The setup is made up of four independent modules linked by optical fibers. a) Vacuum system. b) Laser at 461 nm for the first cooling stage. c) Dichroic fiber port cluster to couple into the same fibers both the lights for first and second cooling stage. d) Compact breadboard for laser beams preparation. All the modules are fastened on the same optical breadboard 90 cm x 120 cm.

4.2 Vacuum system

In order to perform the laser cooling and trapping presented in Chapter 2 we have to avoid collisions between the atoms and the background gas molecules. This means that the slowing, cooling and trapping of atoms have to occur in a vacuum environment. In particular a regime of *Ultra High Vacuum* (UHV) is requested, corresponding to a pressure of about 10^{-9} Torr. Our vacuum system is shown in Fig.4.2. It's basically composed of two main parts: an oven region, where strontium atoms effuse from an hot dispenser, and a MOT region where cold atoms are collected. These two regions are decoupled in terms of background pressure by means of a differential pumping stage. This is realized by inserting between the two regions a tube 7.5 cm long and with an internal diameter of 5 mm (see Fig.A.1 in Appendix A). Such tube ensures a differential pumping ratio of about 1/100. In this way the vacuum in the MOT chamber is preserved by the degassing produced in the oven region by the high temperature (350-400 °C) atomic dispenser. The oven region is pumped by a 40 l/s ion pump (VacIon Plus 40 by *Varian*), while the MOT region is pumped by a 55 l/s ion pump (VacIon Plus 55 by *Varian*) and a titanium sublimation pump (TSP Cartridge Filament Source by *Varian*). With this setup, in operation condition, we achieve a pressure of 10^{-7} Torr in the oven region, and a pressure of 10^{-9} Torr in the MOT cell. The two parts are connected by a gate valve that can be closed if one of the two regions has to be opened to install new windows or recharge the atomic dispenser. Furthermore each part has a valve for independent primary pumping.

Between the oven and the chamber is placed the Zeeman slower in order to slow the thermal atoms coming from the dispenser and increase the loading efficiency of the magneto-optical-trap. This is made up of a series of solenoids wrapped around a steel tube 20 cm long and with an external diameter of 16 mm. This tube contains part of the differential pumping tube. In order to properly align the atomic beam to the differential tube and Zeeman slower tube, the oven is connected to the rest of the system through a flexible joint.

The optical access for the Zeeman slower laser beam is provided by a window on the atomic beam axis. To prevent chimical reactions of strontium and darkening, we used a sapphire window having an anti-riflection coating only on the outer side of the window. Sapphire is an anisotropic crystal that displays substantially different optical charactheristics when measured along different axis. For this reason we have choosen a particular cutting of the

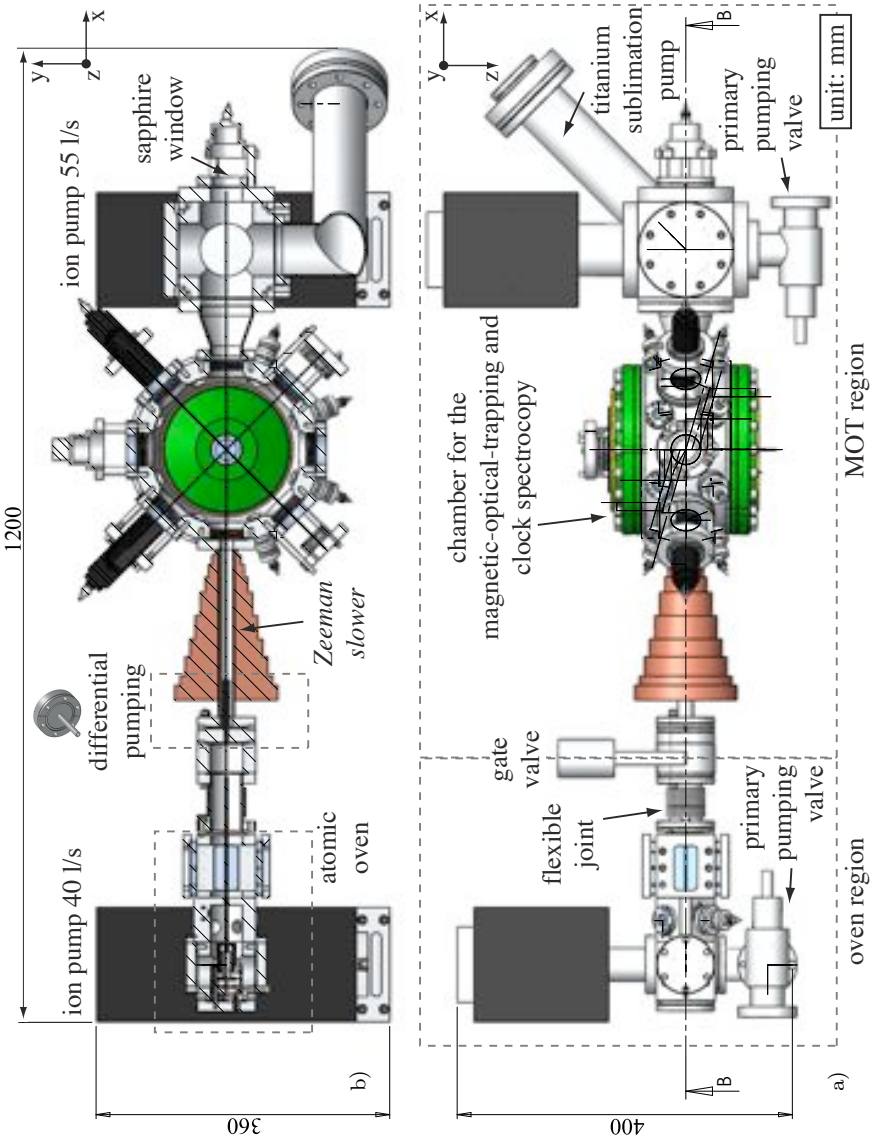

Figure 4.2: Details of the vacuum system in two different views: a) from the above, b) section view. The dashed lines display the two main parts of the vacuum system: the atomic oven region and the MOT region. The size of the vacuum system is about 120 cm x 36 cm x 40 cm, corresonding to a total volume of about 170 liters. See the text for more details.

crystal, called “z-cutting", with crystal orientation parallel to optical axis. In this way the circular polarization of the Zeeman slower laser beam is not perturbed by the sapphire window.

The overall length of the vacuum system is 1.2 meter, 36 cm in height and 40 cm in width, resulting in a total volume size of about 170 liters. The total weigth is about 80 kg.

In the next sections the main parts of the vacuum system are presented in detail, following the atoms trajectory, from the oven, through the Zeeman slower and finally inside the MOT chamber.

4.3 Atomic oven

One of the most critical parts of a cold strontium source is the atomic oven. The vapour pressure of the strontium is quite low (1 mTorr at 1000 Kelvin), so high temperature (350-400 °C) is usually needed to have a resonable number of atoms sublimating from metallic strontium and available for MOT loading. For a tranportable system a high efficiency atomic oven capable to reach such working temperature with the lowest power consumption is needed, providing at the same time a well collimated atomic beam.

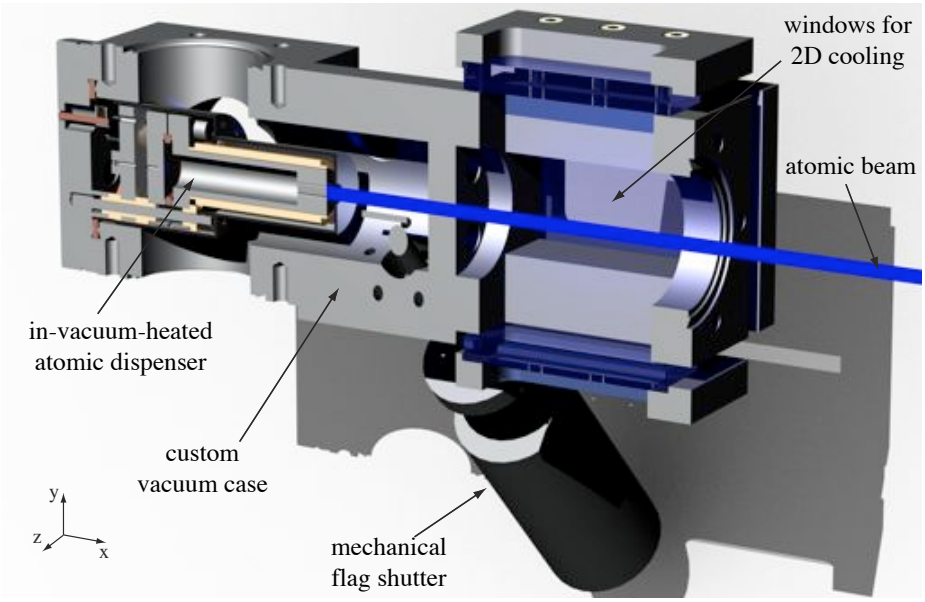

Figure 4.3: Atomic oven. This section view shows the main parts of the oven: 1) the custom vacuum case with integrated mechanical flag shutter and windows for 2D cooling and spectrosopy, 2) the in-vacuum-heated atomic dispenser. The blue line rapresents the atomic beam.

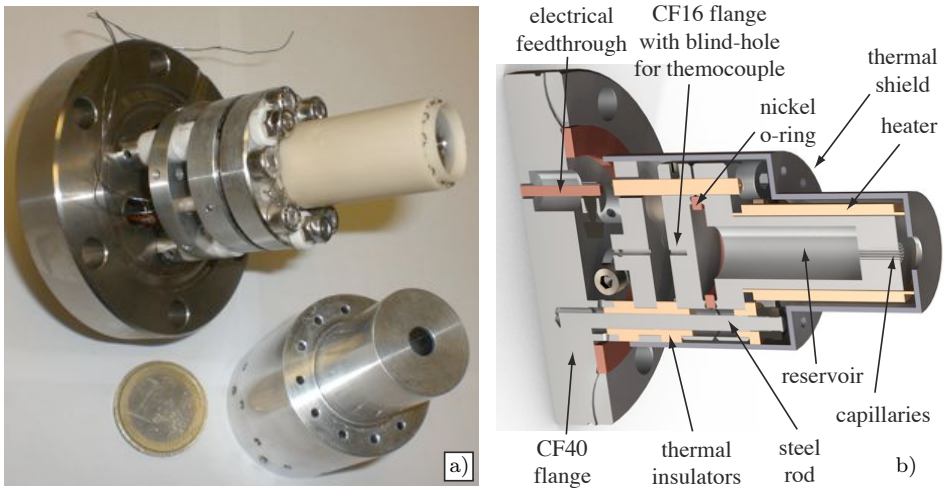

Figure 4.4: In-vacuum-heated atomic dispenser. a) Photo of the assembled dispenser and aluminum black body radiation shield. b) 3D section view of the dispenser. See the text for more details.

The only way to reach high temperatures with low power consumption is to reduce as much as possible the heat dispersion from the heating element at $350 - 400\,°C$ to the environment at $20\,°C$. In this respect our idea has been to avoid the direct contact between the room temperature air and the heater by placing the latter in vacuum. Fig. 4.3 visualizes this idea: a custom made vacuum case, with a certain number of optical accesses, contains an atomic dispenser which is heated in vacuum. This dispenser is basically made up of a stainless steel reservoir (containing the metallic strontium) and the heating element (see Fig. 4.4). This heater is powered by a tantalium wire (by *Euro-Tantalum*) wrapped around an Alumina multibore tube (by *Friatec-Degussit*). Alumina (Al_2O_3) is indeed a good electrical insulator (specific thermal resistance $10^{11}\,\Omega$·cm at 400 °C) and has at the same time a high thermal conductivity (13 W/mK at 400 °C). The reservoir can be filled with about 40 g of metallic strontium and it is surrounded by the heater to have the best thermal contact.

In order to have a collimated beam, about 50 stainless steel capillaries (8 mm long and with an internal diameter of 200 μm manufactured by *Le Guellec*) have been placed at the exit of the reservoir. So only the atoms flowing along the direction set by capillaries can leave the reservoir, thus ensuring a ballistic divergence of the atomic beam of 25 mrad. To minimize the leaking of atoms along the opposite side, the reservoir is hermetically

closed (in vacuum) with a CF16 flange by using the *conflat* sealing standard for UHV regime. A nickel o-ring instead of a copper one has been chosen in order to ensure the tightness of the sealing at the working temperature of $350 - 400\,^{\circ}C$. In this way remaining atoms with random directions are not lost but indeed recycled inside the reservoir until they acquire the right velocity direction to escape through capillaries. This fact implies a longer life-time operation and indeed less frequent recharges of metallic strontium. Furthermore the CF16 flange has a blind hole hosting the hot-junction of a thermocouple (type K by *Thermocoax*) in order to measure the dispenser temperature.

The reservoir is mechanically fixed on a CF40 flange through three stainless steel rods 4 cm long and with a diameter of 3 mm. The thermal contact between reservoir and rods is avoided by means of ceramic thermal insulators. The CF40 flange has vacuum feedthroughs to deliver the current to the heating tantalum wire and for the thermocouple.

By putting the heater in vacuum and by means of ceramic thermal insulators we have limited the heat dispersion by thermal contact but there is still another source of energy dispersion represented by the black body radiation emitted by the hot "reservoir+heater" system. In order to recover the energy lost in this form we have placed the reservoir and the heater inside an aluminum shield. This has the internal surface polished with optical quality. In this way part of the black body radiation is reflected back. Highly polished aluminum has been chosen for its low emissivity coefficient ($\epsilon \sim 0.05$).

The custom vacuum case containing the in-vacuum-heated atomic dispenser has been designed to provide several optical accesses. In particular four square windows 6 cm x 4 cm , sealed with an indium gasket, can be used to perform a 2D transverse cooling in order to further reduce the atomic beam divergence. This is realized by means of two pairs of retroreflected near-resonance laser beams. Other two CF16 windows are available to send and to reflect back a probe beam orthogonal to the atomic beam (see Fig.4.5). In this way it is possible to realize an orthogonal-crossed-beam scheme of spectroscopy. The fluorescence signal is collected through a third CF16 window and it is used to stabilize the frequency of the laser source for the first cooling stage ($\lambda = 461\,\mathrm{nm}$) on the atomic resonance ${}^1\mathrm{S}_0 - {}^1\mathrm{P}_1$. In this way an additional high-temperature strontium vapor cell for laser stabilization is not needed. This solution provides a simpler setup architecture and furthermore avoids the extra-power consumption requested for a vapor cell operation.

Additionally, a mechanical flag shutter has been installed in the custom vacuum case in order to quickly stop, during the clock transition interrogation, both the atoms and the black body radiation produced by the dispenser and coupled into the MOT chamber.

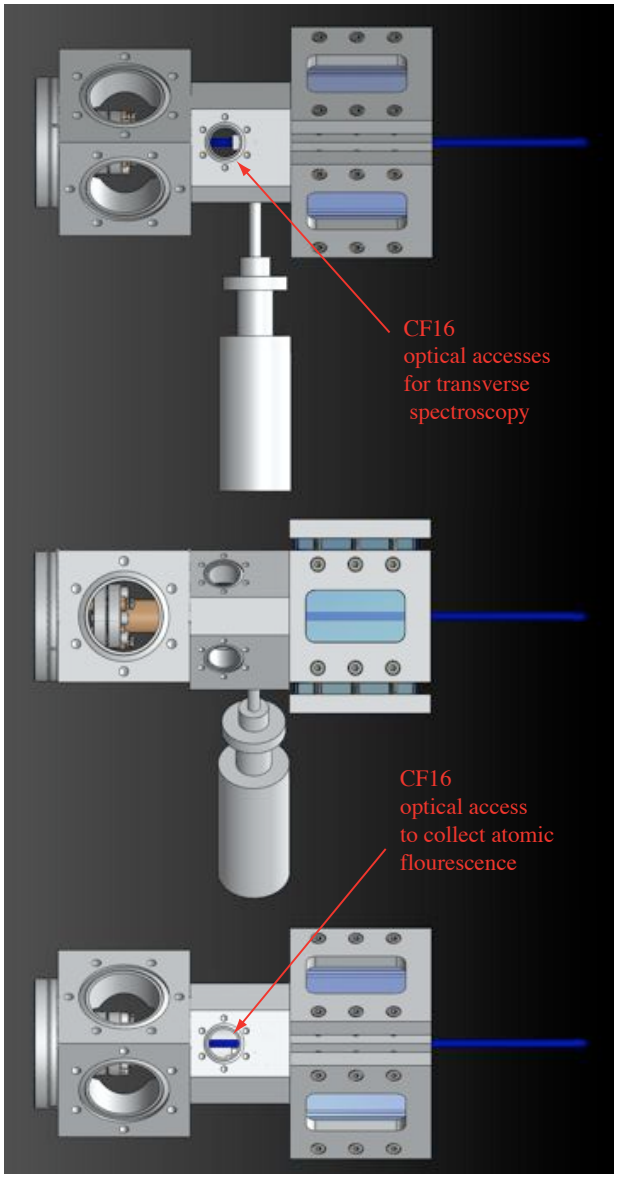

Figure 4.5: Atomic oven as seen from different views. In addition to four square windows for 2D cooling there are three optical accesses to perform an orthogonal-crossed-beam spectroscopy. The fluorescence signal is used to frequency stabilize the first cooling stage laser on the atomic transition $^1S_0 - {}^1P_1$.

4.4 Zeeman Slower

Thermal atoms coming from the dispenser at 350-400 °C have a most probable velocity $v_{\mathrm{i}} = \sqrt{3k_BT/M} \sim 430\,\mathrm{m/s}$ too high to be efficiently trapped into the Blue MOT that has a capture velocity of about 50 m/s. In order to slow down atoms a Zeeman slower has been placed between the oven and the chamber. The operating principle has been already presented in Subsection 4.4: atoms are slowed down by using the radiation pressure of a counter-propagating laser beam with a fixed detuning. Atoms during the slowing dynamics are kept in resonance by a proper magnetic field that shifts their energy levels in order to compensate the variation of the Doppler shift. This is summarized by the condition

$$\omega_0 + \frac{\mu B(x)}{\hbar} = \omega_L + k_L v(x)\,, \tag{4.1}$$

where x represents the coordinate of the axis along the slowing direction. Fig.4.6 shows the experimental realization. Thermal strontium atoms coming from the oven are slowed down by means of a counter-propagating laser beam at 461 nm and with polarization σ^+. The magnetic field shape $B(x)$ obeying eq.4.1 is provided by a series of ten solenoids.

In order to reduce power consumption three main solutions have been adopted. First, these solenoids are wrapped around a stainless steel tube with an external diameter of only 19 mm in order to be as close as possible to the atoms. Then, we have chosen a non zero final velocity $v_{\mathrm{f}} = 50\,\mathrm{m/s}$, according to the capture velocity of the Blue MOT. Finally we have used the x-axis component of the magnetic field needed for Blue MOT operation

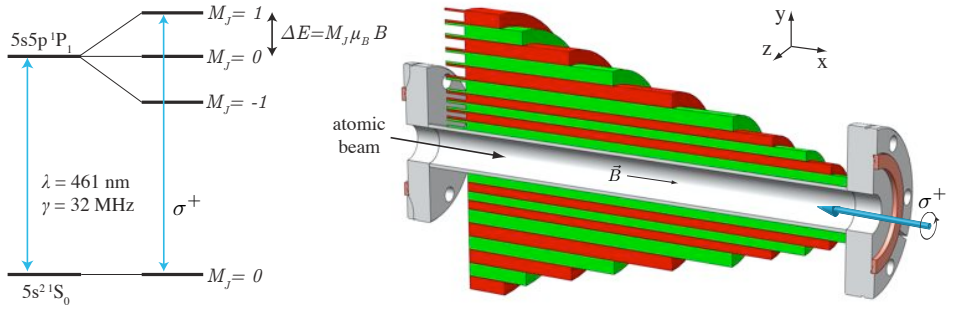

Figure 4.6: Zeeman slowing. A laser beam with $\lambda = 461\,\mathrm{nm}$ and polarization σ^+ slows down thermal Sr atoms coming from the oven. A proper magnetic field, produced by a series of ten independent solenoids, shifts the atomic energy level in order to compensate the variation of the Doppler shift keeping the atoms in resonance during the slowing dynamics.

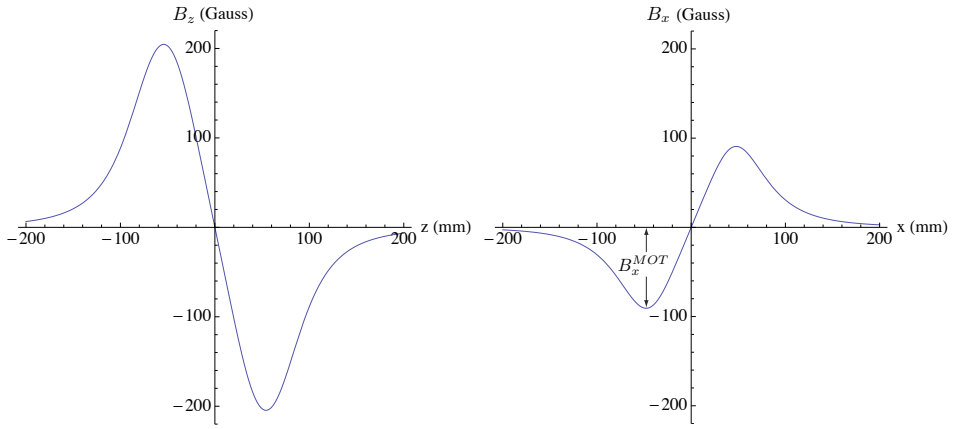

Figure 4.7: Magnetic field produced by coils in anti-Helmholtz configuration placed in the MOT chamber. Both the component along z and x axes are displayed. The latter is used to realize the final part of the Zeeman slowing process. Both z and x axes origins correspond to the MOT position.

to perform the last part of the slowing. As it will be shown in the next subsection Blue MOT needs a magnetic field gradient of about 50 Gauss/cm which is realized by means of two anti-Helmholtz coils aligned along the z-axis. Maxwell equation $\overrightarrow{\nabla} \cdot \overrightarrow{B} = 0$ implies

$$\frac{dB_x}{dx} = \frac{dB_y}{dy} = -\frac{1}{2}\frac{dB_z}{dz}$$

and since in our experimental setup $dB_z/dz < 0$ we have $dB_x/dx > 0$ and therefore a minimum of the magnetic field along the x axis. In operation condition this minimum has the absolute value $B_x^{MOT} \sim 90$ Gauss (see Fig.4.7).

The shape of the magnetic field for Zeeman slowing can be easily found by setting in eq.4.1 a constant deceleration regime given by equation:

$$v(x) = \sqrt{v_{\mathrm{i}}^2 - 2ax}\,,$$

where v_{i} is the initial thermal velocity and a is the atom deceleration. In working condition we have $I = I_{\mathrm{sat}}$ and thus the effective deceleration

$$a = \frac{\hbar k_L}{M}\frac{\Gamma}{4} \sim 5 \cdot 10^5\,\mathrm{m/s^2}\,.$$

For this value of deceleration to reach the final velocity $v_{\mathrm{f}} = 50\,\mathrm{m/s}$ we need a Zeeman slower with a total length given by

$$L = \frac{v_{\mathrm{i}}^2 - v_{\mathrm{f}}^2}{2a} \sim 18\,\mathrm{cm}\,.$$

By setting this values for slowing dynamics in eq.4.1 we obtain the ideal magnetic field shape for our Zeeman slower:

$$B_{\text{ideal}}(x) = B_0\sqrt{1-\left(1-\frac{v_{\text{f}}^2}{v_{\text{i}}^2}\right)\frac{x}{L}} + B_{\text{bias}}\ , \tag{4.2}$$

where $B_0 = \hbar v_{\text{i}}/\mu \sim 665\,\text{Gauss}$ and $B_{\text{bias}} = \hbar(\omega_L - \omega_0)/\mu$. The bias term is fixed by the condition

$$B_{\text{ideal}}(x = L) = -B_x^{MOT} \quad \Rightarrow \quad B_{\text{bias}} = -B_x^{MOT} - \frac{\hbar k_L}{\mu} v_{\text{f}} \sim -167\,\text{Gauss}\ .$$

In this way we have realized a magnetic field with sign inversion having a maximum positive value given by $B_0 + B_{\text{bias}} \sim 498\,\text{Gauss}$ (red curve in Fig.4.8). So our idea of choosing a final velocity close to the MOT capture velocity (instead of $v_{\text{f}} \sim 0$) and of using the off-axis MOT magnetic field for the final part of the slowing dynamics allowed us to save a factor $B_{\text{bias}}/B_0 \sim 25\,\%$ of the requested magnetic field, that in terms of power consumption ($P \propto B^2$) means a reduction of $\sim 44\,\%$.

The magnetic field given by eq.4.2 provides the ideal shape (red curve in Fig.4.8) that has to be matched by the calculated magnetic field corresponding to a certain Zeeman slower geometry (blue curve). There are different ways to design the geometry of the Zeeman slower. Our approach has been to preliminary set the value of the current to 1 A, the overall length to 18 cm, the wire diameter to 1 mm and the external tube diameter to 19 mm. Then we have searched for the geometric configuration of solenoids that best fits with the ideal shape. The geometry of the Zeeman slower has been parameterized in terms of number of solenoids, number of turns along the radial (nR) and axial (nx) direction for each solenoid. The result of this design process is shown in Fig.4.8 where the geometrical configuration accepted as final is illustrated. Notably, the agreement between the ideal shape (red curve) and the calculated magnetic field (blue curve) is very good. The Zeeman slower is very close to the MOT chamber in order to reduce the overall length of the vacuum system.

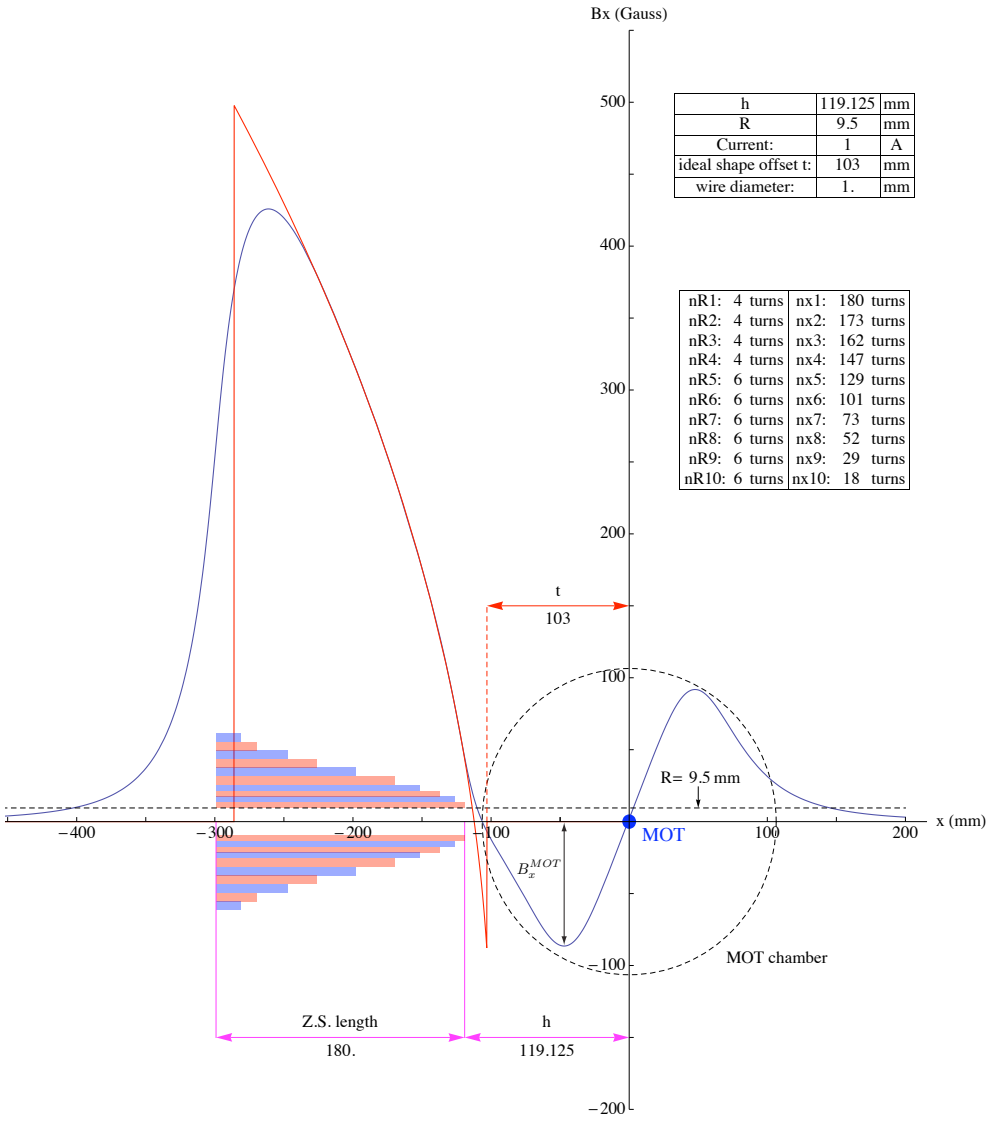

Figure 4.8: Design of the magnetic field for Zeeman slowing. The red curve represents the ideal shape. The blue curve represents the calculated magnetic field produced by ten solenoids. Their geometry is parametrized in terms of turns along the radial (nR) and axial (nz) direction. The black dashed circle represents the MOT chamber with an external diameter of 213 mm.

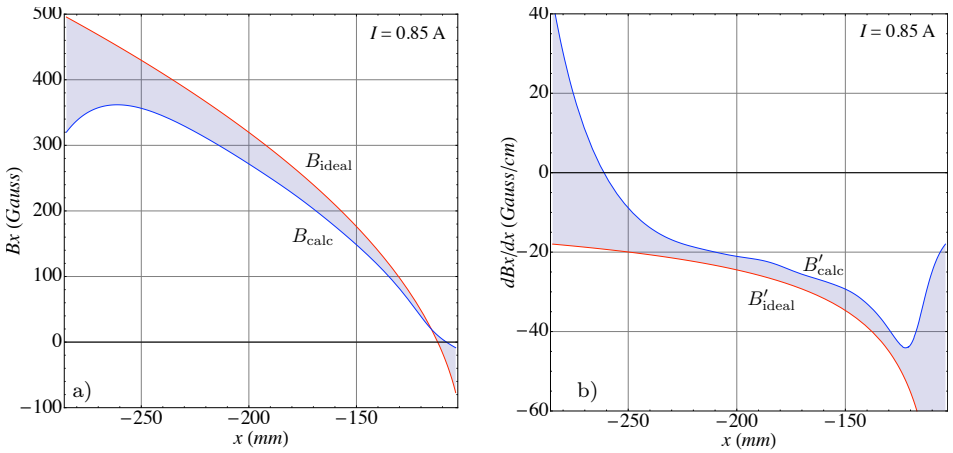

Figure 4.9: a) Ideal shape and calculated magnetic field for $I = 0.85\,\mathrm{A}$. b) Comparison between the slope of the ideal shape and slope of the calculated magnetic field for $I = 0.85\,\mathrm{A}$. The absolute value of the slope for calculated field is lower than that of the ideal shape along all the slowing distance.

Once that the geometry is defined it's important to find the operation current I that realizes the condition

$$\left|\frac{dB_{\mathrm{calc}}(I)}{dx}\right| \leq \left|\frac{dB_{\mathrm{ideal}}}{dx}\right|$$

ensuring that atoms slow down without going out of resonance. This condition is well satisfied by the choice $I = 0.85\,\mathrm{A}$ as shown in Fig.4.9.

To find which is the working detuning $\nu_L - \nu_0$ that maximizes the highest atomic speed slowed down by this configuration of solenoids and current we performed a numerical simulation of the slowing dynamics (see Fig.4.10). We found that for a working detuning of $-317\,\mathrm{MHz}$ atoms with speed up to 390 m/s can be efficiently slowed down to the MOT capture velocity 50 m/s. This speed limit is very close to the most probable velocity 430 m/s leading to a slowing efficiency

$$\int_{0\,\mathrm{m/s}}^{390\,\mathrm{m/s}} f(v)dv \simeq 35\,\% \,, \tag{4.3}$$

where $f(v)$ is the velocity distribution in an effusive atomic beam at $T = 375^\circ\,\mathrm{C}$ given by

$$f(v) = 2\left(\frac{M}{2k_{\mathrm{B}}T}\right)^2 v^3 \exp\left(-\frac{Mv^2}{2k_{\mathrm{B}}T}\right) \,.$$

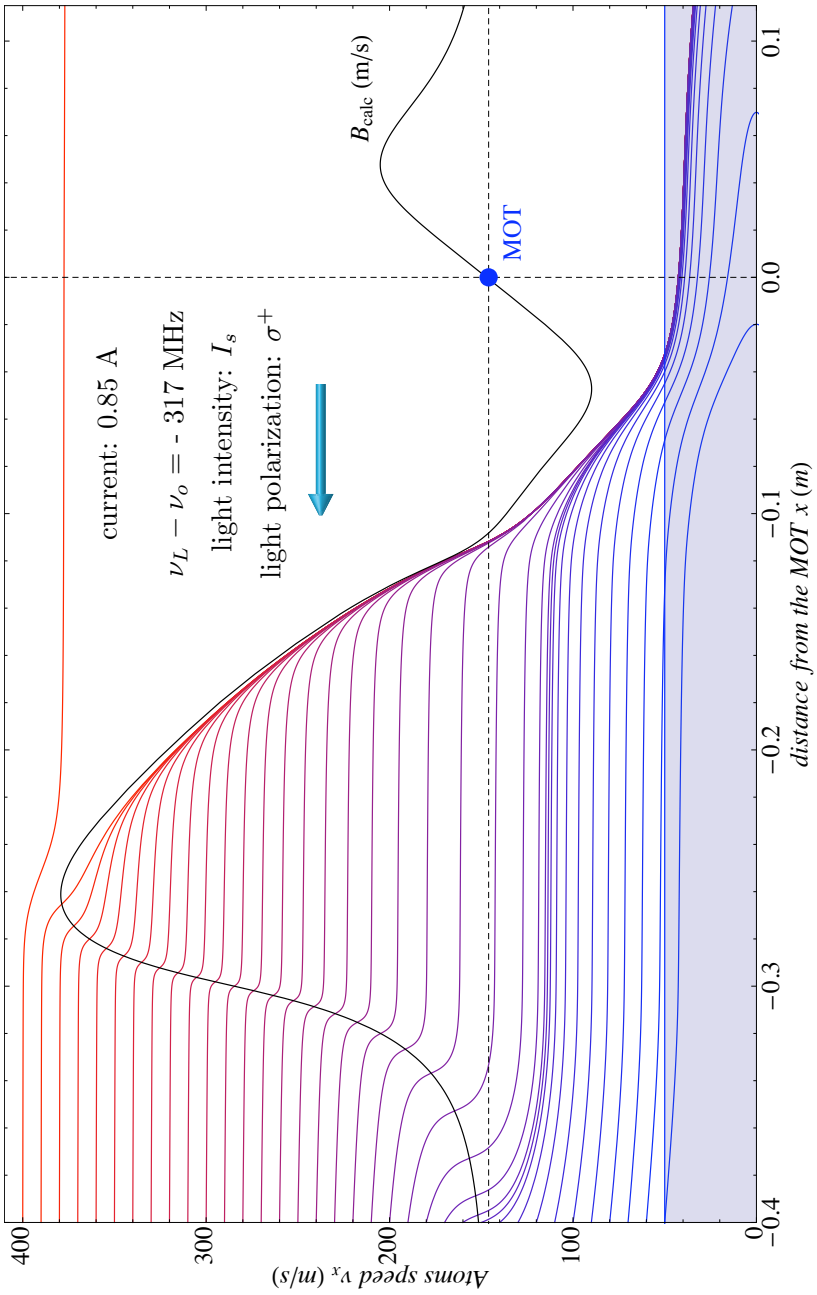

Figure 4.10: Numerical simulation of the atomic Zeeman slowing dynamics. Atoms with different initial velocities (from 50 m/s to 390 m/s) are slowed down to the MOT capture velocity 50 m/s in about 20 cm. The line in black represents the magnetic field of the Zeeman slower and MOT expressed in velocity. This line displays the velocities for which atoms are resonant with the counter-propagating light. The laser detuning $\nu_L - \nu_0 = -317$ MHz maximizes the atom speed that is possible to slow down (390 m/s).

The total length of the copper wire (1 mm diameter) needed to realize this Zeeman slower geometry is 855 m, leading to a total resistance of about $20\,\Omega$ and therefore to a power consumption of

$$P = RI^2 \simeq 14\,\mathrm{W}\ .$$

For this value of power dissipation no water cooling is needed with a further reduction of the setup complexity.

Fig.4.11 displays the experimental realization of the Zeeman slower and its integration with the atomic oven and MOT chamber. The ten solenoids are electrically connected in series but in principle they can be independently powered with ten different currents in order to fine tune the magnetic field shape. The total weight is about 7 kg.

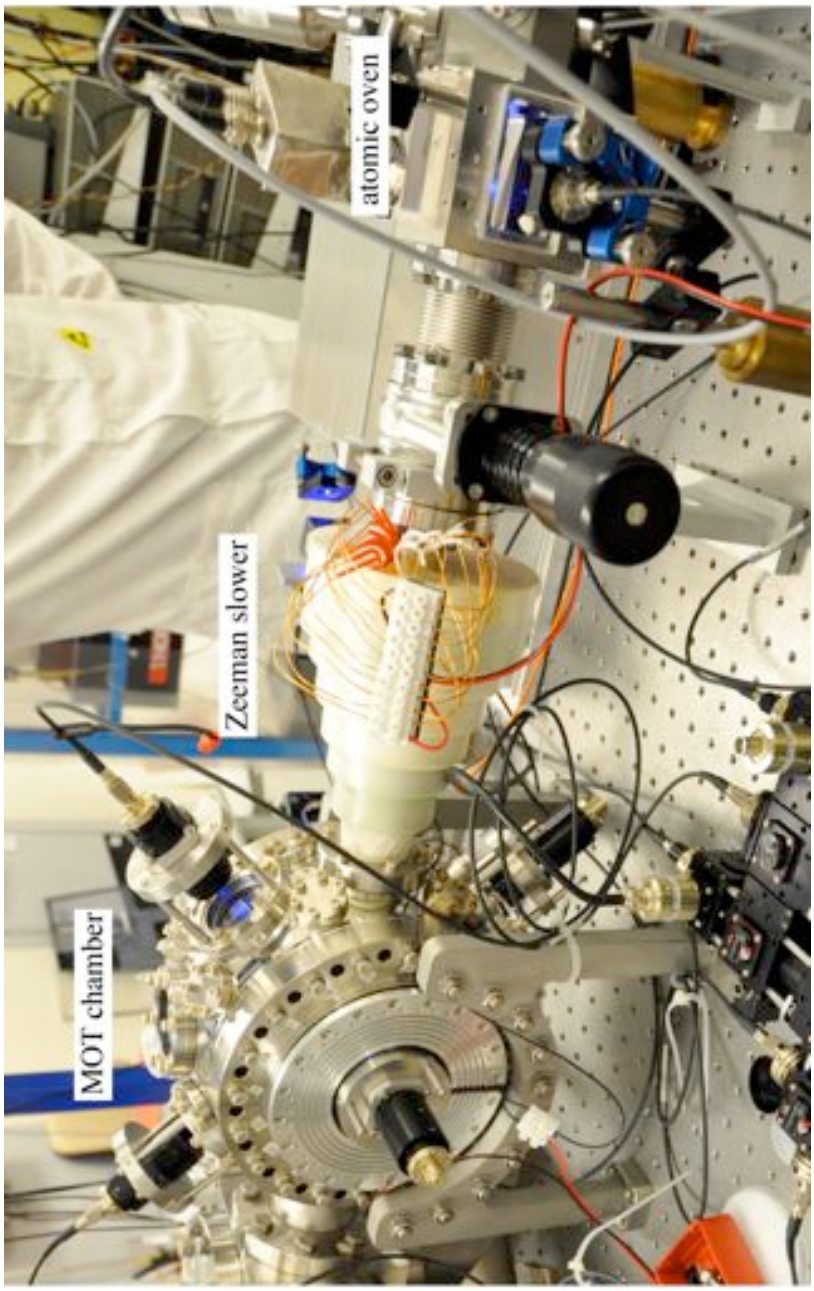

Figure 4.11: Photo of the vacuum system showing the particular of the realized Zeeman slower and its integration with the atomic oven (to the left) and MOT chamber (to the right).

4.5 MOT Chamber

Slowed strontium atoms are trapped and cooled inside the chamber shown in Fig.4.11. This chamber provides optical accesses to perform both the first cooling stage at 461 nm ($T \sim 1\,\mathrm{mK}$) and the second cooling stage at 689 nm ($T \sim 1\,\mu\mathrm{K}$). Additional optical accesses for repumping lasers (679 nm and 707 nm), probing beam (461 nm), optical lattice (813 nm), clock spectroscopy (698 nm) and fluorescence detection (461 nm) are also available. This is a commercial stainless steel UHV cell (by *Kimball Physics*) with an external diameter of 213 mm and 106 mm width, which provides *conflat* sealing surfaces for two CF150 windows, eight CF40 windows and sixteen CF16 windows (see fig.4.12).

The geometric configuration of the laser beams is shown in Fig.4.13. The chamber is connected to the vacuum system through two opposite CF40 accesses. Two CF150 and four CF40 optical accesses are employed to deliver three orthogonal retroreflected beams to atoms in order to perform the two-stage MOT (461 and 689 nm). One of the two remaining CF40 aperture is used for the detection of the atomic fluorescence. Repumpers (679 and 707 nm), probe (461 nm), lattice (813 nm) and clock beam (698 nm) are sent to atoms through the CF16 optical accesses.

Remarkably, due to the geometry of chamber, a 2D lattice can be easily implemented. A 3D lattice is also possible by properly designing the flanges that close the two CF150 accesses.

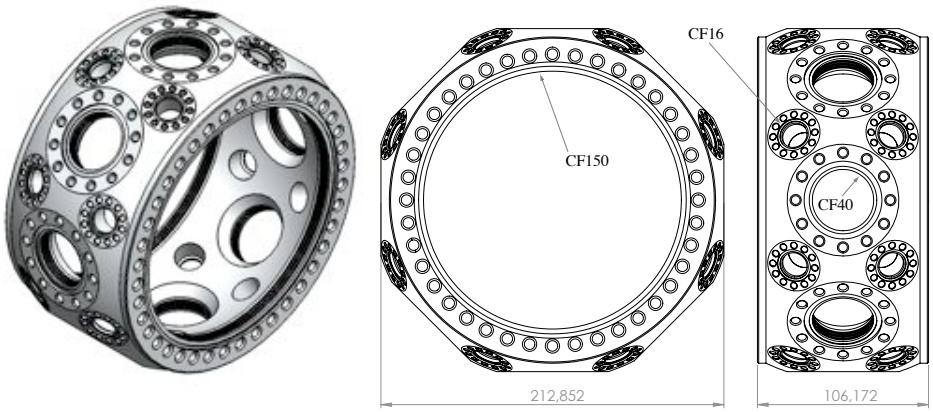

Figure 4.12: Ultra High Vacuum cell for magnetic-optical-trapping and clock spectroscopy. Dimensions are expressed in millimeters. This cell provides several optical accesses with three different kinds of sealing surfaces: n.2 CF150, n.8 CF40 and n.16 CF16.

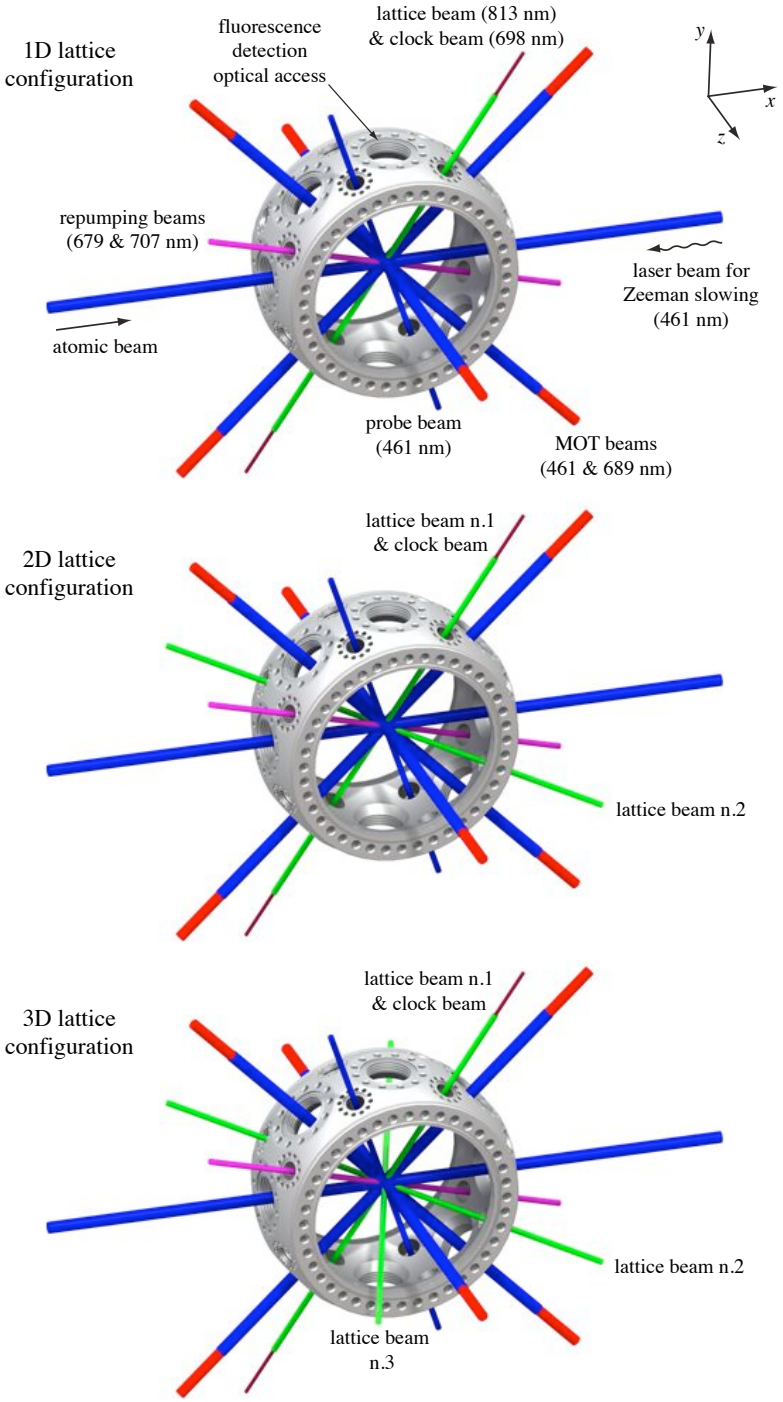

Figure 4.13: Geometrical configurations of the laser beams for cooling, trapping and clock spectroscopy.

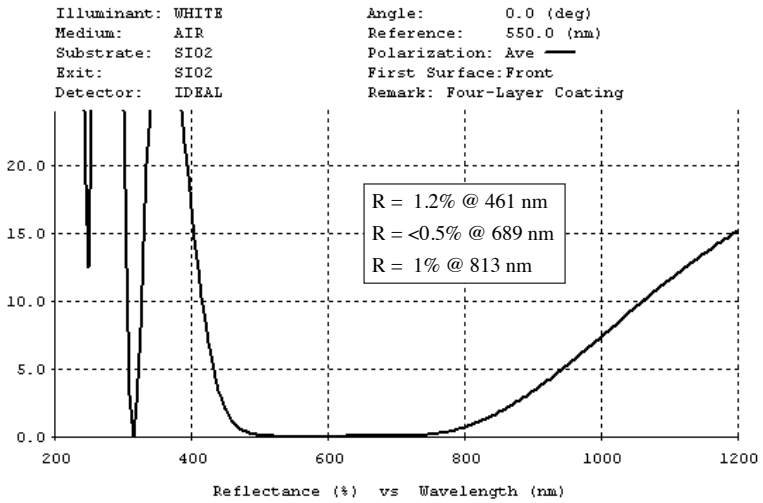

Figure 4.14: Reflectance spectrum of the antireflection coating used for our UHV viewports. A four-layer coating ensures a reflectance level $\leq$ 1% over the wavelength range of interest 461 − 813 nm.

Due to multi-wavelength operation the vacuum chamber has been sealed with broad-band antireflection coated fused silica viewports (by *Caburn-MDC Europe*). Fused silica has been chosen because of its isotropic polycrystalline structure that implies uniform optical properties in all directions and so no change of the polarization of the incoming light. These fused silica viewports have been coated on both sides with an antireflection multilayer coating optimized for the spectrum of interest ranging from 461 nm to 813 nm (reflectance $\leq$ 1%, see Fig. 4.14).

The magnetic field gradient needed for the operation of the Blue and Red MOT is provided by two anti-Helmholtz coils hosted by two custom-made CF150 flanges. These flanges have been designed to minimize the distance between the coils and the atomic sample trapped in the center of the chamber. In this way it is possible to reduce the current needed to realize the typical magnetic gradient of 50 Gauss/cm requested for MOT. This idea is illustrated in Fig.4.15 where these custom flanges are shown in green. Each custom flange provides one CF40 optical access for the retroreflected MOT beam collinear with the magnetic axis of the coils. The minimum distance between atoms and coils is basically set by two constraints. First, custom flanges must not block the CF16 optical accesses. Then, the thickness of the custom flanges has to be sized in order to ensure a mechanical stiffness adequate for UHV sealing. In particular by means of a finite element analysis

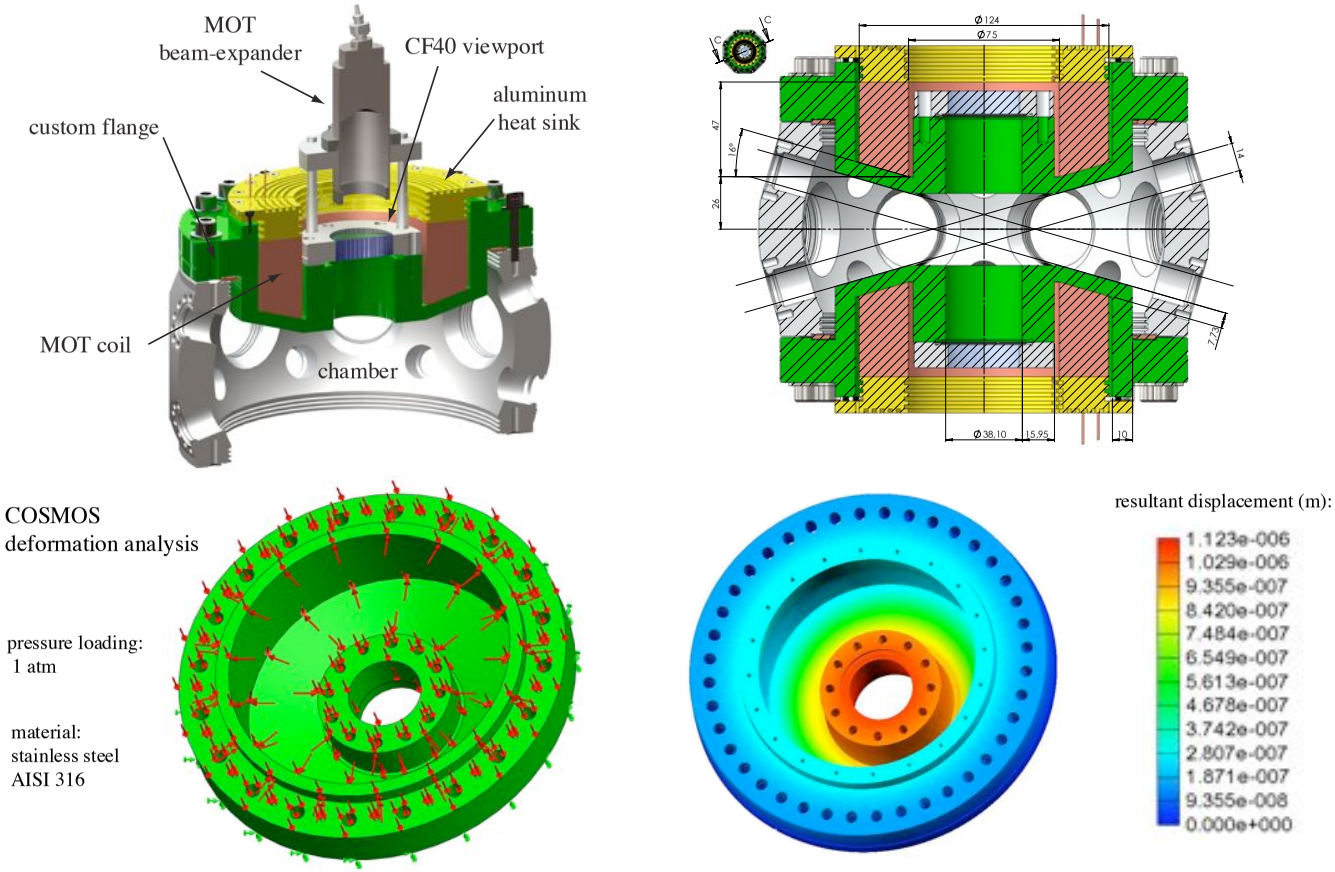

Figure 4.15: Details of the MOT chamber. MOT coils are hosted near the center of the chamber by two special flanges (green). A deformation analysis has been performed to study the mechanical stiffness of these flanges under an external pressure loading of 1 atm.

(through COSMOS software) we studied the deformation of the flange under the effect of 1 atm pressure exerting on the external side. The optimized version of the custom flange has a maximum displacement at the level of about 1 μm, and more importantly it is uniform in the region of the CF40 conflat sealing, thus ensuring a proper UHV sealing. In this configuration the custom flange holds the MOT coil only 2.6 cm far from the atoms. Each coil has been realized with an enameled copper wire of 1 mm diameter wrapped around an internal diameter of 75 mm. The external diameter of each coil is 124 mm and the averaged height is 45 mm, corresponding to a total number of turns of about 1200. This geometry allowed us to reach the needed magnetic field gradient of 50 Gauss/cm with only 1.6 A (at 25 V), corresponding to a total power consumption of about 40 W. Fig.4.16 shows the calculated magnetic field and its slope as a function of the z coordinate.

Each coil has a flat side and a 16° wedge-shape side matched with that of the hosting flange. This gives a simple way to fix the position of the coil: an aluminum plate (yellow part in Fig.4.15) is in contact with the flat side of the coil and presses it against the flange by simply tightening proper screws. This aluminum plate also works as a passive heat sink since it has many folds on the external side to increase the total surface. Therefore due to a power dissipation of only 40 W and to the presence of a passive thermal sink no water cooling is needed, thus reducing the setup complexity.

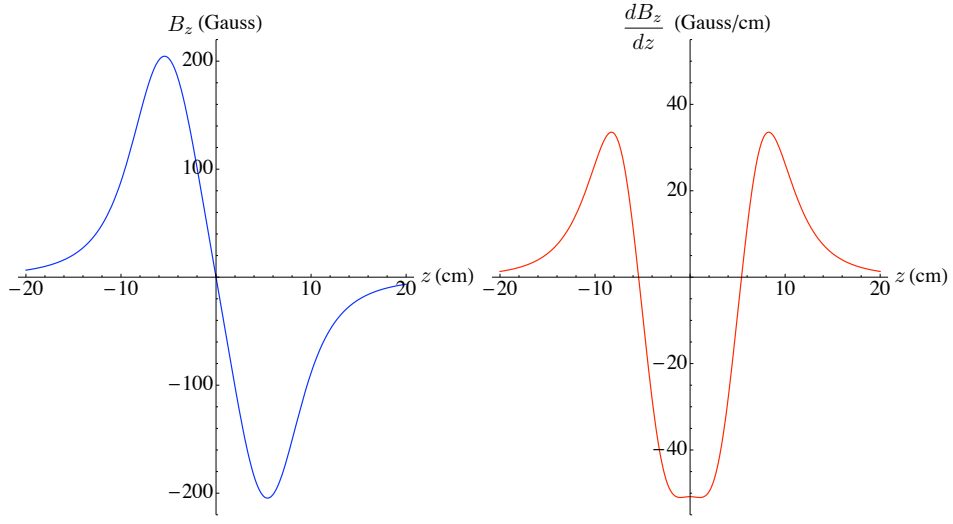

Figure 4.16: Magnetic field and gradient along the z axis produced by MOT coils in anti-Helmholtz configuration.

The light needed for the two-stage MOT is delivered to the atoms by means of fiber coupled beam-expanders that produce gaussian beams with an $1/e^2$ diameter of 10 mm (see Fig.4.17). Each beam-expander has an integrated $\lambda/4$ plate to set the proper circular polarization for both blue (461 nm) and red (689 nm) MOT. In order to ensure the most robust and reliable alignment of the beams to the atoms, these expanders are directly fastened to the vacuum chamber. Fig.4.17 shows in detail the geometry of the beam-expander and the mechanical system to fix it on the cell. In particular the expander is fixed on steel flange sliding on three steel rods, which are screwed on threaded holes of the MOT chamber. The position of this sliding flange can be locked by tightening three screws. A sorbothane sheet between this sliding flange and the expander allows the fine setting of the beam direction by means of three adjustment screws. The final position of the expander can be fixed by means of three locking screws.

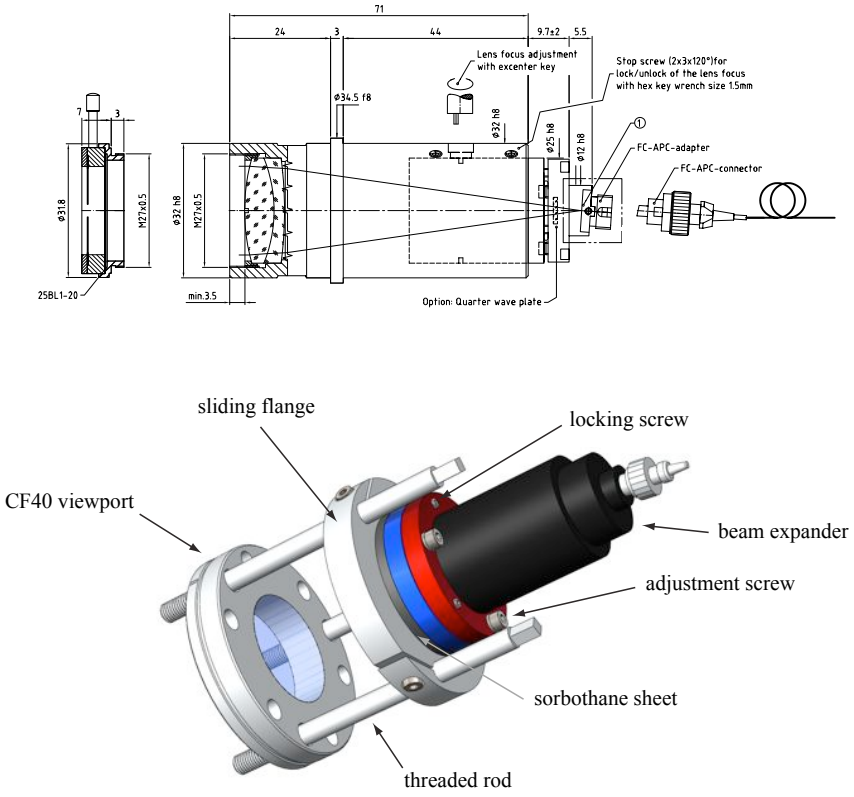

Figure 4.17: Technical drawing and artistic view of a MOT beam-expander. It provides a gaussian beam with a diameter of 10 mm and it is fastened to the MOT chamber.

4.6 Blue Laser for First Cooling Stage

The first stage cooling of strontium atoms is performed by using the strong transition $^1S_0 - {}^1P_1$ at 461 nm. Due to the large saturation intensity on this transition ($I_s = 42.5$ mW/cm^2) usually high power (about 200 mW) laser radiation at 461 nm is requested. Moreover for a transportable device it is also preferred the use of semiconductor devices.

While high power semiconductor laser sources are available in the near infrared region (up to 1.5 W), at the moment no high power blue laser at this wavelength has been developed. The only choice is then to use frequency doubling techniques by employing non-linear crystals.

In the following it is described the compact laser source we developed for the production of more than 200 mW at 461 nm by frequency doubling a high power 922 nm laser source in a non linear crystal. In Fig.4.19 is shown a design of this second-harmonic generation (SHG) laser.

4.6.1 High power infrared master laser at 922 nm

The 922 nm master laser is based on a low power extended cavity diode laser (ECDL) amplified with a tapered amplifier (TA). The ECDL consists of a diode laser at 922 nm placed in a resonant cavity closed by a piezo actuated diffraction grating. This grating is mounted so that the light diffracted in the first order is reflected back into the diode laser, while the light diffracted in the zeroth order is coupled out (*Littrow configuration*). The ECDL typically delivers about 20 mW at 922 nm, it has a spectral linewidth less than

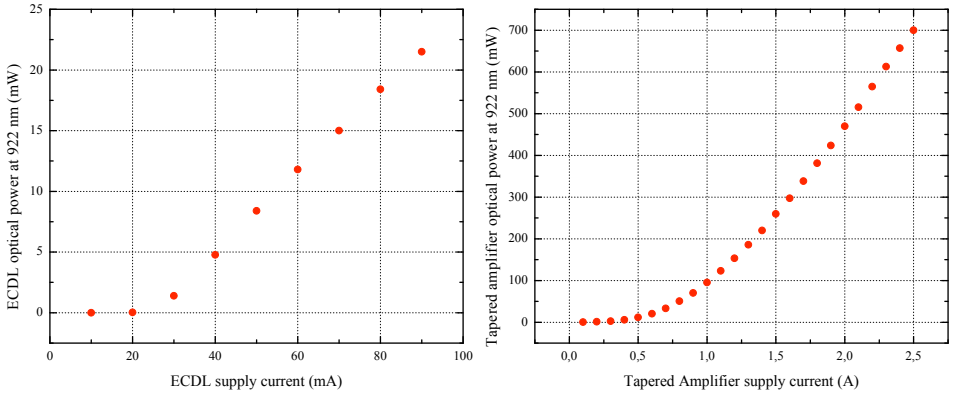

Figure 4.18: Characterization of the optical power at 922 nm. a) Optical power emitted by the ECDL as a function of the supply current. b) Optical power available after the amplification stage as a function of the current supplying the tapered amplifier.

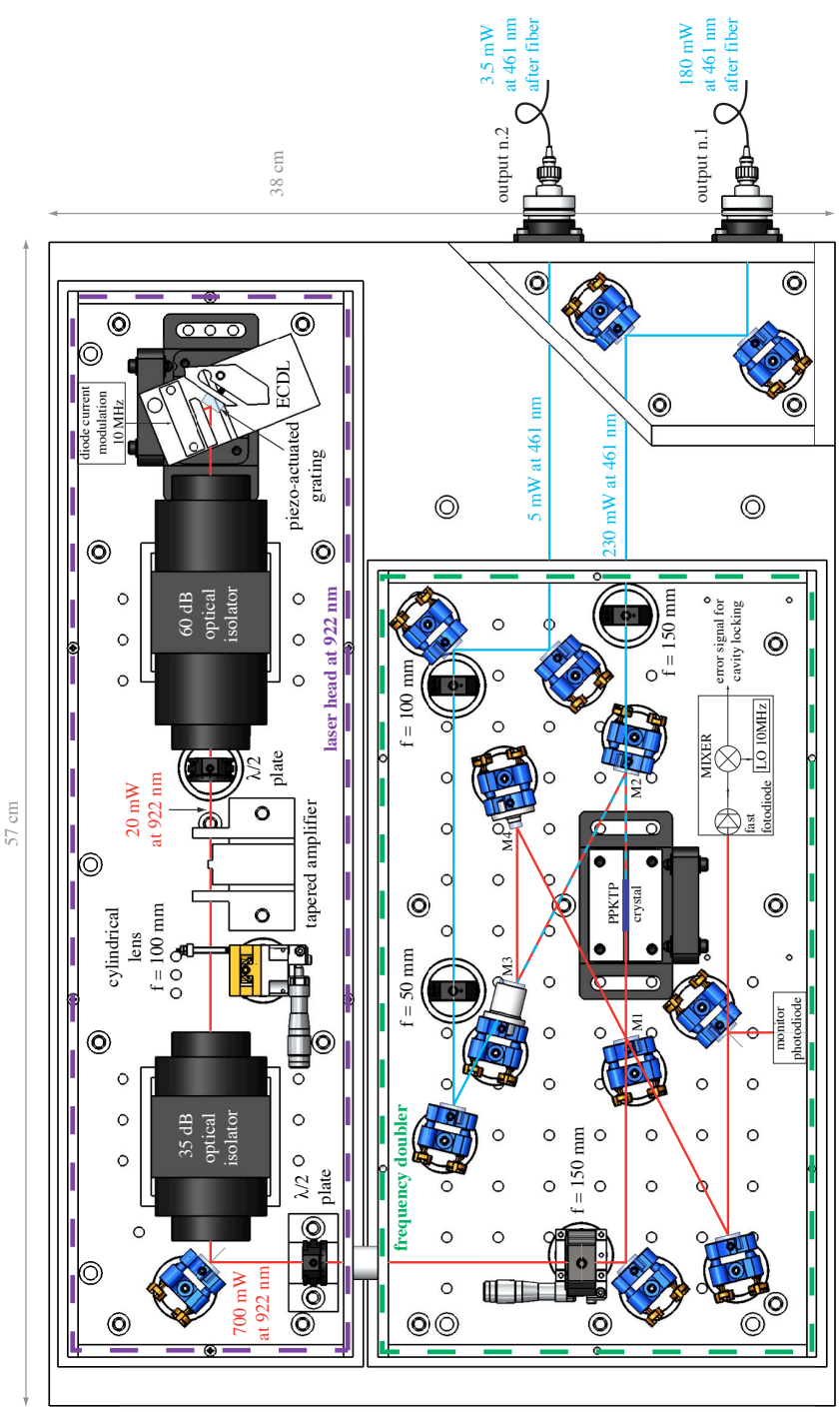

Figure 4.19: Design of the 461 nm laser for first stage cooling of strontium atoms. This module basically is made up of a "laser head" providing about 700 mW at 922 nm and a "frequency doubler" which converts the input infrared radiation into visible light at 461 nm. This light is sent to rest of the transportable system by means of two single mode fibers delivering 180 mW for cooling and trapping and 3.5 mW for laser locking and resonant probing.

500 kHz and its wavelength can be fine tuned by moving the piezo-actuated grating. The light produced by the ECDL is then amplified by a semiconductor tapered amplifier providing in typical operation conditions about 700 mW at 922 nm (see Fig.4.18).

In order to maximize the overall stability of the system and ensure the reliability in the long term operation, two optical isolators have been installed. A 60 dB optical isolator has been placed between the ECDL and the semiconductor tapered amplifier in order to prevent optical feedback in the ECDL, which otherwise could generate frequency instabilities. A 35 dB optical isolator after the tapered amplifier prevents accidental back reflections into the amplifier which could also lead to permanent damages. The laser head at 922 nm is assembled in a box 53.2 cm × 15 cm × 10.5 cm and it provides the radiation to the frequency doubler box (39.5 cm × 22.5 cm × 10.5 cm).

4.6.2 High efficiency frequency doubler

The frequency doubler consists of a 25 mm long periodically-poled $KTiOP_4$ crystal (PPKTP). The crystal facets are antireflection coated both at 922 and 461 nm (R < 0.2%) and the poling period has been chosen to fulfill quasi-phase matching at room temperature [93, 94]. Since the single pass conversion efficiency would not ensure the blue power level requested for first cooling stage, the non linear crystal has been placed inside a four mirrors “bow-tie" resonant cavity which boosts the optical power at 922 nm. For efficient second harmonic generation the spatial mode of the input beam has to match the fundamental mode of the doubling cavity. For this reason a cylindrical lens has been placed between the tapered amplifier and the cavity. The coupling of the input beam into the cavity is further optimized by proper selection of the reflectivity of the coupling mirror M1. This value can be found by setting to zero the reflected power given by [95]

$$P_r = \frac{\sqrt{R_1} - \sqrt{r_m}}{(1 - \sqrt{R_1 r_m})^2} P_i \ ,$$

where R_1 is the reflectivity of the coupling mirror M1 and $1 - r_m$ represents the round-trip losses of the intra-cavity circulating power at 922 nm. Therefore the optimal reflectivity is given by the so called impedance matching condition $R_1 = r_m$. For the cavity shown in Fig.4.20 round-trip losses of 11.5% have been estimated so an input coupling mirror M1 with reflectivity of 88.5% at 922 nm has been used. The other three mirrors of the cavity have a coating with high reflection at 922 nm (R = 99.5%) and high transmission

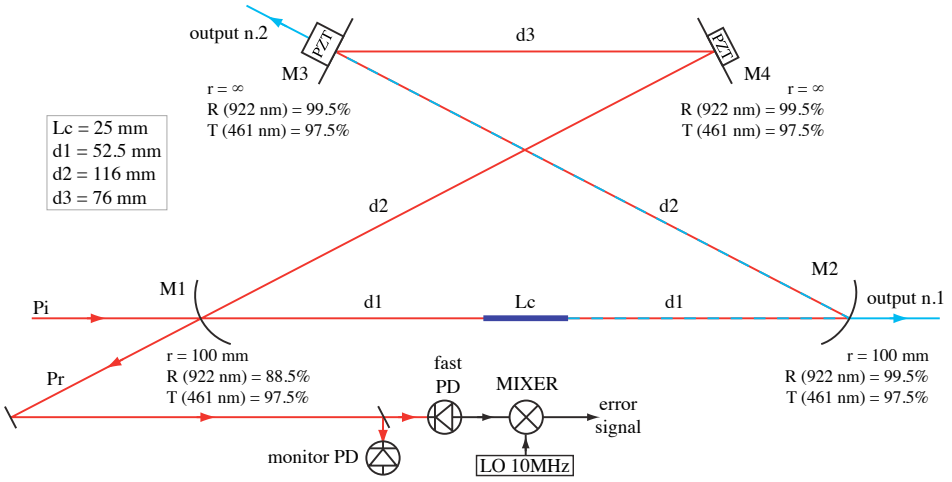

Figure 4.20: Geometry of the "bow-tie" cavity used to enhance the second harmonic generation process. Starting from the radiation at 922 nm provided by the ECDL and then amplified by TA, two outputs at 461 nm are generated. The distances and the details of each mirror are reported. The cavity is kept in resonance with the 922 nm laser by two piezo-actuated mirrors. The cavity length is stabilized by means of Pound-Drever-Hall scheme: the ECDL current is modulated at 10 MHz and the error signal is obtained by demodulating the signal of a fast photodiode detecting the reflection of the doubling cavity.

at 461 nm (T = 97.5%). The doubling crystal is placed between two plano-convex mirror M1 and M2 with curvature radius r = 100 mm. The distance between each mirror and the crystal is d1 = 52.5 mm. The other two mirrors M3 and M4 are plane mirrors and are placed at a distance d3 = 76 mm. The inter-distance M2-M3 and M4-M1 is the same and is given by d2 = 116 mm. This geometry corresponds to a stable configuration of the cavity resonator. The resulting free spectral range (FSR) is given by

$$\mathrm{FSR} = \frac{c}{\mathrm{n}_c \mathrm{L}_c + 2\mathrm{d1} + 2\mathrm{d2} + \mathrm{d3}} = 650\,\mathrm{MHz}\ ,$$

where $\mathrm{n}_c = 1.919$ and $\mathrm{L}_c = 25$ mm are respectively the index of diffraction and the length of the non linear crystal. Fig.4.21 shows the longitudinal modes of the doubling cavity by observing the reflected power at 922 nm.

Under typical operation conditions about 60% of the light is coupled inside the doubling cavity leading to a production of about 230 mW at 461 nm corresponding to a 33% overall conversion efficiency .

The cavity is kept in resonance by two piezo-actuated mirrors M3 and M4. In particular the piezo controlling the M3 mirror compensates the long therm drifts of the cavity length and it has a stroke of about 1 μm/V which is enough to scan many FSR with low voltage. The M4 mirror is actuated

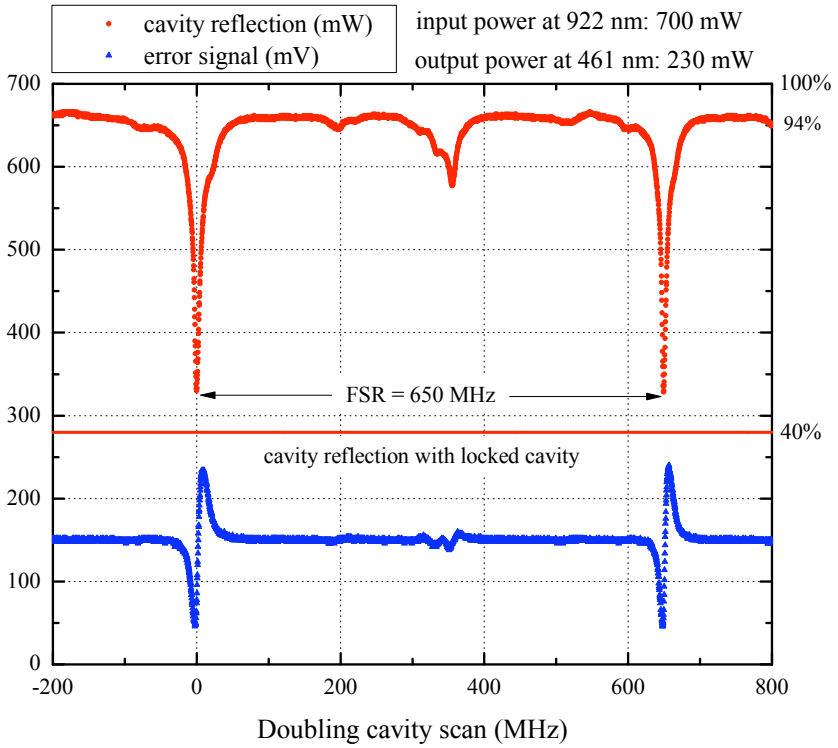

Figure 4.21: Longitudinal modes (red points) of the doubling cavity obtained by changing the cavity length over one FSR and by detecting the reflected optical power at 922 nm. When the cavity is kept in resonance about 60% of the infrared power is coupled into the cavity. The error signal (blue triangles) for cavity locking is also shown in millivolt scale.

by a small piezo (thickness 2 mm) with a high unloaded resonance frequency around 500 kHz providing a high locking bandwidth.

Two different optical outputs at 461 nm are produced, with typical optical power of 250 mW and 5 mW. The spatial mode quality of these beams allowed us to reach very high efficiency in single mode fiber coupling. By matching the beam diameter at 461 nm before and after fiber it has been possible to achieve single mode fiber coupling efficiency higher than 75%. This high coupling efficiency is mainly due to the nature of second harmonic generation process. We have used indeed a *noncritical phase matching* which avoids the spatial *walk-off* and therefore the frequency-doubled beam has the same spatial mode of the incoming beam at 922 nm [93, 94]. In this way more than 180 mW from output n.1 can be coupled into a single mode fiber and sent to the “compact breadboard for beams preparation" which produces all the beams needed for first cooling stage. The output n.2 is also fiber coupled

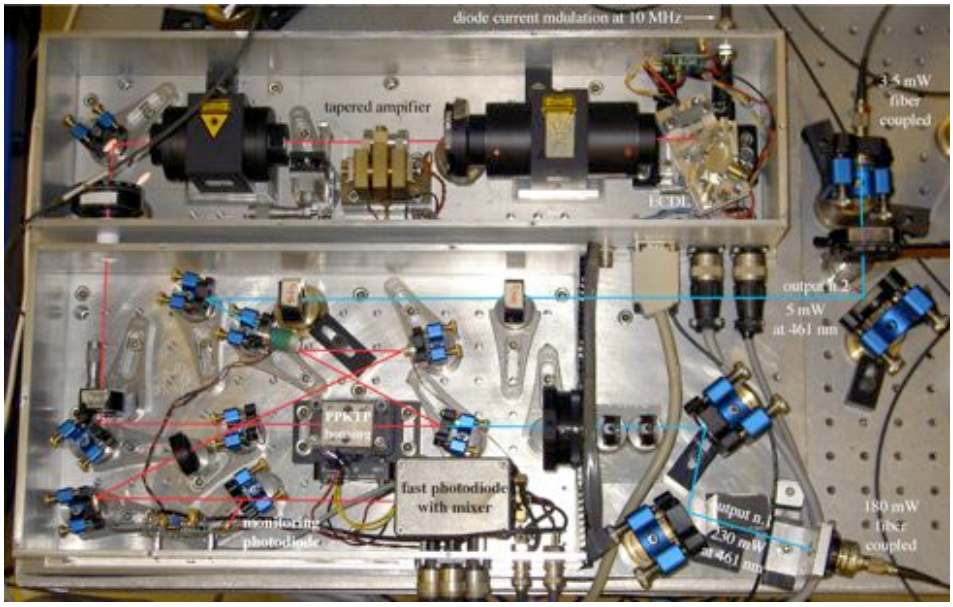

Figure 4.22: experimental realization of the blue laser module.

and typically provides 3.5 mW which are processed by the this module to produce one beam resonant with the cooling transition and one beam red shifted for the stabilization of the blue laser frequency.

Fiber coupling is realized by means of two commercial fiber couplers (by *Schäfter+Kirchhoff*) which have fiber connectors FC. Optical fibers are single mode polarization maintained and are 8°-inclined polish ("APC" standard) to avoid back-reflected radiation into the laser.

Fig. 4.22 shows the experimental realization of the blue laser module. This has been assembled on breadboard 57 cm x 38 cm filling a total volume of about 25 liters and with a weight of 20 kg. The estimated power consumption of the laser source is about 25 W.

4.7 Compact Breadboard for Beams Preparation

Starting from the light produced by the laser at 461 nm several laser beams, with different frequencies and optical power levels, are needed to perform the first cooling stage. More precisely starting from the two blue laser outputs, five beams are needed for Zeeman slowing, Blue MOT operation, 2D cooling, resonant probing and blue laser locking. To provide all these beams a compact breadboard containing all the opto-mechanics for beams preparation has been designed (see Fig.4.24). This breadboard has two optical fiber inputs which tipically deliver 180 mW and 3.5 mW optical power provided by the blue laser. The higher power input is used to produce three beams needed for Blue MOT operation, Zeeman slowing and 2D cooling. The lower power input provides the light for blue laser locking and resonant probing. All the five optical outputs are coupled into single mode optical fibers, which deliver the light to the vacuum system. The beams preparation is realized by means of high-reflectivity mirrors, polarization cubes, plates and lenses. All the different detunings can be tuned by using five acousto-optical modulators (AOM) that shift the frequency of the beams according to the frequency chart shown in Fig.4.23. This compact breadboard has been realized by using compact and ultra-stable opto-mechanical mounts developed for transportable systems in FINAQS and ESA-SAI projects [96, 97].

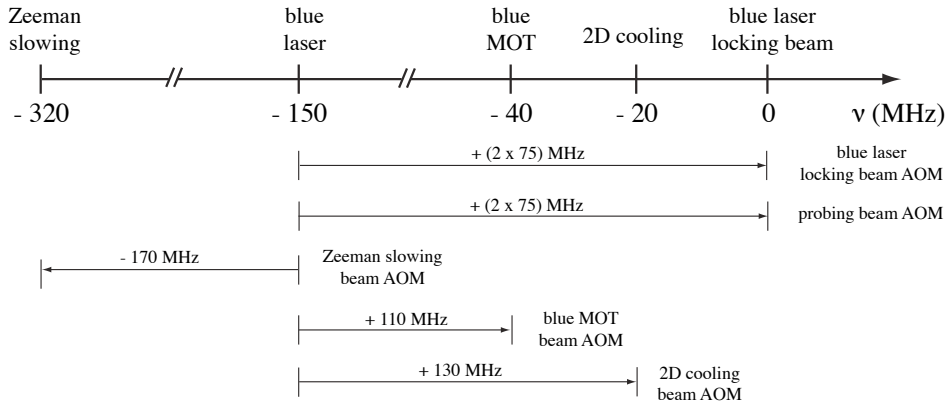

Figure 4.23: Frequency chart for first cooling stage. The light coming from the blue laser (locked at -150 MHz) is shifted in frequency by using acousto-optical modulators (AOM) in single-pass and double-pass configurations.

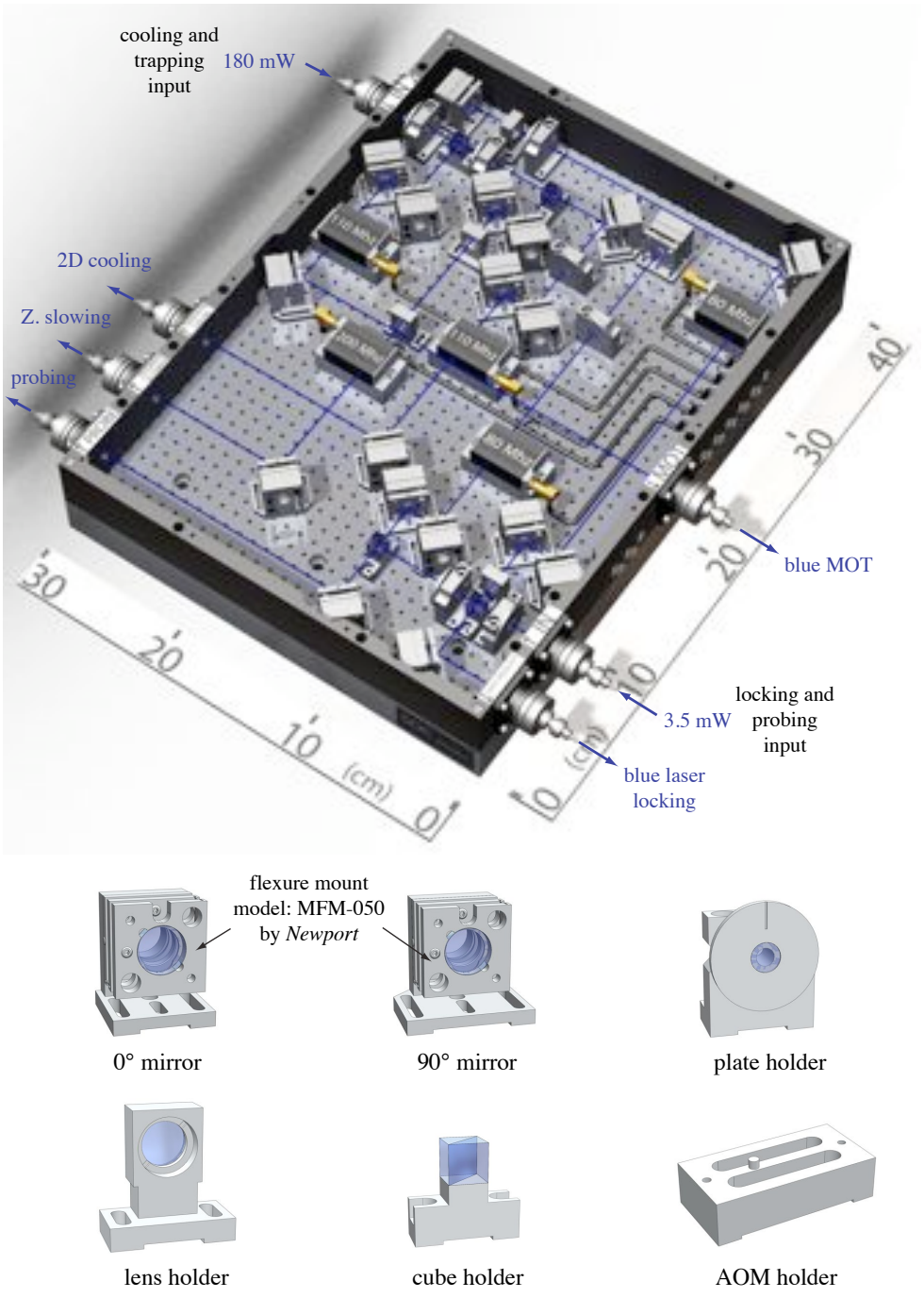

Figure 4.24: Artistic view of the module for beams preparation. This module processes the light coming from the blue laser providing all the beams needed for the first cooling stage. The compact and ultra-stable mounts used in this breadboard are also shown in detail.

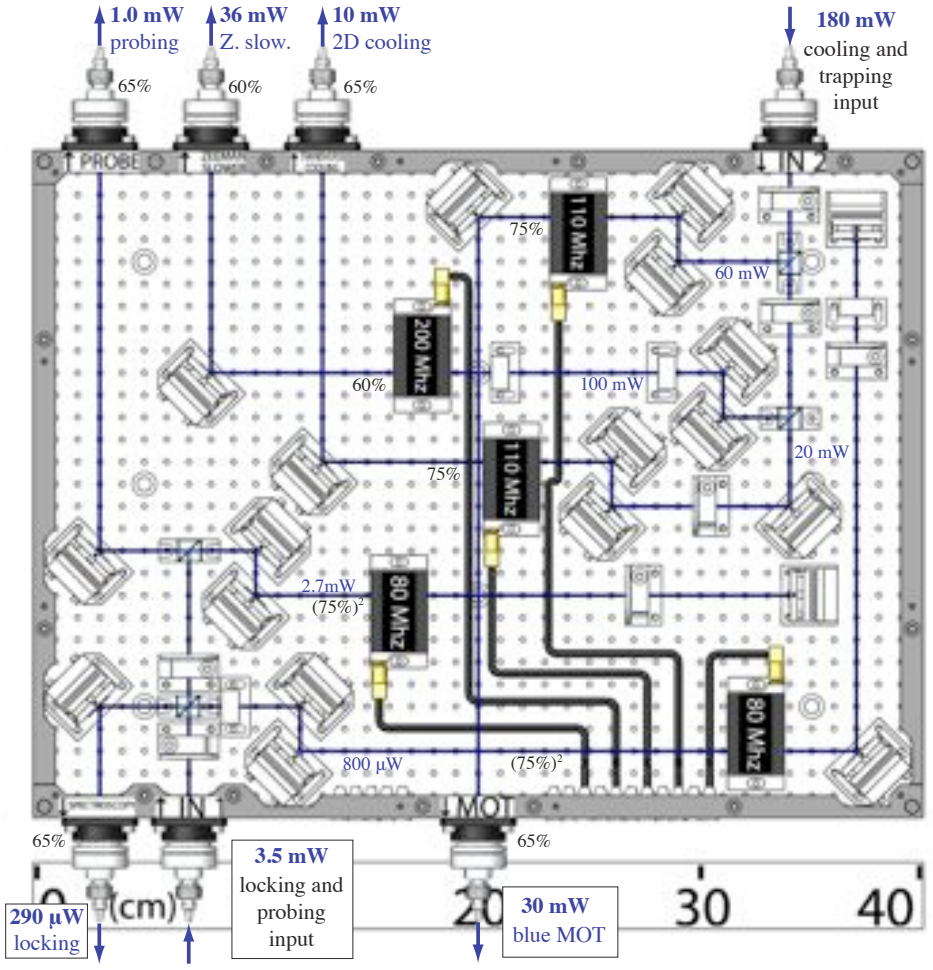

Figure 4.25: Optical circuit of the module for beams preparation. Basically two inputs with 180 mW and 5 mW at 461 nm are processed in power and frequency to obtain 30 mW for Blue MOT, 36 mW for Zeemam slowing, 10 mW for 2D cooling, 1.0 mW for resonant probing (in double pass configuration) and 290 μW for blue laser stabilization (in double pass configuration).

The detail of the optical circuit realized in the compact breadboard is shown in Fig.4.25. Optical paths have been minimized to improve the stability of the alignment. In order to reach high efficiency in AOMs coupling the diameter of the beams has been set to 0.5 mm ($1/e^2$).

Starting from the high power input at 180 mW a series of two polarization cubes and two half-wave plates split the light in three beams for Blue MOT, Zeeman slowing and 2D cooling. The power level of each beam is adjusted by changing the orientation of these two half-wave plates.

Each beam is sent to its AOM with vertical polarization in order to optimize the diffraction efficiency. Indeed a third half-wave plate is placed before the 2D cooling AOM to rotate the horizontal polarization. The alignment of the beams through the fixed AOMs is realized by adjusting the beams direction. This is realized by means of a couple of mirrors placed before each AOM. In typical operation condition the obtained diffraction efficiency in the first order is 75%. Each diffracted beam is then coupled into singlemode fibers by means of a mirror and an adjustable fiber coupler. Optical fibers are connected to fiber couplers by using FC-APC connections. The coupling efficiency of the diffracted beams into singlemode fibers is typically about 65 %.

The light coming from the input at 3.5 mW is split in two beams by two polarization cubes. Again, the power levels are adjusted by two half-wave plates placed before the polarization cubes. Each beam is sent to its AOM with vertical polarization by a couple of mirrors. Here two double pass configurations through AOMs are set. The first provides the beam for blue laser frequency stabilization. In this case double pass configuration is used to frequency modulate the locking beam at 100 KHz. Such frequency modulation allows us to obtain from the atomic beam spectroscopy the error signal suitable for blue laser stabilization. In this configuration the blue laser is stabilized with a frequency offset of -150 MHz. To compensate this shift the beam for resonant probing is produced in a double pass configuration through an AOM driven at the fixed frequency of 75 MHz. Again both the beams are coupled into singlemode fibers by means of two mirrors and two adjustable fiber couplers with FC-APC fiber connectors.

Taking into account all the losses mainly due to AOMs and fibers coupling, starting with two optical inputs of 180 mW and 3.5 mW in normal operation condition about 30 mW are available for Blue MOT operation, 36 mW for Zeeman slowing, 10 mW for 2D cooling, 1.0 mW for resonant probing and 290 μW for blue laser stabilization.

Fig.4.26 shows the experimental realization of the compact breadboard for beams preparation. This breadboard is hermetically closed with an aluminum cover 30 cm $\times$40 cm $\times$0.6 cm. Several electrical channels have also been implemented to deliver radio-frequency to AOMs, to supply eventual shutters and to install photodiodes for power levels monitoring.

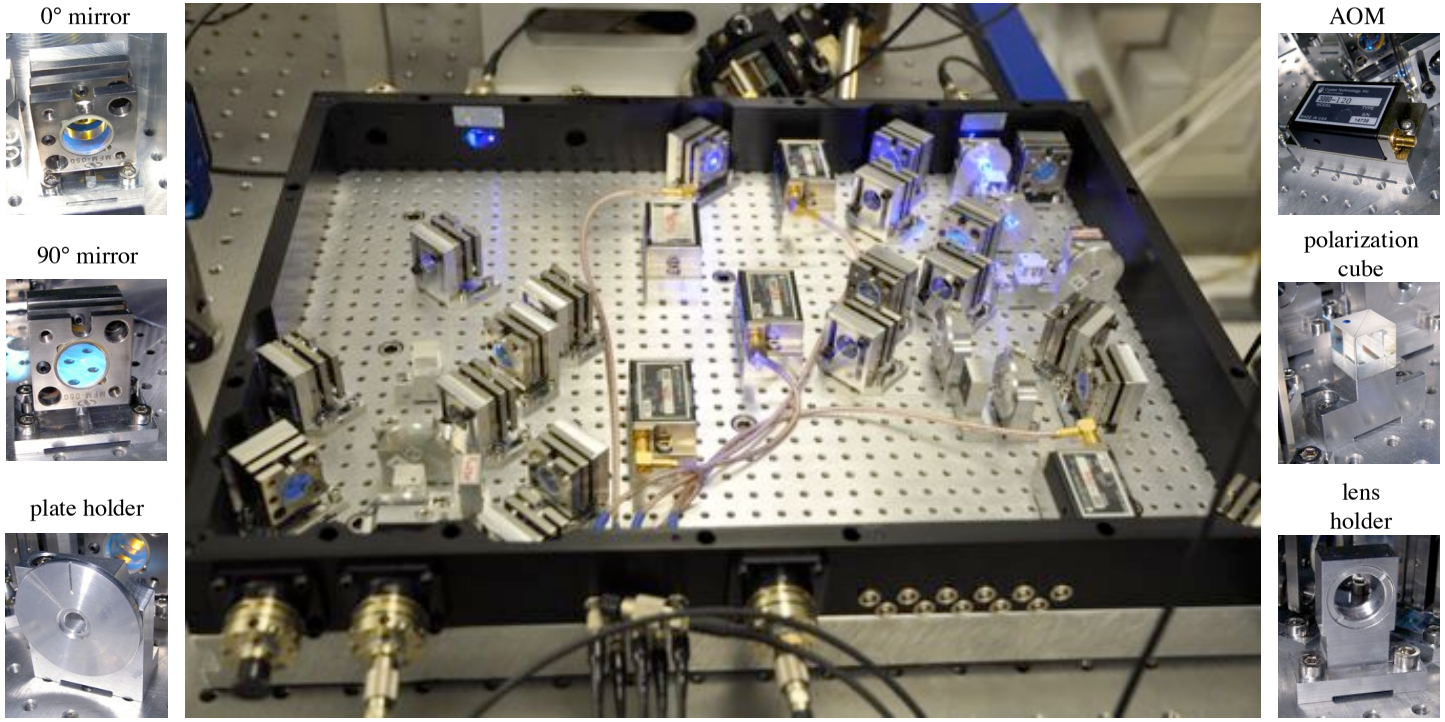

Figure 4.26: Experimental realization of the module for first-cooling-stage laser beams preparation with the detail of the opto-mechanical mounts.

4.8 Dichroic Fiber Cluster for Blue-Red MOT

The light at 461 nm for Blue MOT is sent through optical fibers from the compact breadboard to a dichroic fiber cluster (by *Schäfter+Kirchhoff*). Here the light is split in three beams which are finally sent by fibers to the vacuum system. The dichroic fiber cluster has two optical fiber inputs at 689 nm and one input at 461 nm to couple into the same output fibers both the light needed for Blue and Red MOT (see Fig.4.27). More precisely one input at 689 nm provides the light for Red MOT and the second input at 689 nm ($\sim$ 1.5 GHz red-detuned) provides the "stirring beam" needed for operation with ^{87}Sr atoms. For this isotope indeed the magneto-optical trapping over the $^1S_0 - {}^3P_1$ transition is complicated by the presence of hyperfine states and a "stirring beam" is needed to cycle atoms in hyperfine states well-suited for trapping [98].

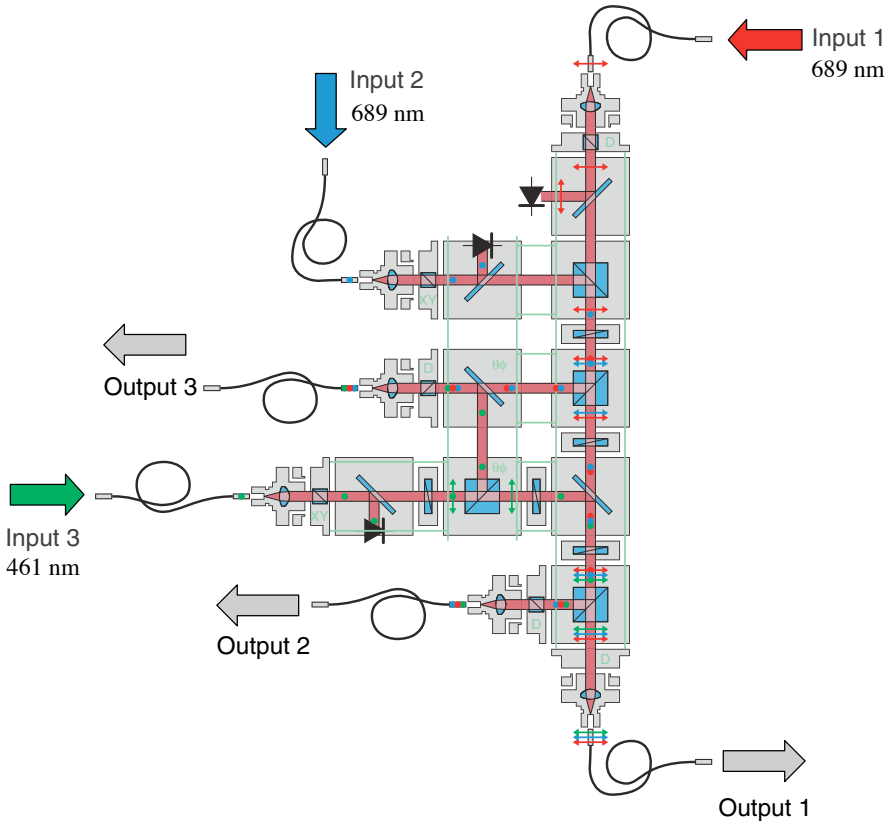

Figure 4.27: Schematic view of the dichroic fiber cluster to couple into the same output fibers the light for Blue MOT, Red MOT and "stirring beam".

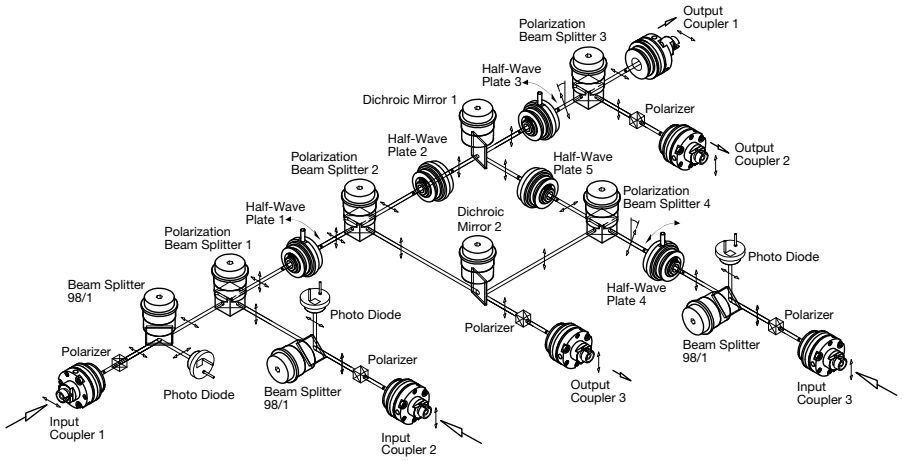

Figure 4.28: Optical scheme of the dichroic fiber cluster.

The optical scheme of the dichroic cluster is given in Fig.4.28. Basically the two lights at 461 nm and 689 nm are coupled together by a dichroic mirror. A number of polarization cubes split the light in three beams for Blue and Red MOT. The power level of these beams can be tuned by adjusting the orientation of two half-wave plates placed in front of polarization cubes. The three optical outputs are fiber coupled into singlemode fibers operating at two wavelength 461 nm and 689 nm and sent to the vacuum system.

In this way the superposition of the beams for Blue and Red MOT is perfect since each beam is produced by the same beam-expander. This should also ensure a better stability and efficiency of the overall cooling process since Blue and Red MOT region are placed exactly in the same position. Additionally, fibers provide gaussian beams with high-quality spatial modes and regular wavefronts such that extra-heating mechanism due to spatial intensity fluctuations of the beams [69] can be largely reduced. Furthermore MOT beams travels in the air for less than 1 cm from expanders to the chamber viewports so spatial intensity fluctuations are strongly suppressed.

This version of dichroic fiber cluster at 461 nm and 689 nm is a first prototype and is currently under study. First tests showed that the overall optical power efficiency is at level of 40% at 461 nm and 50% at 689 nm. Further tests will be performed to study its sensitivity to vibrations and mechanical shocks in order to develop a version well suitable for transportable applications. The optical design can be simplified if we specialized this dichroic only for ^{88}Sr operation, thus eliminating the second input at 689 nm for “stirring beam". This should also lead to a higher optical power efficiency.

Chapter 5

Experimental results

All the sub-sytems presented in the previous chapter have been completed and assembled thus realizing the first transportable cold strontium source. In this chapter such system is presented in terms of the attained Volume-Mass-Power budget. Furthermore, preliminary results of the ongoing system characterization are presented. In particular the atomic dispenser has been tested and the produced atomic beam has been used to realize the first cooling stage. Finally by using an external laser source at 689 nm a preliminary test of the second cooling stage has also been performed.

5.1 Volume-Mass-Power budget

The transportable system has been realized by integrating all the modules presented in the previous chapter: vacuum system, laser for first cooling stage, compact breadboard for beams preparation, dichroic fiber cluster. The result of this integration is shown in Fig.5.1. All the modules have been fastened on a breadboard $0.9\,\mathrm{m} \times 1.2\,\mathrm{m}$. In this configuration we have direct access to each module for optimization. The total volume filled by the transportable setup is about 210 liters. This value is given by the sum of the volume of each module (see Tab.5.1). In the same way the total mass of the system has been estimated to be around 120 kg. The total power consumption is about 110 Watts. These values have to be compared with those of a stationary system. For instance the stationary system for the production of ultra-cold strontium atoms built in Florence has been assembled on a breadboard $2\,\mathrm{m} \times 2\,\mathrm{m}$, is not modular and the vacuum system has a maximum height of about 60 cm. Therefore the volume filled by this system is about 2400 liters, thus a factor of 10 higher than that of the transportable version. In terms of mass we have estimated for the transportable system a reduction by a factor of 3 with respect to the stationary. Furthermore the power consumption of the stationary system results in around 500 W, basically due to the operation of the high temperature oven ($\sim 500\,^{\circ}\mathrm{C}$) and to the production of the magnetic fields for Zeeman slowing and magneto-optical trapping. This means for the transportable system a reduction by a factor of 5 in terms of power consumption.

Transportable system	**Volume ($\mathbf{dm^3}$)**	**Mass (kg)**	**Power (W)**
vacuum system	$12 \times 4 \times 3.6 \simeq 170$	80	80
blue laser	$3.8 \times 5.7 \times 1.2 \simeq 25$	20	25
compact breadboard	$3 \times 4 \times 0.76 \simeq 9$	15	5
dichroic cluster	$3 \times 2 \times 1 = 6$	5	0
total	**210**	**120**	**110**
Stationary system in Florence	$20 \times 20 \times 6 =$ **2400**	$\simeq$ **300**	$\simeq$ **500**

Table 5.1: Final budget of volume, mass and power consumption of the transportable cold strontium source. Analogous values of the stationary system built in Florence are also shown for comparison.

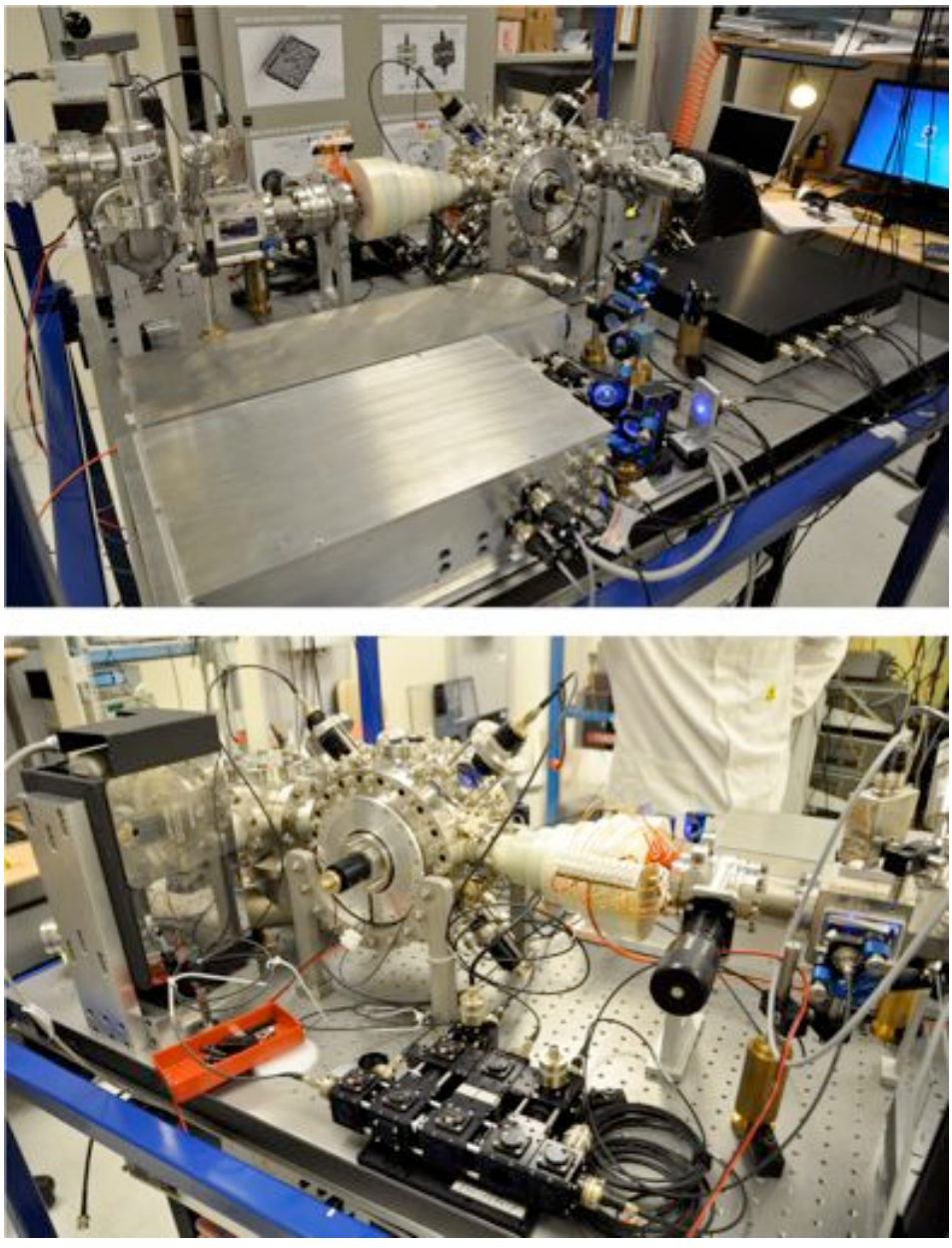

Figure 5.1: Experimental realization of the transportable system for ultra cold strontium atoms production. The system is shown in a front and rear view.

In order to further optimize the volume filled by the transportable system all the electronics needed for the experiment operation has been placed in three consoles hosted under the main breadboard (see Fig.5.2). In this way the free space available under the main breadboard is used and no additional rack for electronics is required. The interface with the user is provided by a single computer that controls the cycle of the experiment.

Figure 5.2: Configuration of the transportable system with all the electronics hosted under the main breadboard.

5.2 Atomic Dispenser Characterization

5.2.1 Thermal properties

The atomic dispenser has been designed to reduce the heat dispersion from the high temperature heater ($\sim 400\,^{\circ}\mathrm{C}$) to the environment at room temperature ($\sim 20\,^{\circ}\mathrm{C}$). To do this several solutions have been adopted. The heater has been placed into the vacuum to avoid the heat transfer to the air at room temperature by convention. Also the heat dispersion through direct contact has been reduced by placing ceramic thermal insulators between the heater and the rest of the vacuum system. Finally the blackbody radiation has also been considered by placing the heater inside an aluminum shield (see 4.3 for further details).

Experimentally these solutions allowed us to realize a high efficient dispenser capable to reach typical working temperature of about $360\,^{\circ}\mathrm{C}$ with a power consumption of less than $17\,\mathrm{W}$ ($1.75\,\mathrm{A} - 9.6\,\mathrm{V}$). The easiest way to model the thermal properties of the oven is to write its equilibrium temperature T_{eq} in the form

$$T_{\mathrm{eq}} - T_{\mathrm{amb}} = R_{\mathrm{th}} \cdot P\,,$$

where T_{amb} is the ambient temperature, P is power consumption and R_{th} represents the overall thermal resistance of the oven. By measuring the

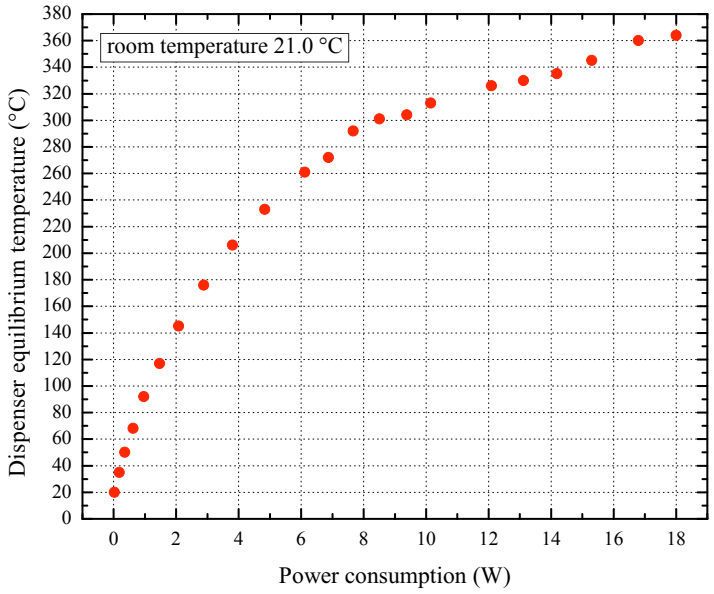

Figure 5.3: Equilibrium temperature reached by dispenser as a function of its power consumption.

equilibrium temperature of the dispenser as a function of the input power P (see Fig.5.3) we have experimentally found that $R_{\rm th}$ is not constant with temperature. At the equilibrium temperature of interest $T_{\rm eq} = 360\,^{\circ}$C the value of $R_{\rm th}$ is about $20\,^{\circ}$C/W. This corresponds to a thermal conductance of the oven (at $T_{\rm eq} = 360\,^{\circ}$C) given by $(R_{\rm th})^{-1} = 5.0 \times 10^{-2}\,$W/$^{\circ}$C.

5.2.2 Atomic beam

The atomic beam produced by the dispenser has been characterized by performing the orthogonal-crossed-beam spectroscopy shown in Fig.5.4. A probing beam at 461 nm with optical power $P_{probe} = 1\,$mW and diameter $d = 5\,$mm $(1/e^2)$ perpendicularly crosses the atomic beam. By changing the frequency of the probe beam around the atomic resonance and by detecting the atomic fluorescence it is possible to measure flux and divergence of the atomic beam.

In these experimental conditions the frequency width of the spectroscopy signal (see Fig.5.5) is not broadened by the finite interaction time τ with light due to the thermal velocity of atoms. At typical dispenser temperature $T = 360\,^{\circ}$C the most probable velocity in the atomic beam is $v = \sqrt{3k_{\rm B}T/M} \sim 420$m/s corresponding to a transit-time broadening given by

$$\Delta\nu_{tt} \simeq \frac{1}{\tau} = \frac{v}{d} = \frac{420}{5 \cdot 10^{-3}} \simeq 84\,\text{kHz}\,,$$

which is indeed less than the natural linewidth $\gamma = 32\,$MHz of the interrogated transition $^1\text{S}_0 - {}^1\text{P}_1$.

Furthermore, for this configuration ($P_{probe} = 1\,$mW, $d = 5\,$mm) the saturation parameter s is very small. This is given by

$$s \equiv \frac{I}{I_s} = \frac{P_{probe}/(\pi d^2)}{43\,\text{mW/cm}^2} \simeq 1.8 \cdot 10^{-2}\,, \tag{5.1}$$

therefore the power-broadening $\Delta\nu = \gamma\sqrt{1+s}$ is also negligible.

Thus in these conditions this orthogonally-crossed-beam spectroscopy allows us to measure the frequency broadening due solely to the atomic beam divergence. The measured frequency width $\Delta\nu_{tr}$ is indeed related with the atomic beam divergence α by the relation

$$\alpha = \frac{\Delta\nu_{tr}}{\Delta\nu_D}\,,$$

where $\Delta\nu_D$ is the Doppler broadening (eq.2.3) which has for $T = 360\,^{\circ}$C the value $\Delta\nu_D \simeq 1.25\,$GHz. Therefore by measuring $\Delta\nu_{tr}$ it is possible to estimate the atomic beam divergence α.

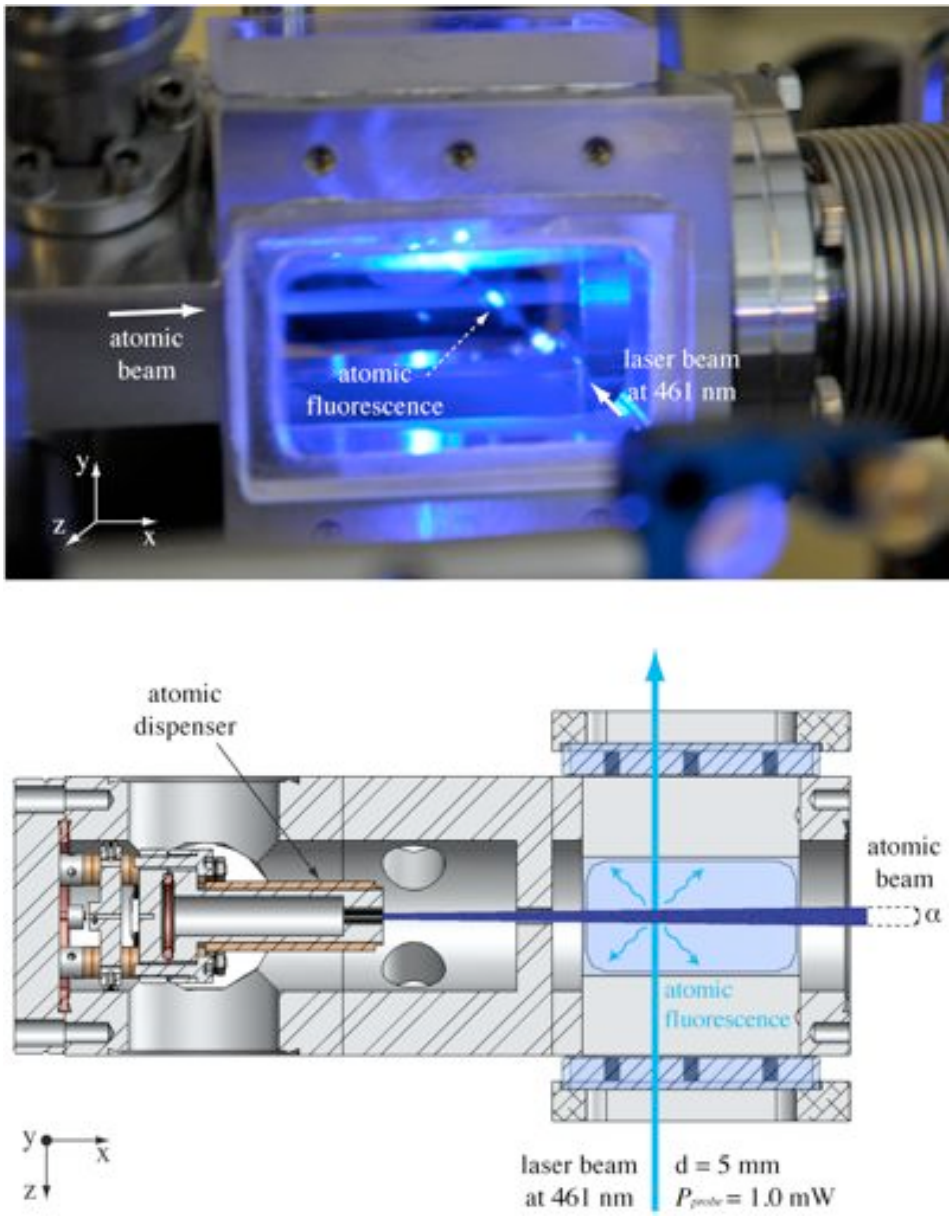

Figure 5.4: Experimental setup of the orthogonally-crossed-beam method for atomic beam characterization and blue laser frequency stabilization.

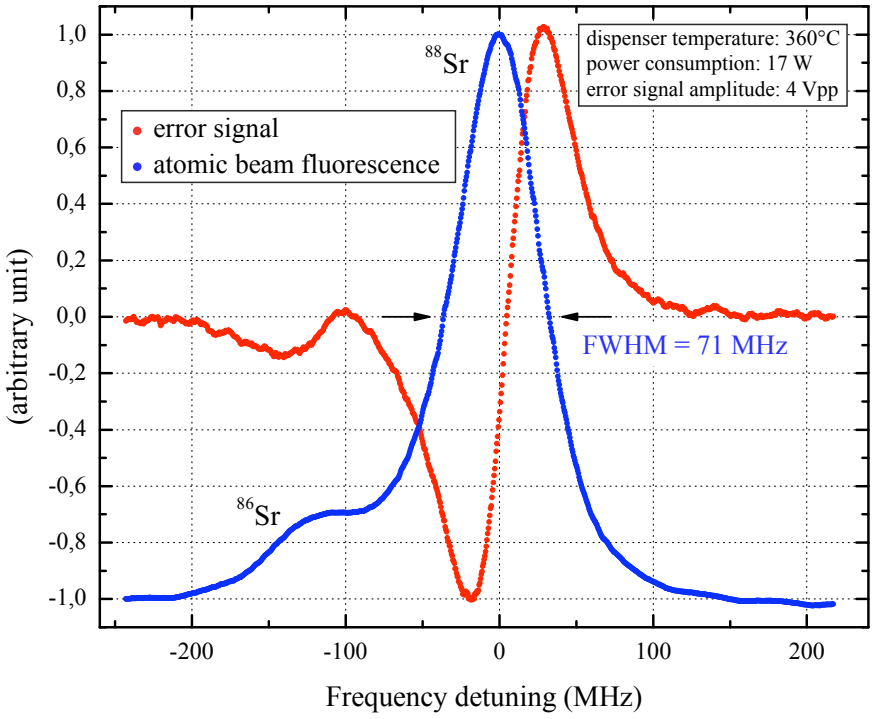

Figure 5.5: Fluorescence signal (blue points) produced by the atomic beam as a function of the frequency detuning of the orthogonal probing beam at 461 nm. Red points represents the corresponding error signal used for blue laser frequency stabilization.

A typical spectroscopy signal obtained by sweeping the blue laser frequency around the atomic resonance transition and by detecting the atomic fluorescence is shown in Fig.5.4. Remarkably, the frequency width of the fluorescence signal is less than the isotope shift $\nu^{88} - \nu^{86} = 124.5\,\mathrm{MHz}$ [99, 100] therefore the signal of each isotope can be resolved. This fact also provides a simple way to calibrate in frequency the x-axis. The resulting width for ^{88}Sr signal is only 71 MHz, which implies an atomic beam divergence of only

$$\alpha = \frac{71\,\mathrm{MHz}}{1.25\,\mathrm{GHz}} \simeq 60\,\mathrm{mrad}\,,$$

so the same order of magnitude of the 25 mrad divergence estimated from the geometry of capillaries.

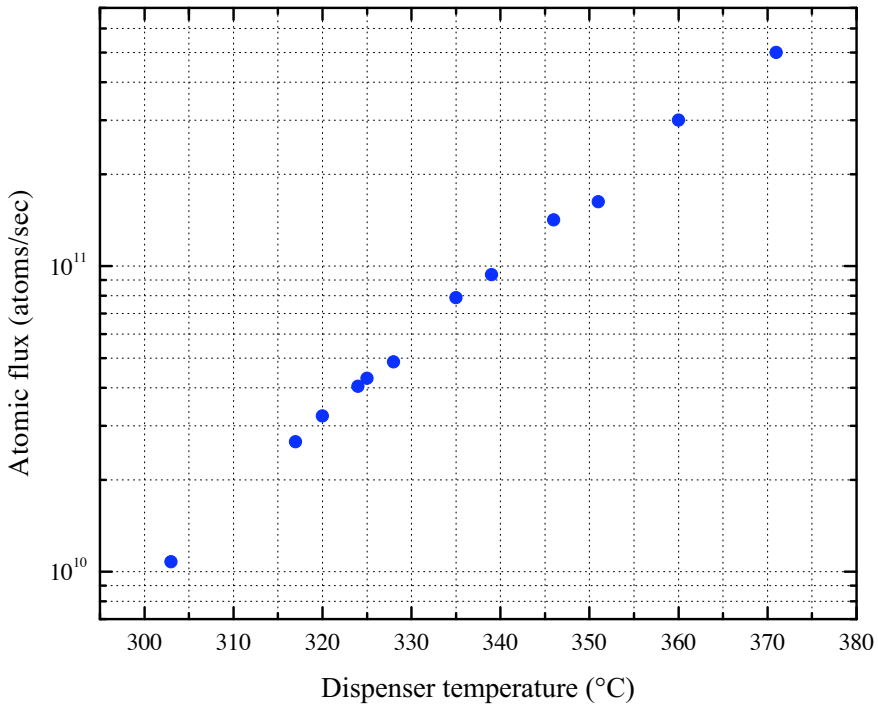

Figure 5.6: Atomic flux produced by the dispenser as a function of its temperature. Flux can be increased by an order of magnitude by increasing the dispenser temperature by $\Delta T \simeq 35\,^{\circ}\mathrm{C}$.

The amplitude of the atomic fluorescence signal can also be used to estimate the flux of atoms produced by the dispenser. The fluorescence optical power P detected by a photodiode is indeed related with the atomic flux ϕ by the equation

$$\phi = \frac{4\pi}{d\Omega}\frac{P}{h\nu\Gamma_{\mathrm{scat}}\tau}\,,$$

where $d\Omega$ is the solid angle as viewed by the photodiode, $h\nu$ is the energy of a photon at 461 nm, Γ_{scatt} is the scattering rate of photons for the $^1\mathrm{S}_0 - {}^1\mathrm{P}_1$ transition (eq.2.5) and $\tau = d/v$ is the transit time. In this way we have estimated a typical flux of about $3 \cdot 10^{11}$ atoms/sec for a dispenser temperature of 360 °C. Remarkably, this high atomic flux is obtained with a power consumption of only 17 W. The atomic flux was measured for different values of dispenser temperature as it is shown in Fig.5.6.

5.2.3 Blue laser frequency stabilization

The width of the fluorescence signal (71 MHz) has the same order of magnitude of the natural linewidth of the $^1S_0 - {}^1P_1$ transition (32 MHz), therefore it is suitable for blue laser frequency stabilization. To do this we have to process the fluorescence signal in order to produce the error signal (red points in Fig.5.4) needed for laser stabilization. This is realized by modulating the frequency of the probing beam at 100 kHz (by means of an AOM in double pass configuration) and by demodulating at the same frequency the fluorescence signal. Finally, the error signal is sent to a PID (Proportional-Integral-Derivative) controller which applies the corrections on the piezo actuated grating of the blue laser (see Fig. 4.19).

A possible angular misalignment $\delta\theta$ of the probe beam with respect to the perpendicular to the atomic beam (see Fig.5.7) should introduce a frequency shift given by

$$\delta\nu \simeq \Delta\nu_{tr} \cdot \delta\theta \sim 70\,\mathrm{MHz/rad}\,,$$

which is valid for $\delta\theta < 1\,\mathrm{rad}$. Previous equation states that a maximum misalignment of about 3° can be tolerated to have a resulting frequency shift

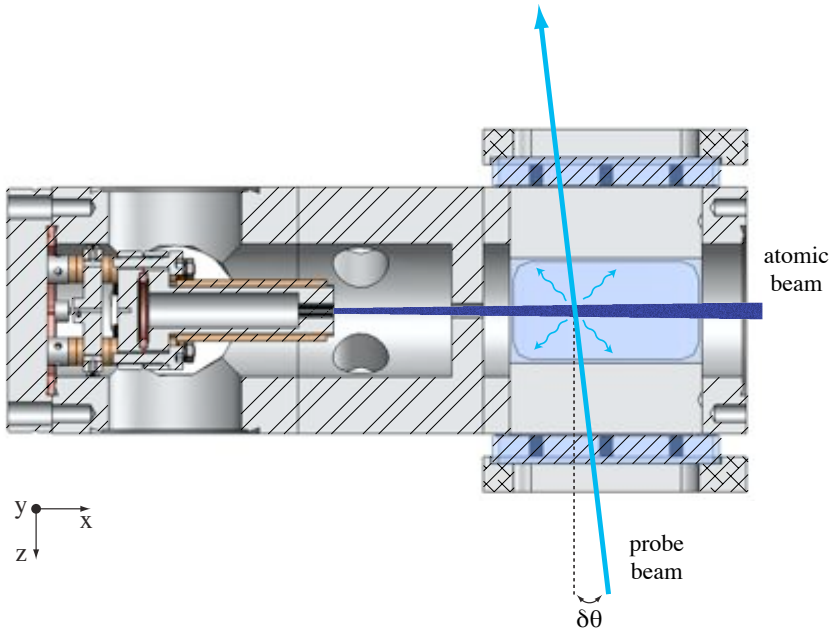

Figure 5.7: Scheme of the orthogonally-crossed-beam method spectroscopy in presence of a possible angular misalignment $\delta\theta$ between the probe beam and the perpendicular to the atomic beam. This should introduce a frequency shift in blue laser frequency stabilization.

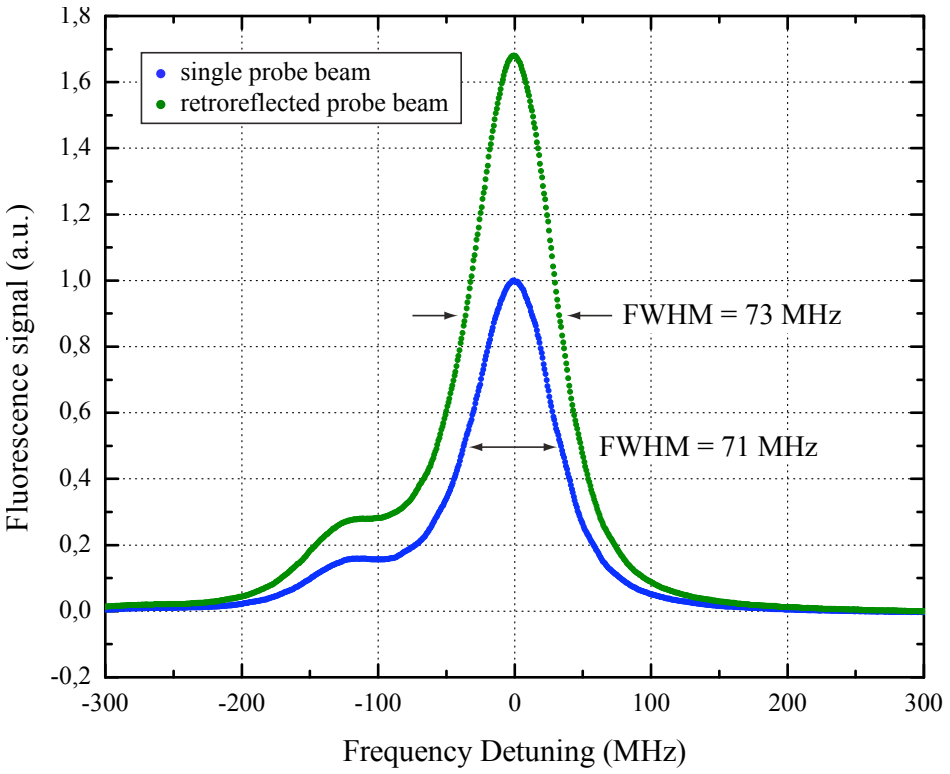

Figure 5.8: Comparison between the fluorescence signals obtained with a single (blue) and a retroreflected probe beam (green). The frequency width variation provides a shift estimate of ~ 1 MHz. The amplitude of the fluorescence signal obtained with a retroreflected probe beam is increased by a factor of 1.7.

less than the natural linewidth of 32 MHz. Experimentally this condition can be easily reached by realizing the alignment that minimizes the width of the fluorescence signal. A further proof that the shift is less than the fluorescence width is provided by retroreflecting the probe beam. In optimal alignment condition the width of the fluorescence signal is not broadened with respect to that obtained with a single beam. Fig.5.7 shows that the width difference is about 2 MHz, therefore the shift is at ~ 1 MHz level. In the configuration with retroreflected probe beam the saturation effect is negligible (see eq.5.1), therefore the fluorescence is almost doubled (with quite the same FWHM) leading to a better signal-to-noise ratio.

In normal operation we have to take into account the additional atomic fluorescence due to the Zeeman slower laser beam. Fig.5.9 shows how this affects the total fluorescence and error signal. In particular, the configuration with both probe and slowing laser beams (blue points) is compared with that obtained with probe beam alone (red points).

Significantly, the presence of the slowing beam changes the total fluorescence signal but does not perturb the error signal. This is because the slowing beam is not modulated and therefore does not contribute to the error signal production.

In this way we demonstrated that is possible to stabilize the blue laser frequency on the $^1S_0 - ^1P_1$ transition just using the atomic beam fluorescence. In optimal alignment condition frequency shift in blue laser stabilization is negligible and the Zeeman slower laser beam does not affect the error signal. This solution considerably reduces the overall system complexity since the high temperature Sr vapor cell conventionally used for blue laser stabilization is not needed here.

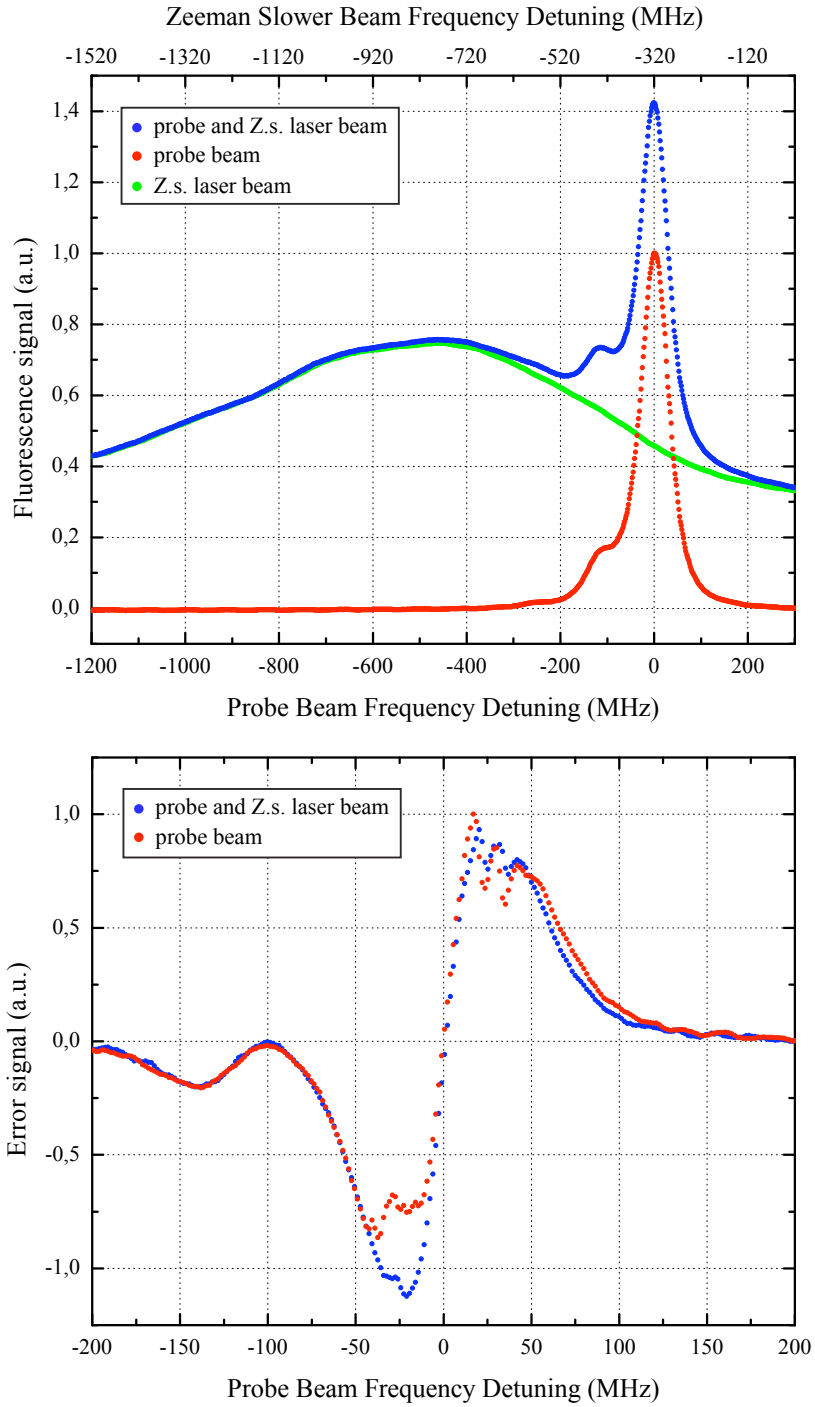

Figure 5.9: Fluorescence and error signals corresponding to the configurations with (blue points) and without the Zeeman slower laser beam (red points).

5.3 First Cooling Stage

Thermal atoms produced by the atomic oven are slowed down by the counter-propagating laser beam for Zeeman slowing and are trapped in the center of the chamber in a magneto optical trap operating on the $^1S_0 - {}^1P_1$ transition. This so called Blue MOT is realized by means of a magnetic field gradient of 50 Gauss/cm along the z-axis and three retroreflected orthogonal laser beams at 461 nm (see 2.1.3 for theoretical details). In typical operation conditions each beam has an optical power of about 3 mW, a diameter of 10 mm ($1/e^2$) and a circular polarization. The frequency red-detuning with respect to the $^1S_0 - {}^1P_1$ transition is 40 MHz. In this conditions we have observed the typical fluorescence signal of atoms trapped in the Blue MOT as it is shown in Fig.5.10. Remarkably, this represents the first realization of a ^{88}Sr Blue MOT by using a transportable setup.

The fluorescence signal is detected by a calibrated photomultiplier in order to estimate the number of trapped atoms. Additionally by changing the blue laser frequency it is possible to separately trap three different strontium isotopes, as shown in Fig.5.10. For the most abundant ^{88}Sr isotope a number of about 1.0×10^8 trapped atoms is estimated.

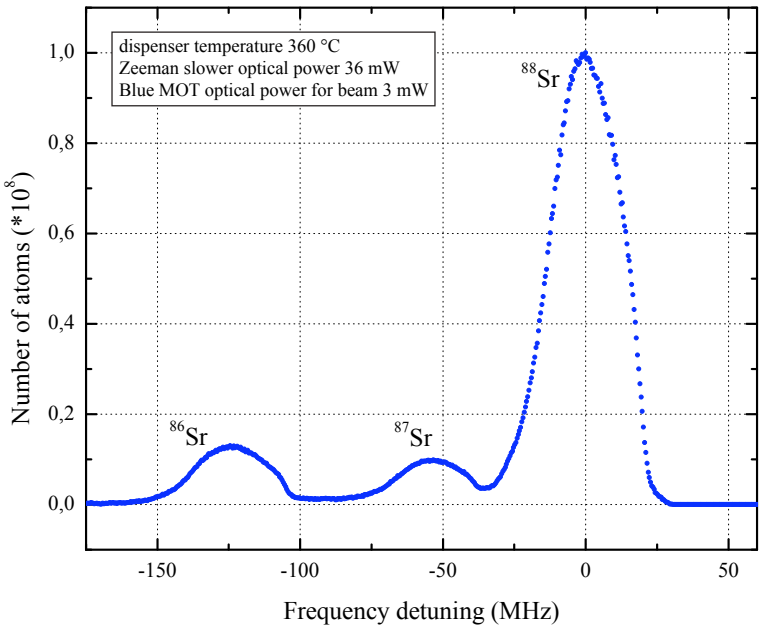

Figure 5.10: Fluorescence signal produced by atoms trapped into the Blue MOT as a function of blue laser detuning. Three peaks corresponding to ^{88}Sr, ^{87}Sr and ^{86}Sr isotope are visible.

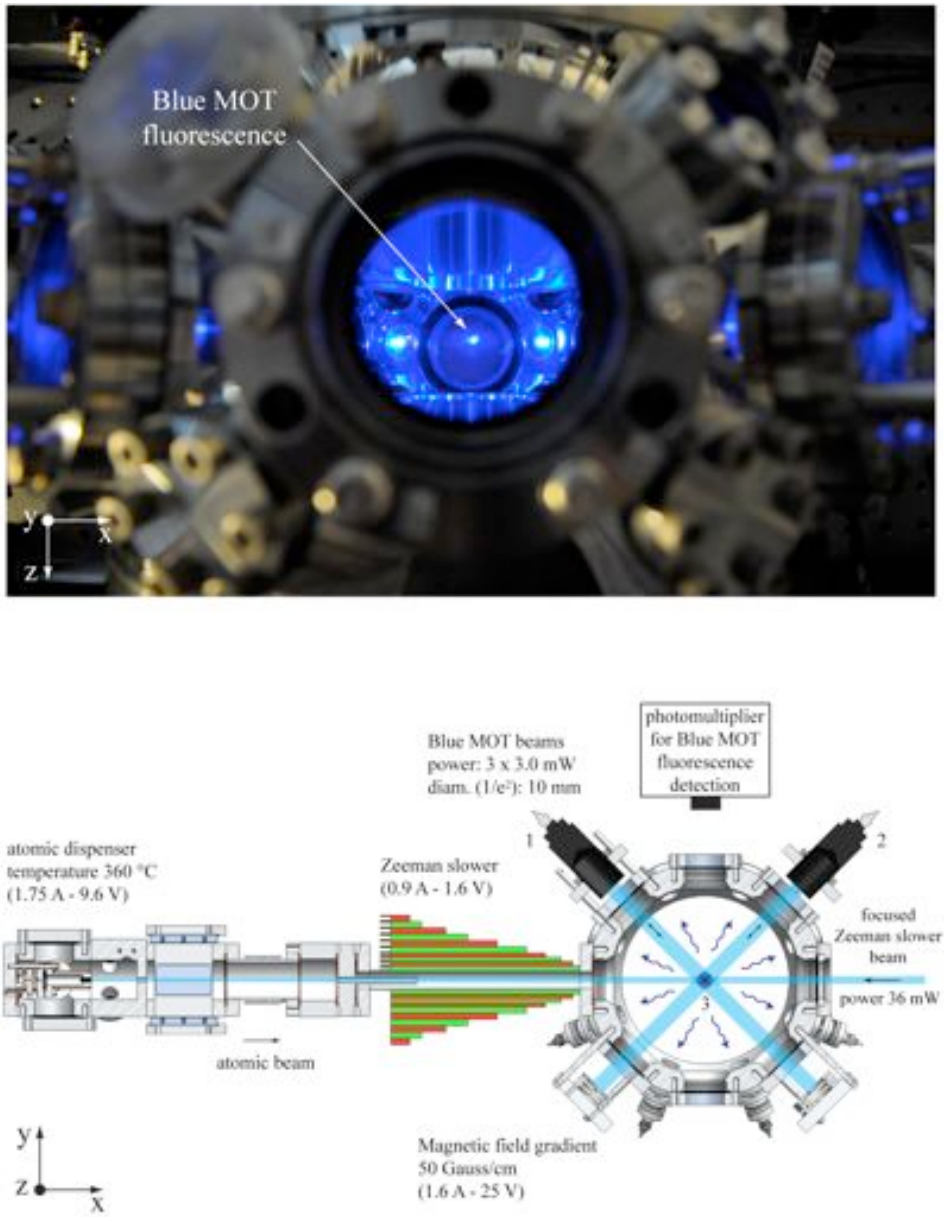

Figure 5.11: Picture of the atomic fluorescence produced by atoms trapped in the Blue MOT and a schematic view of the system for Blue MOT production. The fluorescence signal is observed from one of the CF40 viewports of the chamber and it is detected by a calibrated photomultiplier for Blue MOT characterization.

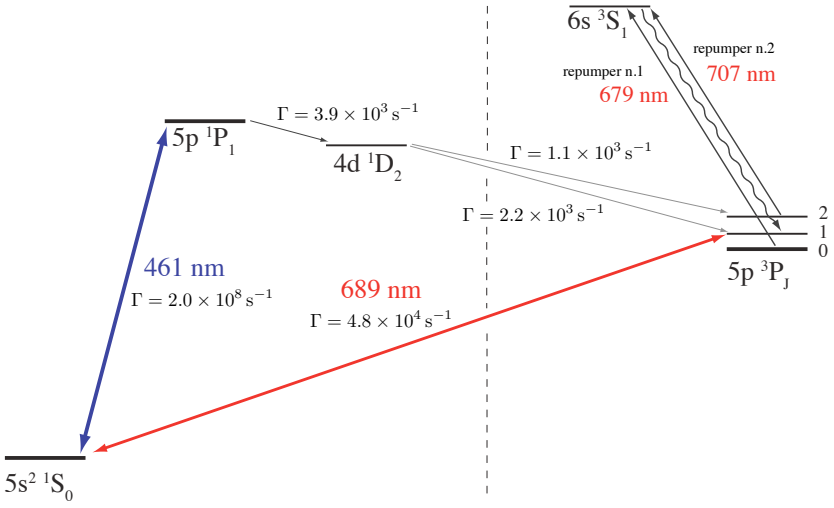

Figure 5.12: Partial electronic level structure of atomic strontium. The $^1S_0 - {}^1P_1$ transition is not perfectly closed and a certain fraction of atoms are optically pumped into the metastable $5p\,{}^3P_2$ state and lost. A possible repumping scheme with two lasers at 679 nm and 707 nm is also shown.

A further characterization of Blue MOT loading and switching-off dynamics has been realized. The $^1S_0 - {}^1P_1$ transition used for Blue MOT is not perfectly closed due to the decay channel of the $5p\,{}^1P_1$ towards the $4d\,{}^1D_2$ state. Atoms in the latter state may decay to the ground state through the $5p\,{}^3P_1$ within less than 1 ms, or may decay to the metastable $5p\,{}^3P_2$ and be lost (see Fig.5.12).

Therefore the number of atoms trapped in the Blue MOT (N) can be described by the equation

$$\frac{dN}{dt} = \phi_e - \Gamma_L N$$

where ϕ_e is the effective flux of atoms that can be trapped and Γ_L is the number of atoms lost per second due to optical pumping in the metastable $5p\,{}^3P_2$ state [101]. The previous equation with the initial condition $N(t = 0) = 0$ has the solution

$$N(t) = N_{st}(1 - e^{-t/\tau})\,,$$

where $N_{st} = \phi_e/\Gamma_L$ is the stationary number of trapped atoms and $\tau = 1/\Gamma_L$ is the loading time of the Blue MOT (or equivalently the decay time). The value of τ has been experimentally estimated by measuring both the Blue MOT loading time τ_{on} and decay time τ_{off} (see Fig.5.13). The resulting

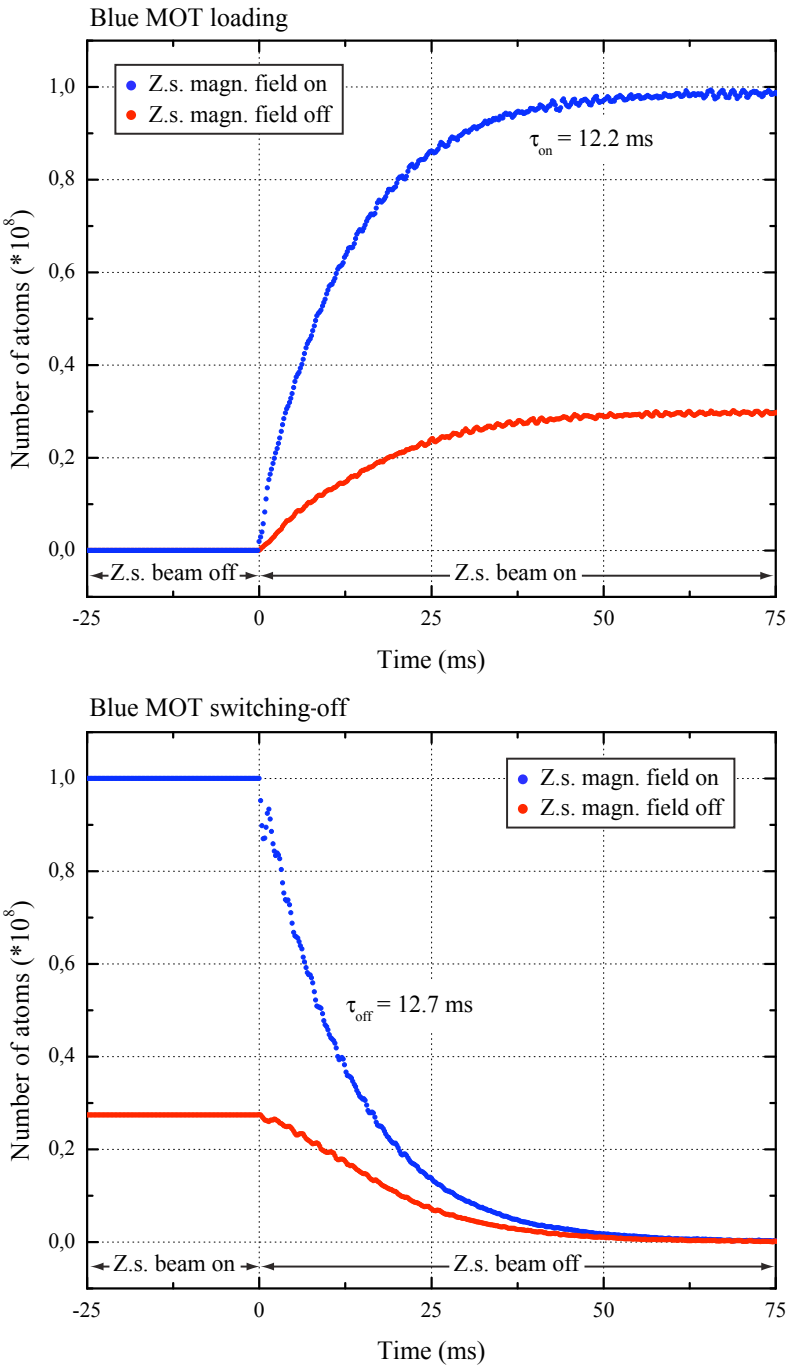

Figure 5.13: Blue MOT loading and switching-off dynamics. Loading (switching-off) is realized by turning on (off) the optical beam for zeeman slowing. The contribution of the Zeeman slower is also outlined by measuring the number of trapped atoms with (blue points) and without (red points) magnetic field for Zeeman slowing.

values are quite comparable and provide a time constant $\tau \sim 12.5\,\mathrm{ms}$. From the independent measurement $N_{st} = 1 \times 10^8$ performed by detecting the Blue MOT fluorescence we also obtain an estimate for the effective flux of atoms $\phi_e = N_{st}/\tau \sim 8.0 \times 10^9\,\mathrm{atom/s}$. Considering that the atomic flux produced by dispenser at $T = 360\,^{\circ}\mathrm{C}$ is about $3 \cdot 10^{11}\,\mathrm{atoms/s}$, results that about 3 % of these atoms are effectively trapped into the Blue MOT. This value can be significantly improved by fine tuning the frequency of the Zeeman slower beam and by optimizing the alignment of the atomic beam across the differential tube. Nevertheless in this configuration, as it is shown in Fig.5.13, the number of trapped atoms is increased by a factor of 3 by the presence of the magnetic field for Zeeman slowing. In normal operation conditions atoms trapped in the Blue MOT are cooled down to a final temperature at the mK level.

5.4 Second Cooling Stage

The cold atomic sample produced by Blue MOT is then loaded on a MOT operating on the $^1\mathrm{S}_0 - {}^3\mathrm{P}_1$ transition (Red MOT). Remarkably the latter operates on an intercombination line (linewidth $\gamma = 7.6\,\mathrm{kHz}$, see Fig.3.1) which corresponds to a Doppler temperature $T_\mathrm{D} = 180\,\mathrm{nK}$ (eq.2.18) which is less than the ultimate laser cooling limit set by half the photon recoil temperature $T_\mathrm{r}/2 = 230\,\mathrm{nK}$ (eq.2.20) [60]. The dynamics of laser cooling on this narrow transition presents several peculiar features which are well described in [70, 71, 72, 73]. Experimentally the Red MOT has been realized by employing an external laser at 689 nm with 20 Hz linewidth which delivers about 6 mW on the atoms. Laser beams for Blue and Red MOT are perfectly superimposed by means of the dichroic fiber cluster (already presented in 4.8). To have an efficient loading process from Blue to Red MOT it is necessary to spread the spectrum of the laser at 689 nm in order to cover the Doppler broadening $\Delta\nu_D(T = 1\,\mathrm{mK}) \simeq 1.6\,\mathrm{MHz}$ corresponding to the velocity distribution of atoms trapped in the Blue MOT. This is realized by sending the 689 nm radiation through an AOM in a double pass configuration. The radio frequency ($\sim 80\,\mathrm{MHz}$) driving the AOM is modulated at 25 kHz, with a span of 400 kHz (see Fig.5.14). Optically this results in a frequency broadening of 800 kHz, corresponding to 32 sidebands, each one with an optical intensity of $240\,\mu\mathrm{W/cm^2}$ (the saturation intensity is $I_s = 3\,\mu\mathrm{W/cm^2}$). The central frequency is red detuned by 400 kHz with respect the $^1\mathrm{S}_0 - {}^3\mathrm{P}_1$ transition. This so called “broadband phase" occurs for

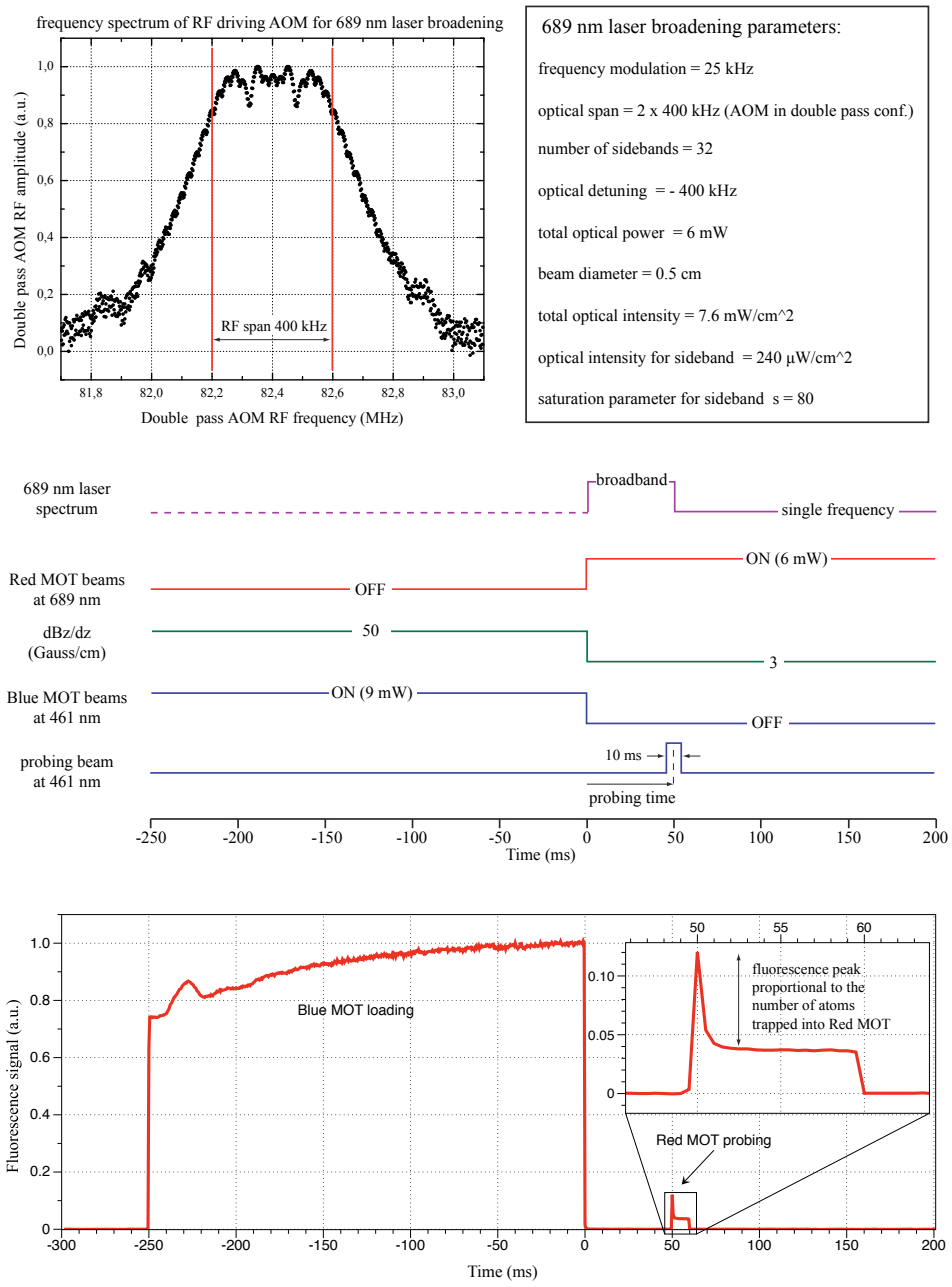

Figure 5.14: Schematic view summarizing the relevant parameters for broadening phase, the timing for Blue to Red MOT loading and the corresponding fluorescence signal used to measure the number of atoms trapped into the Red MOT.

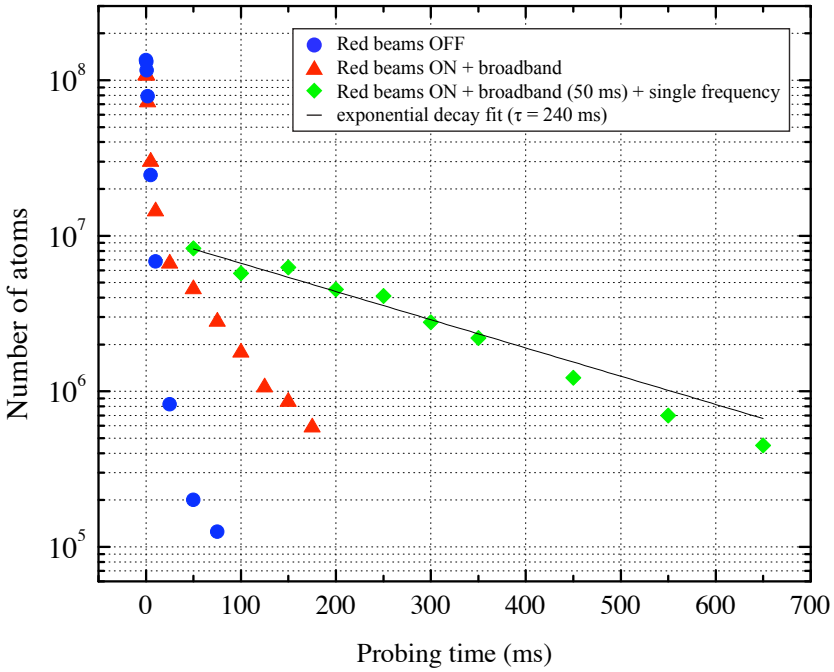

Figure 5.15: Number of atoms trapped into the Red MOT as a function of time. The origin $t = 0$ corresponds to Red MOT loading.

the first 50 ms and is then followed by the proper "single frequency phase" (see Fig.5.14) where the atomic sample is cooled down to the μK level. The number of atoms trapped into the Red MOT is estimated by probing the atomic sample with a resonant laser beam at 461 nm and by detecting the fluorescence signal with a calibrated photomultiplier. Starting from the origin $t = 0$ (timing diagram in Fig.5.14) corresponding to Red MOT loading we measure the number of trapped atoms as a function of the probing time (see Fig.5.15). This is done for three different experimental conditions. Red triangles represent the Red MOT population obtained with a continuos broadband phase. Green rhombuses represents the same population attained with a limited broadband phase (early 50 ms) followed by the proper single frequency phase. From the comparison with the number of atoms measured after Blue MOT switching-off (blue circles) Fig.5.15 shows how this number is increased by the presence of red beams with about 10^7 atoms loaded into the Red MOT. The configuration with single frequency phase allowed us to trap atoms for several hundreds of milliseconds. By performing an exponential fit of the atom population decay we estimate a Red MOT life time of about 240 ms.

Chapter 6

Conclusions and perspectives

The aim of this thesis was to build and experimentally demonstrate the possibility of a transportable optical clock based on strontium atoms. We described the realization of a compact system for ultra-cold strontium production that represents the core of an optical lattice clock. Several novel solutions have been developed to reduce volume, mass and power consumption in comparison with a standard stationary system. The transportable system here presented has been designed matching together the requirements of compact dimension, hardware modularity and operation reliability. We showed the design and the realization of each subsystem and the final integration. In particular we developed a compact vacuum system with solutions to optimize the laser cooling of strontium atoms. We realized a new high efficiency atomic oven providing a highly collimated atomic beam. We used only semiconductor laser sources and we developed a new compact breadboard for the preparation (detunings and optical power distribution) of the laser beams needed for cooling and trapping. Finally we used a novel dichroic fiber cluster to couple into the same fibers both the light needed for the first and second cooling stage, at 461 nm and 689 nm respectively. In this way we realized a system in which all the needed lights for cooling, trapping and clock spectroscopy are delivered to the vacuum system by means of optical fibers.

Preliminary results of the ongoing system characterization were also presented. In particular we performed a characterization of the atomic oven in terms of thermal properties and atomic beam divergence. We produced an atomic beam flux of $\sim 10^{11}$ atoms/s with a power consumption of only 17 W (dispenser temperature $\sim 360\,^{\circ}$C). We measured an atomic beam di-

vergence of only 60 mrad. High atomic beam collimation allowed us to use a orthogonally-crossed-beam spectroscopy scheme to frequency stabilize the laser source at 461 nm on the $^1S_0 - {}^1P_1$ transition. In this way we significantly reduced the system complexity since an additional high temperature strontium vapor cell for laser frequency stabilization was not needed. We performed the first cooling stage and we observed about 10^8 atoms trapped into the Blue MOT (without repumpers). We characterized the Blue MOT loading and switching-off dynamics. A compact Zeeman slower allowed us to increase the number of trapped atoms by a factor of 3. We performed a preliminary test of the second cooling stage and we trapped about 10^7 atoms into the Red MOT.

The next step will be the integration of this system with a transportable clock-laser system at 698 nm to realize a fully transportable strontium optical lattice clock. In this way we will realize a powerful tool for a wide range of applications. The transportable system will be used as an “optical clock tester" to be moved to other stationary optical clocks placed in metrological laboratories spread around the world. In this way it will be possible to verify the effective reproducibility of different optical frequency references and to provide important informations toward the future redefinition of the SI second, based on optical standards. Additionally such transportable clock should also be used to preliminary demonstrate a new kind of relativity-based-geodesy, by measuring how the local mass distribution and variation affects the clock time measurement.

Furthermore, the experimental work done in this thesis can provide important technological and scientific informations toward the realization of a new-generation of transportable optical clocks more robust and reliable for applications on Earth and in Space.

Appendix A

Technical Drawings

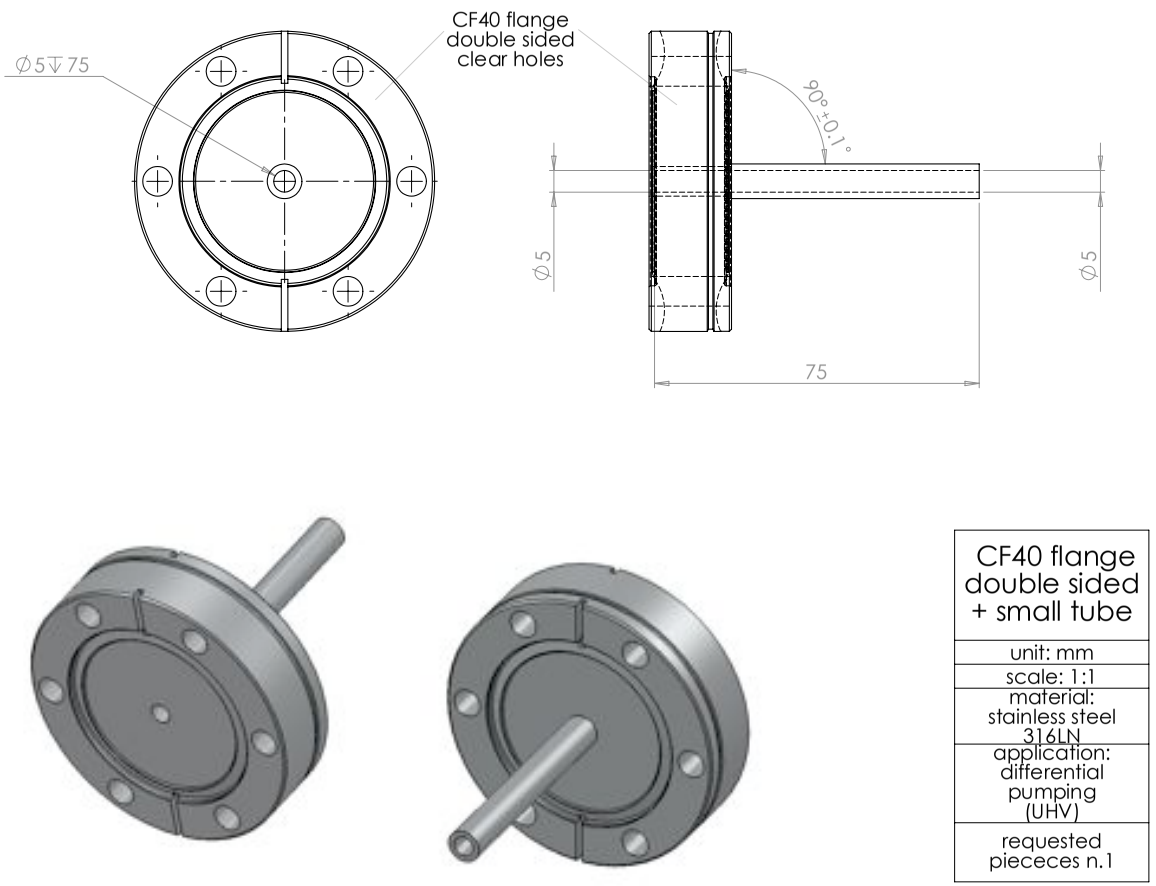

Figure A.1: Double sided CF40 flange with tube for differential pumping.

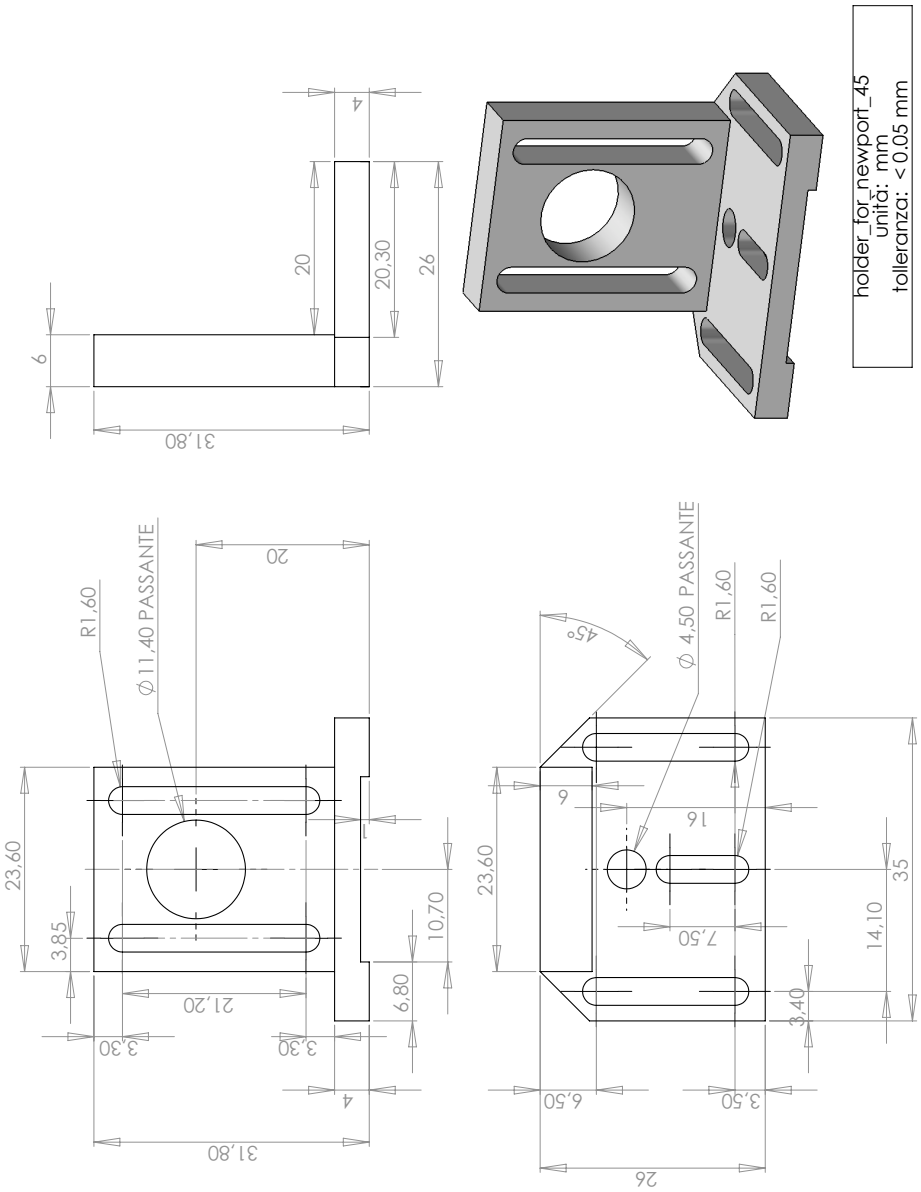

Figure A.2: Custom holder for 45° mirror.

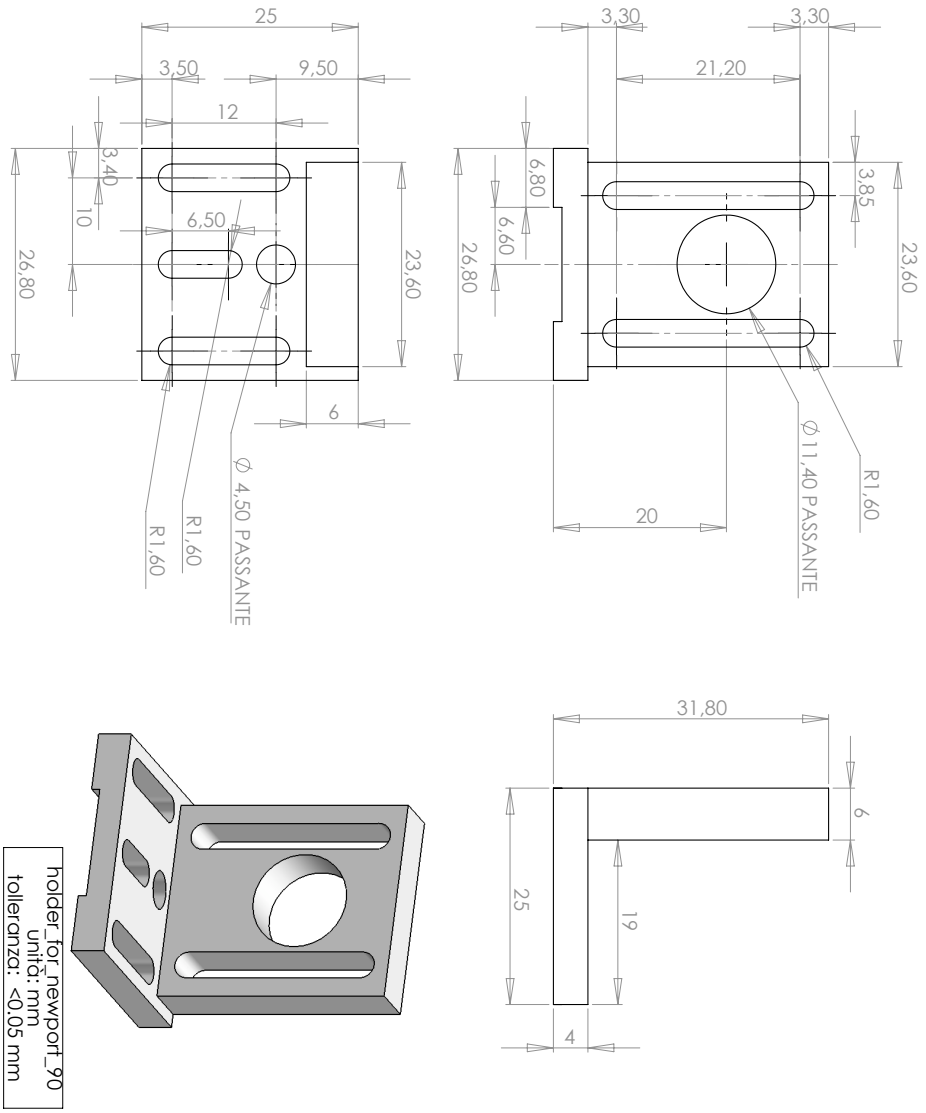

Figure A.3: Custom holder for 90° mirror.

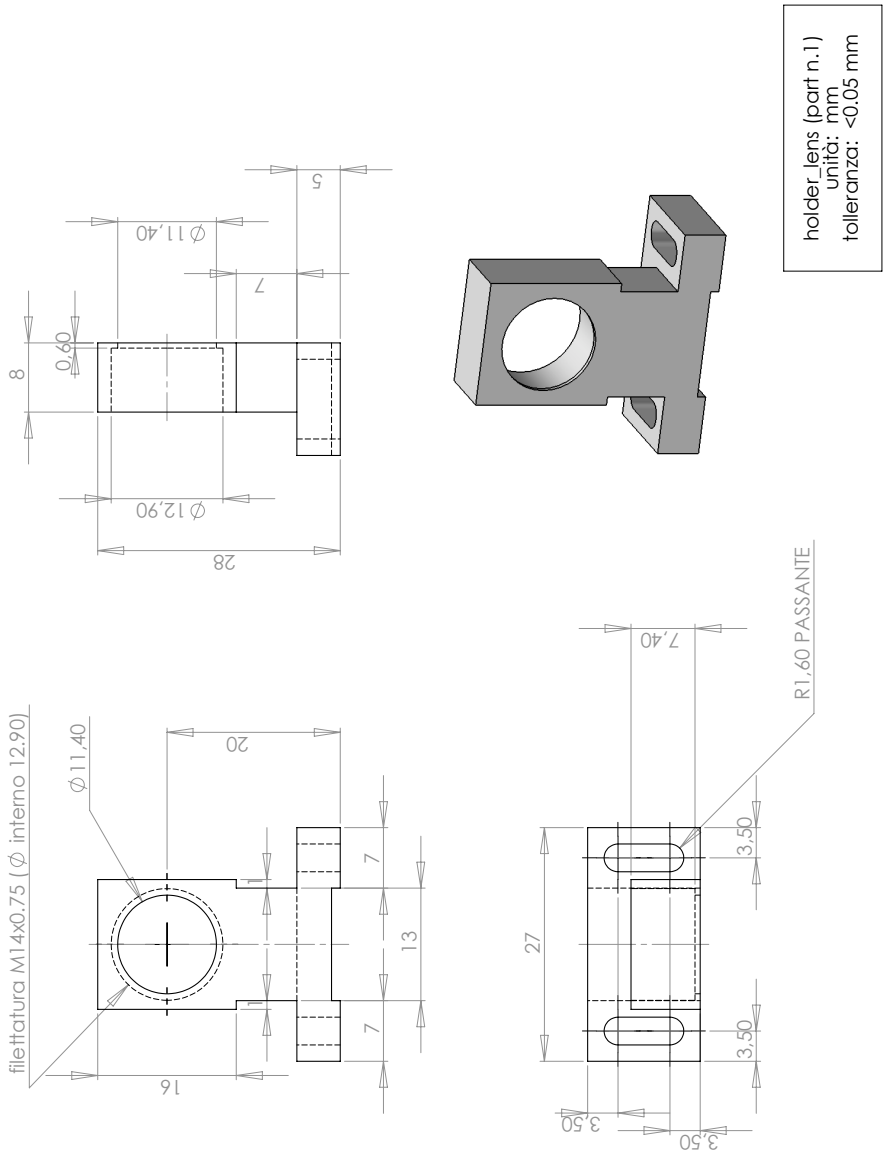

Figure A.4: Custom holder for lens.

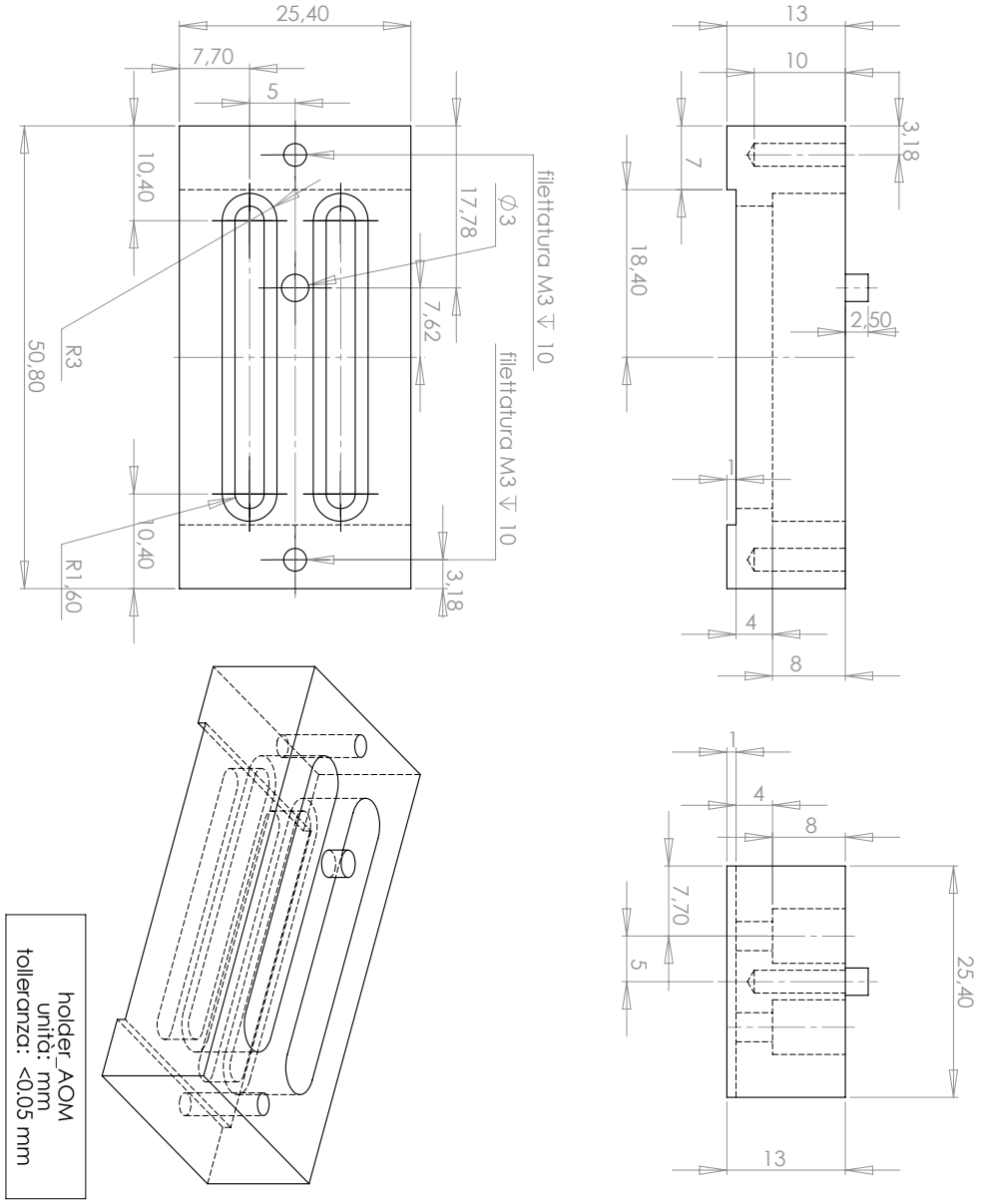

Figure A.5: Custom holder for AOM.

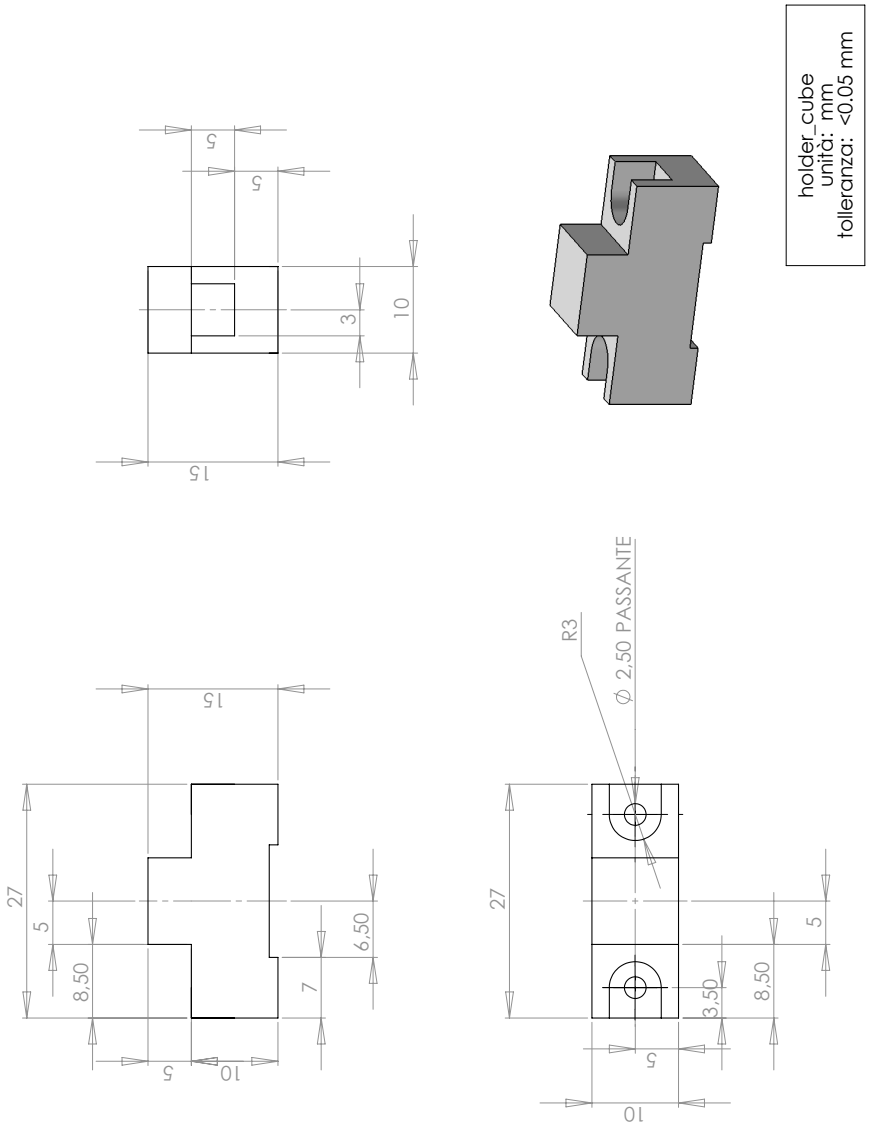

Figure A.6: Custom holder for polarization cube.

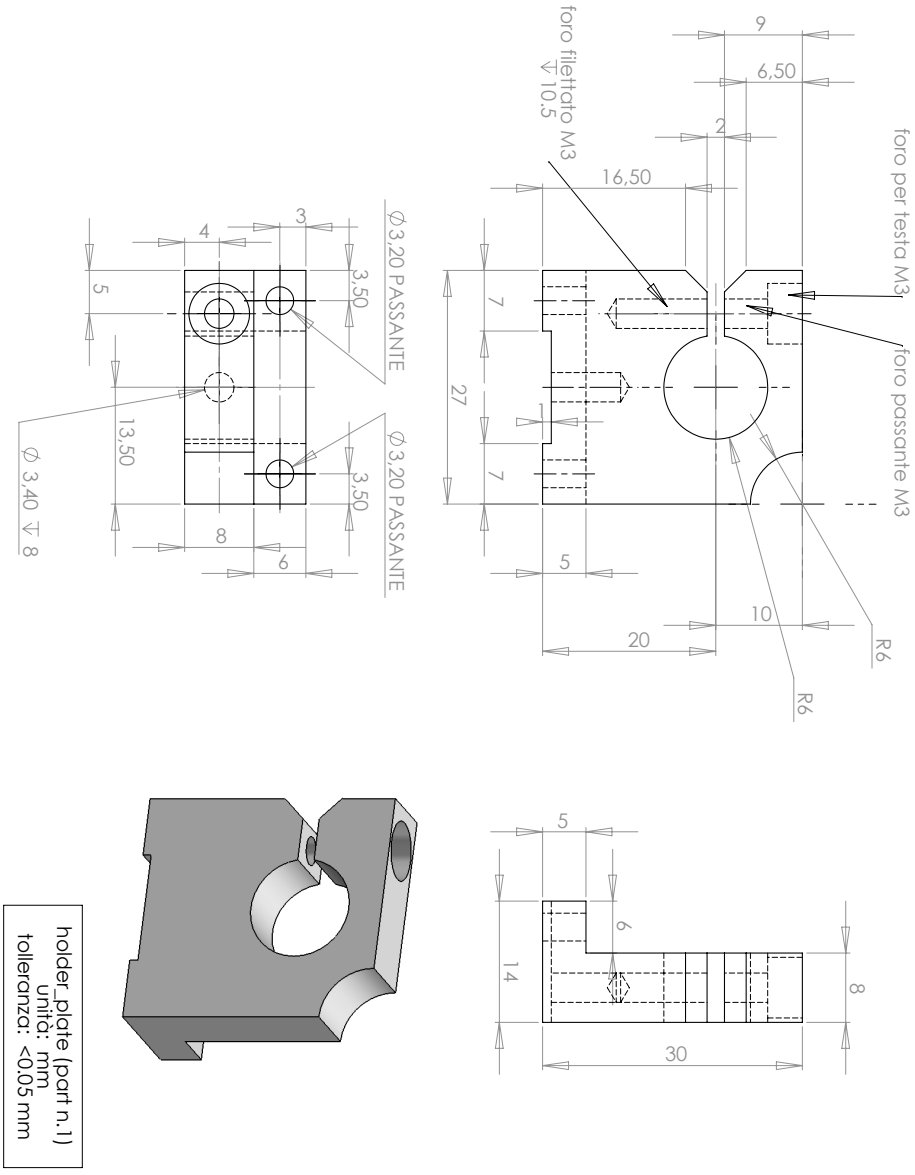

Figure A.7: Custom holder for polarization plate, part 1/2.

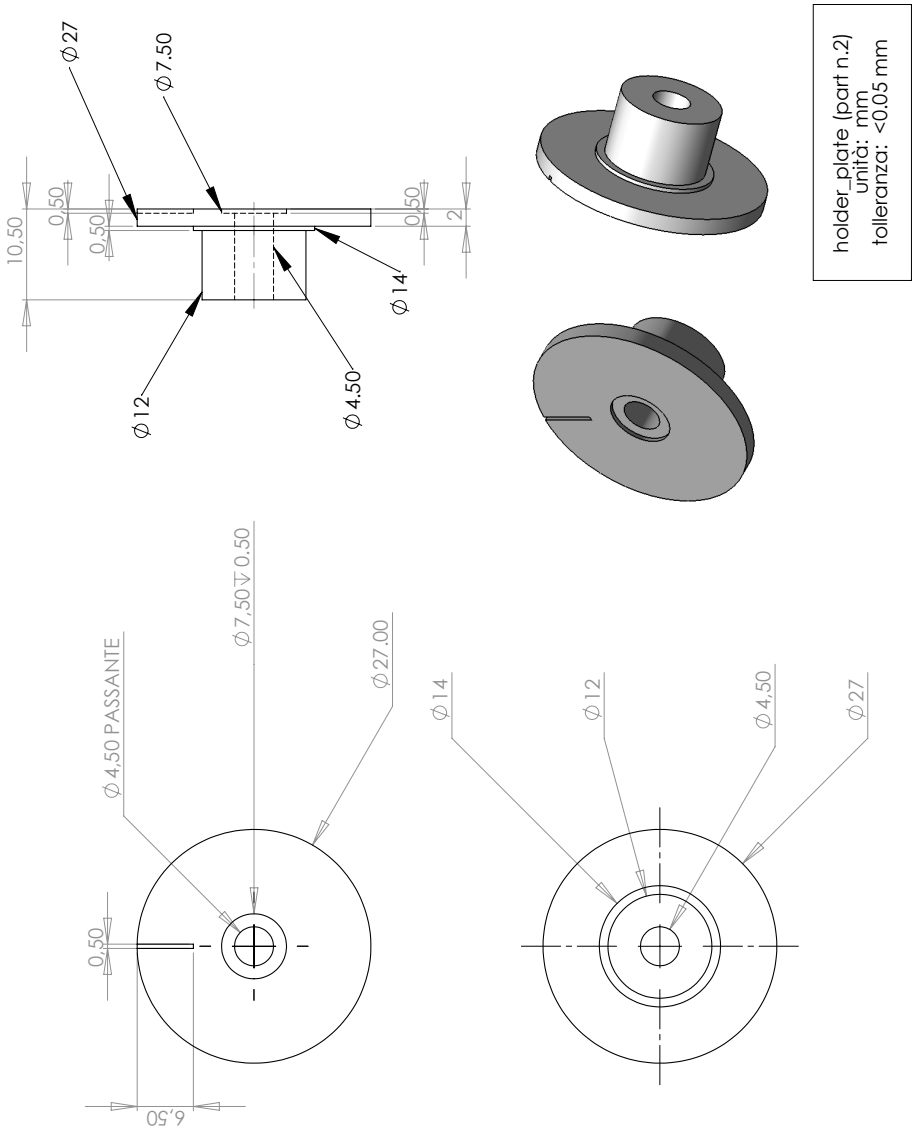

Figure A.8: Custom holder for polarization plate, part 2/2.

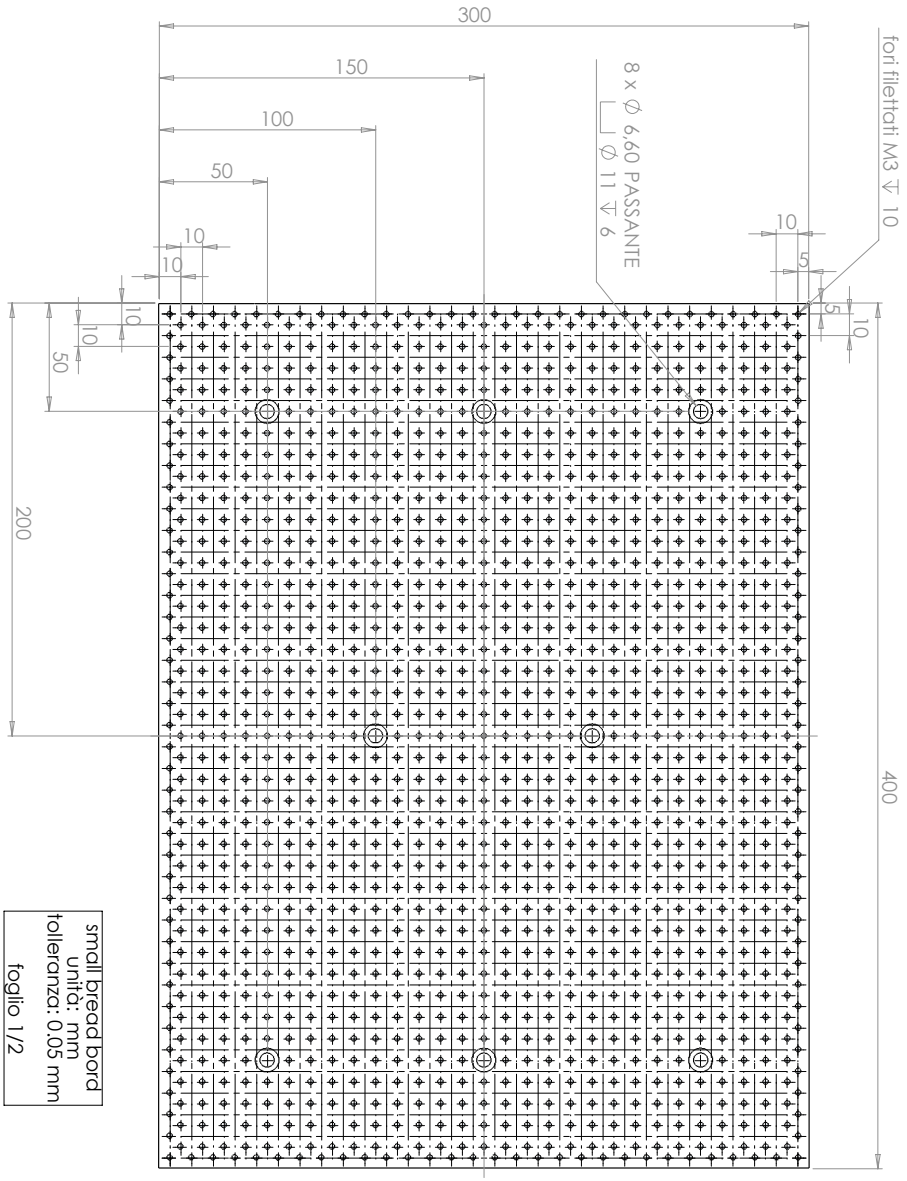

Figure A.9: Compact optical breadboard for laser cooling beams preparation, part 1/2.

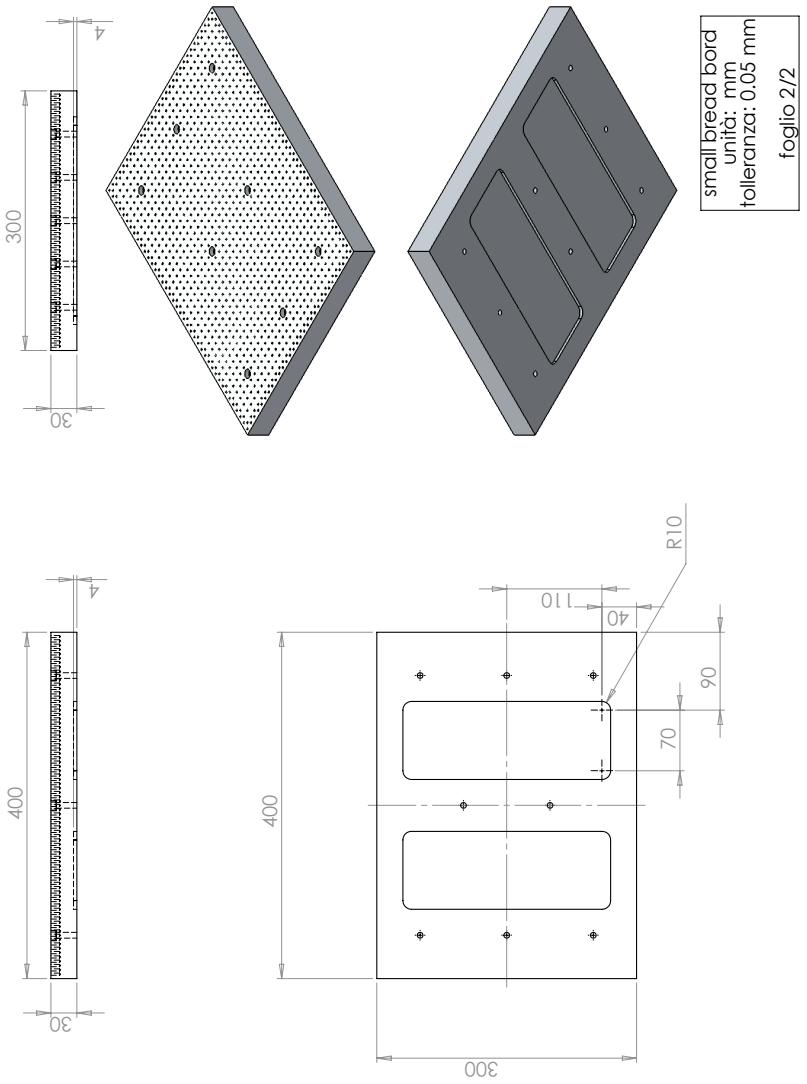

Figure A.10: Compact optical breadboard for laser cooling beams preparation, part 2/2.

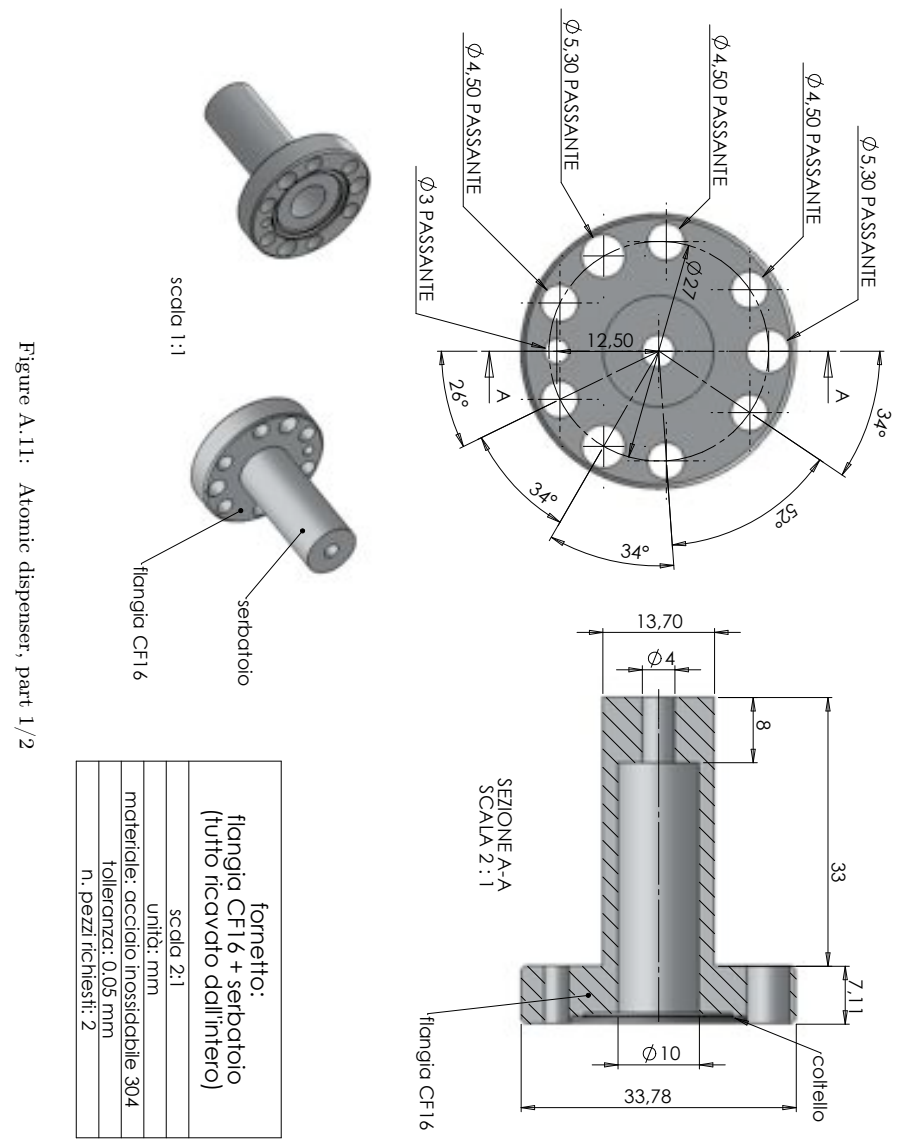

Figure A.11: Atomic dispenser, part 1/2

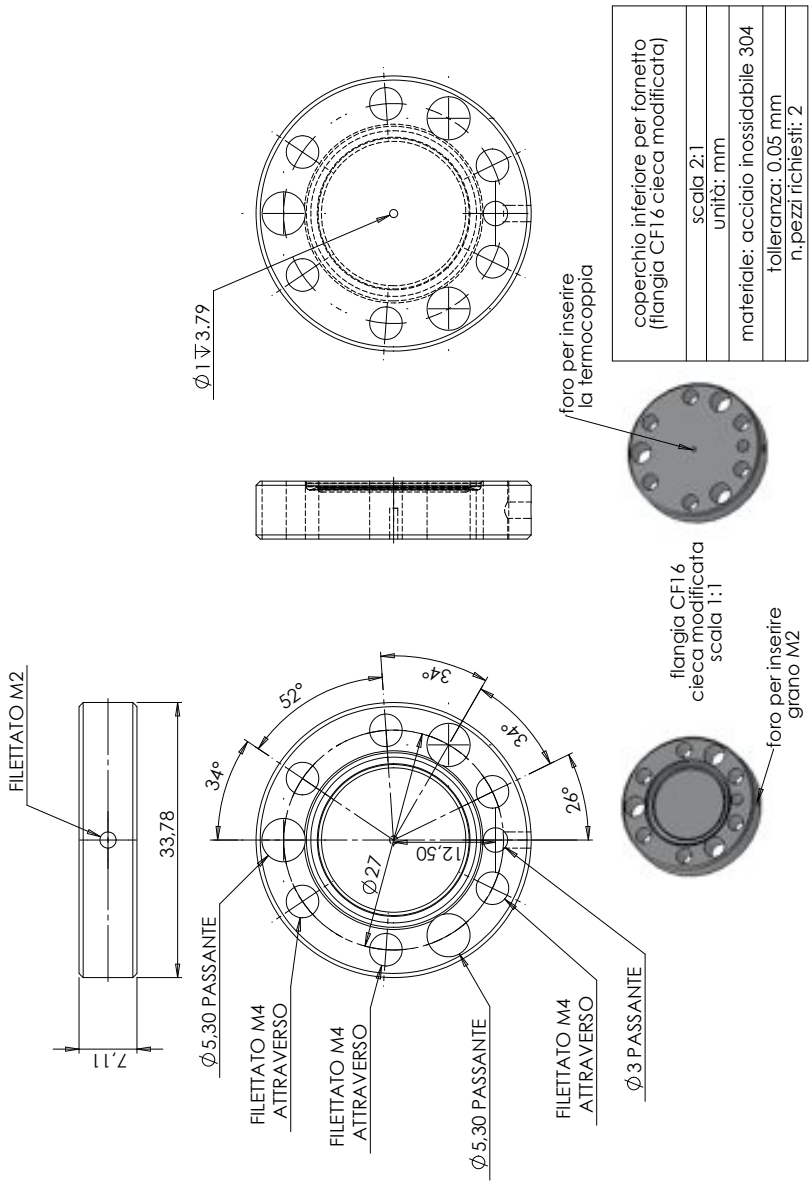

Figure A.12: Atomic dispenser, part 2/2

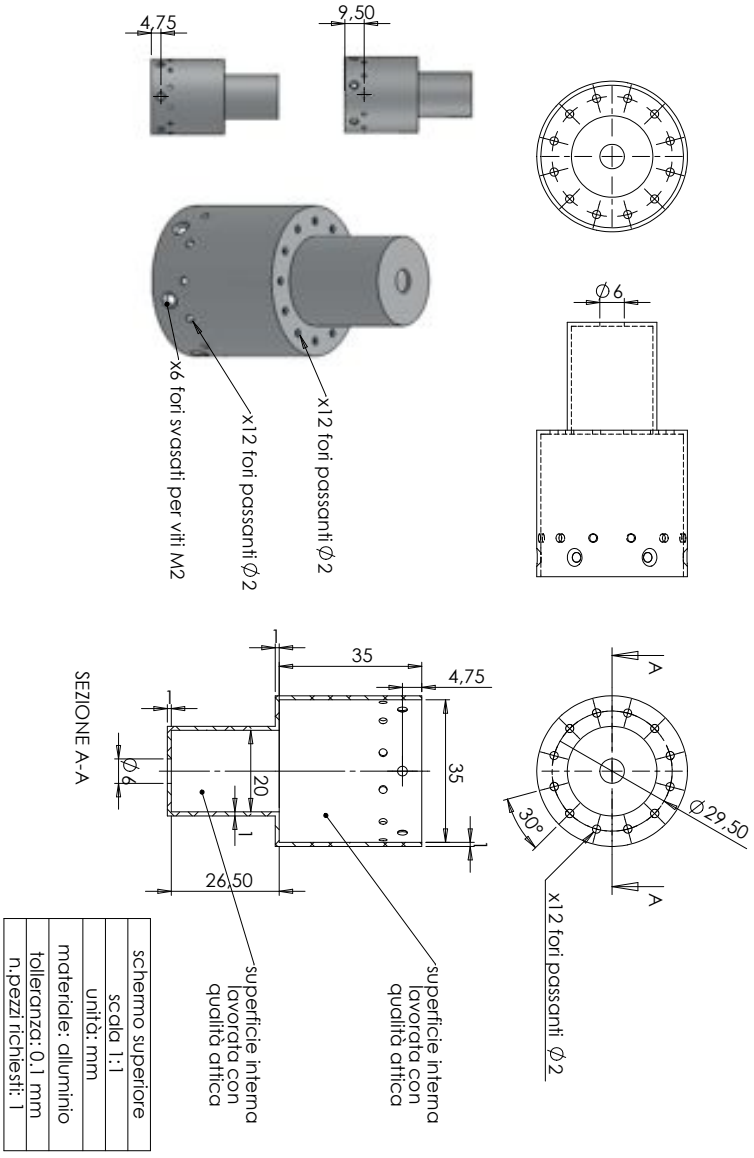

Figure A.13: Thermal shield for atomic dispenser, part 1/2

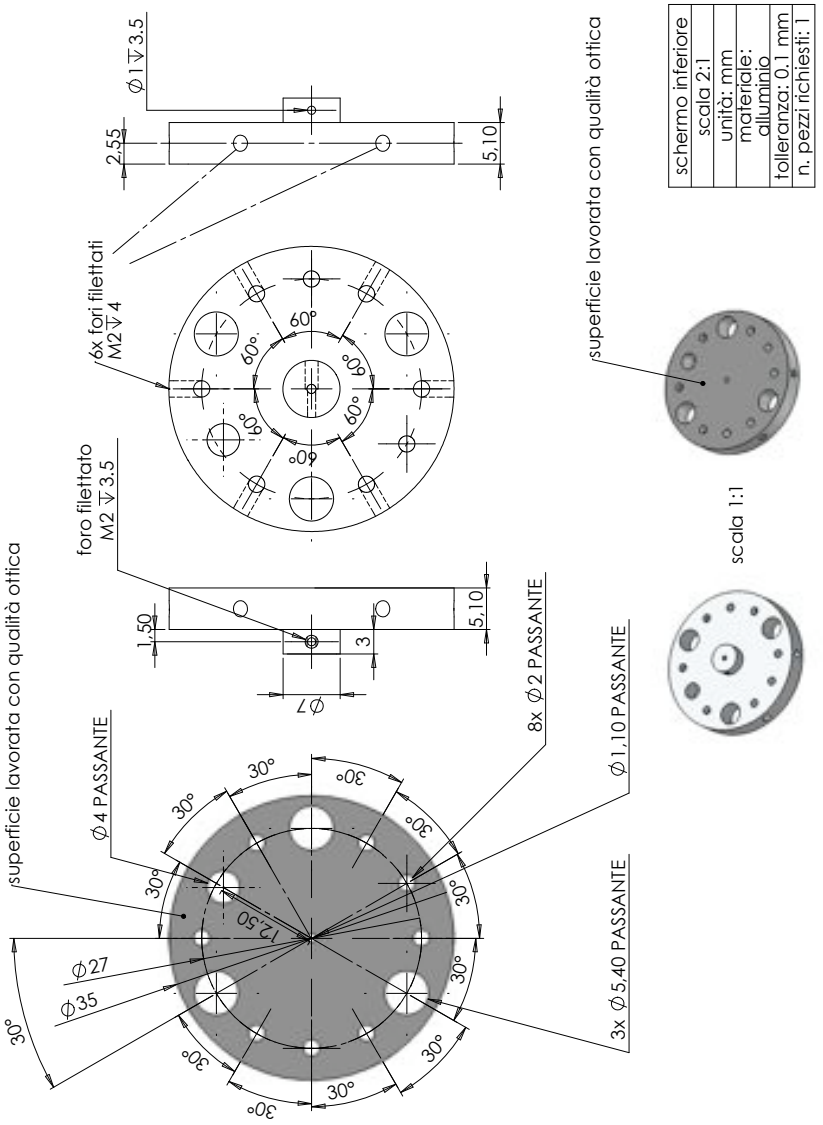

Figure A.14: Thermal shield for atomic dispenser, part 2/2

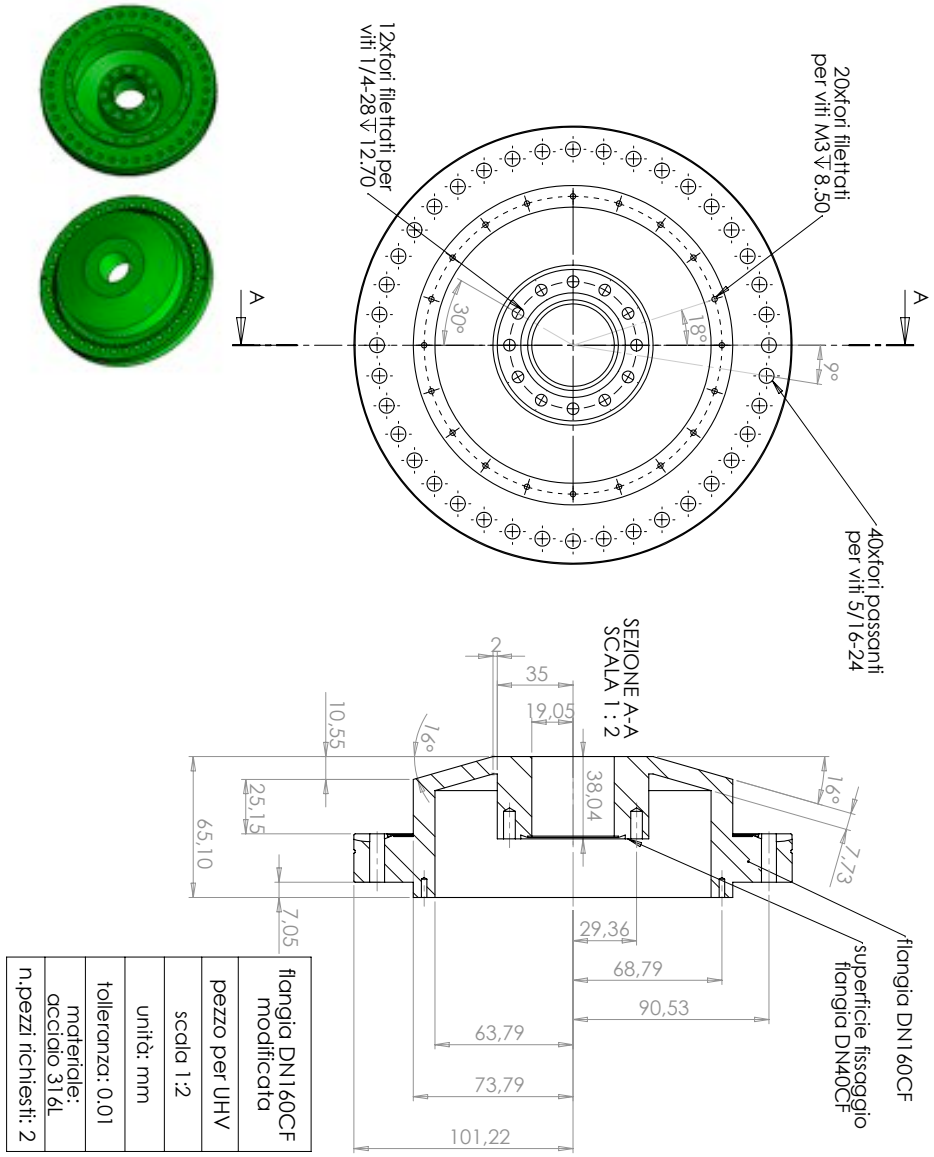

Figure A.15: Custom CF150 flange.

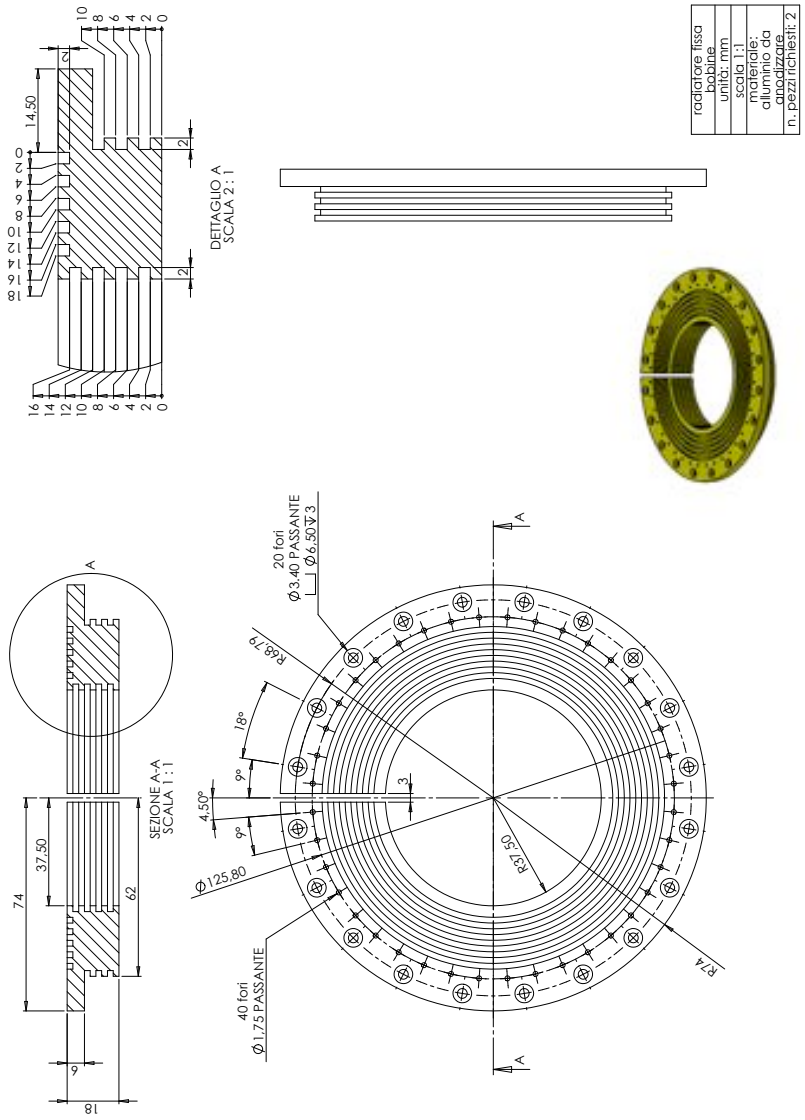

Figure A.16: Passive heat sink for MOT coils .

schematico bobine
unità: mm
scala 1:2
tolleranza 0.5 mm
diametro filo: 1mm
materiale: rame
n.pezzi riciesti 2

Figure A.17: MOT coil.

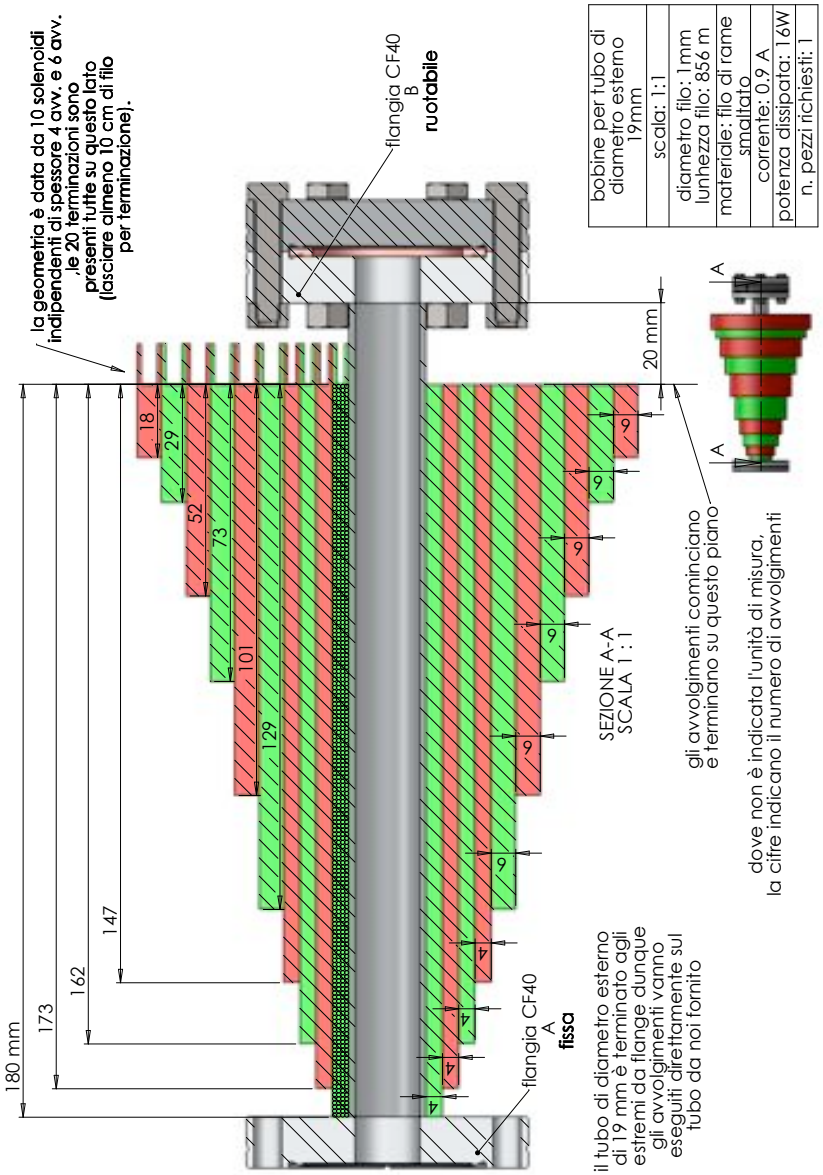

Figure A.18: Zeeman slower.

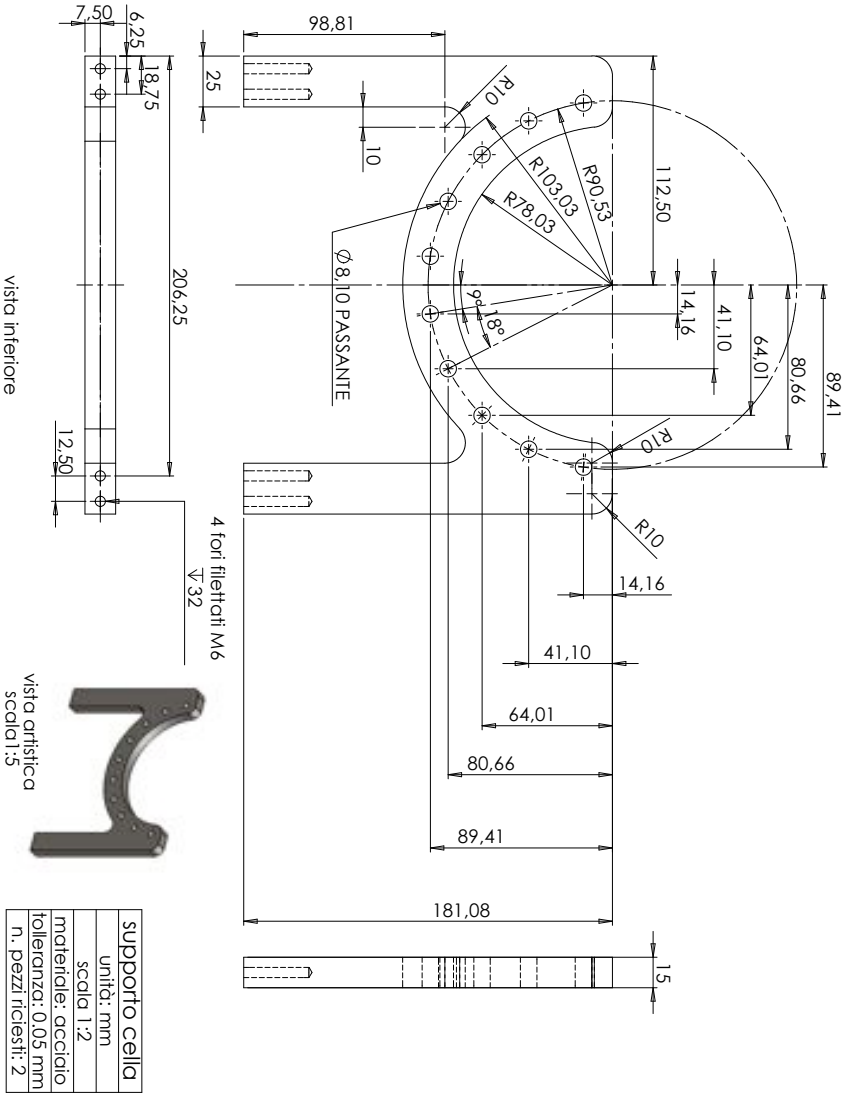

Figure A.19: Holder for MOT chamber.

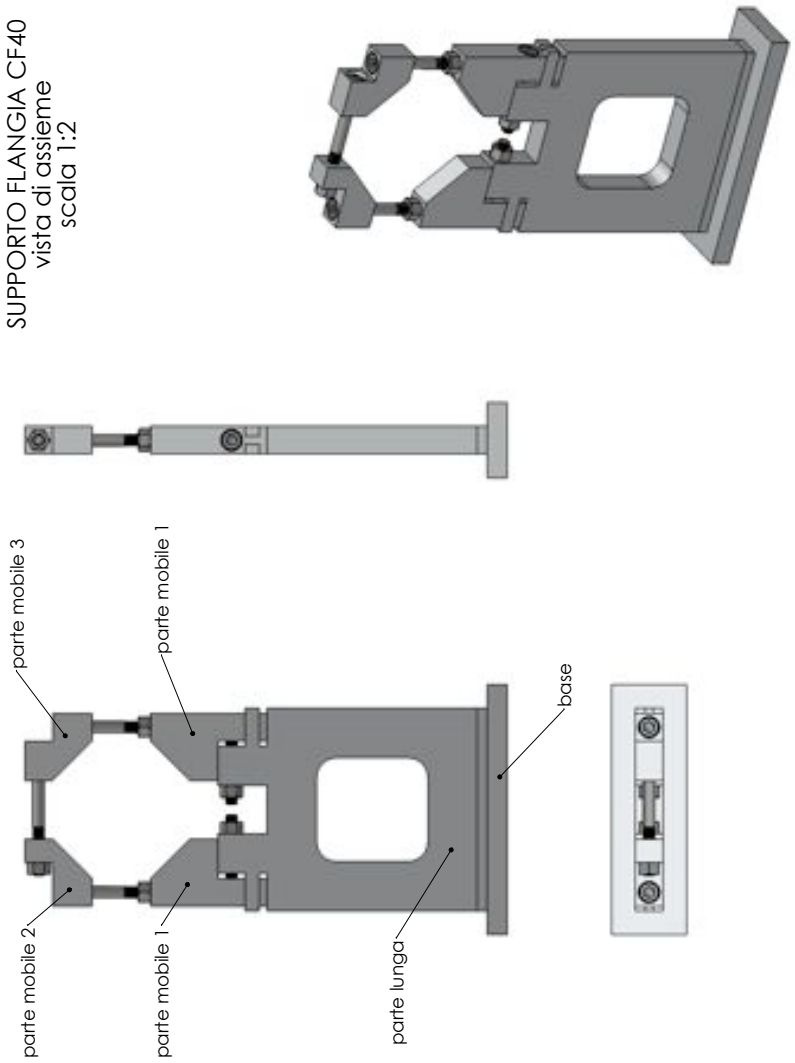

Figure A.20: Adjustable holder for CF40 flange.

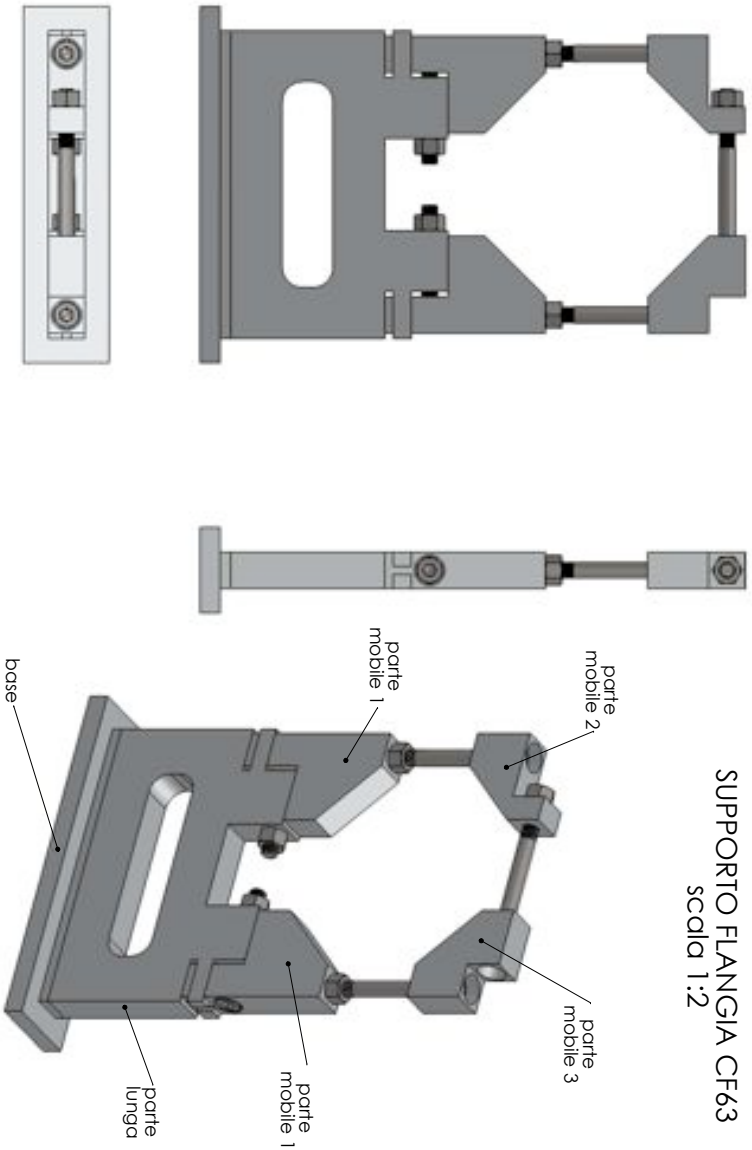

Figure A.21: Adjustable holder for CF63 flange.

List of Figures

List of Tables

Bibliography

[1] J. Jespersen and J. Fitz-Randolph, *From Sundials to Atomic Clocks*, Dover Pubblications, New York, 1999.

[2] D. Allan, *Statistics of atomic frequency standards*, Proceedings of the IEEE **54**, 221– 230 (2005).

[3] W. M. Itano, J. C. Bergquist, J. J. Bollinger, J. M. Gilligan, D. J. Heinzen, F. L. Moore, M. G. Raizen, and D. J. Wineland, *Quantum projection noise: Population fluctuations in two-level systems*, Phys. Rev. A **47**, 3554 (1993).

[4] L. Hollberg, C. W. Oates, E. A. Curtis, E. N. Ivanov, S. A. Diddams, T. Udem, H. G. Robinson, J. C. Bergquist, R. J. Rafac, W. M. Itano, R. E. Drullinger, and D. J. Wineland, *Optical frequency standards and measurements*, IEEE Journal of Quantum Electronics **37**, 1502 (2001).

[5] S. A. Diddams, J. C. Bergquist, S. R. Jefferts, and C. W. Oates, *Standards of time and frequency at the outset of the 21st century*, Science **306**, 1318 (2004).

[6] *The International System of Units (SI) (Bureau International des Poids et Mesure).*

[7] *http://tf.nist.gov/general/pdf/2039.pdf.*

[8] T. P. Heavner, S. R. Jefferts, E. A. Donley, J. H. Shirley, and T. E. Parker, *NIST-F1: recent improvements and accuracy evaluations*, Metrologia **42**, 411 (2005).

[9] S. Bize, P. Laurent, M. Abgrall, H. Marion, I. Maksimovic, L. Cacciapuoti, J. Grünert, C. Vian, F. Santos, P. Rosenbusch, P. Lemonde, G. Santarelli, P. Wolf, A. Clairon,

A. Luiten, M. Tobar, and C. Salomon, *Cold atom clocks and applications*, Journal of Physics B: Atomic, Molecular and Optical Physics **38**, S449 (2005).

[10] F. Levi, D. Calonico, L. Lorini, and A. Godone, *IEN-CsF1 primary frequency standard at INRIM: accuracy evaluation and TAI calibrations*, Metrologia **43**, 545 (2006).

[11] A. L. Schawlow and C. H. Townes, *Infrared and optical masers*, Physical Review **112**, 1940 (1958).

[12] S. Chu, *Nobel lecture: The manipulation of neutral particles*, Reviews of Modern Physics **70**, 685 (1998).

[13] C. N. Cohen-Tannoudji, *Nobel lecture: Manipulating atoms with photons*, Reviews of Modern Physics **70**, 707 (1998).

[14] W. D. Phillips, *Nobel lecture: Laser cooling and trapping of neutral atoms*, Reviews of Modern Physics **70**, 721 (1998).

[15] L. Hollberg, S. Diddams, A. Bartels, T. Fortier, and K. Kim, *The measurement of optical frequencies*, Metrologia **42**, 105 (2005).

[16] J. L. Hall, *Nobel lecture: Defining and measuring optical frequencies*, Reviews of Modern Physics **78**, 1279 (2006).

[17] T. W. Hänsch, *Nobel lecture: Passion for precision*, Reviews of Modern Physics **78**, 1297 (2006).

[18] R. Holzwarth, T. Udem, T. W. Hänsch, J. C. Knight, W. J. Wadsworth, and P. S. J. Russell, *Optical frequency synthesizer for precision spectroscopy*, Phys. Rev. Lett. **85**, 2264 (2000).

[19] S. A. Diddams, D. J. Jones, J. Ye, S. T. Cundiff, J. L. Hall, J. K. Ranka, R. S. Windeler, R. Holzwarth, T. Udem, and T. W. Hänsch, *Direct link between microwave and optical frequencies with a 300 thz femtosecond laser comb*, Phys. Rev. Lett. **84**, 5102 (2000).

[20] T. Udem, S. A. Diddams, K. R. Vogel, C. W. Oates, E. A. Curtis, W. D. Lee, W. M. Itano, R. E. Drullinger, J. C. Bergquist, and L. Hollberg, *Absolute Frequency Measurements of*

the Hg^+ and Ca Optical Clock Transitions with a Femtosecond Laser, Phys. Rev. Lett. **86**, 4996 (2001).

[21] A. D. Ludlow, T. Zelevinsky, G. K. Campbell, S. Blatt, M. M. Boyd, M. H. G. de Miranda, M. J. Martin, J. W. Thomsen, S. M. Foreman, J. Ye, T. M. Fortier, J. E. Stalnaker, S. A. Diddams, Y. L. Coq, Z. W. Barber, N. Poli, N. D. Lemke, K. M. Beck, and C. W. Oates, *Sr lattice clock at 1×10^{-16} fractional uncertainty by remote optical evaluation with a Ca clock*, Science **319**, 1805 (2008).

[22] T. Rosenband, D. B. Hume, P. O. Schmidt, C. W. Chou, A. Brusch, L. Lorini, W. H. Oskay, R. E. Drullinger, T. M. Fortier, J. E. Stalnaker, S. A. Diddams, W. C. Swann, N. R. Newbury, W. M. Itano, D. J. Wineland, and J. C. Bergquist, *Frequency ratio of Al^+ and Hg^+ single-ion optical clocks; metrology at the 17th decimal place*, Science **319**, 1808 (2008).

[23] C. W. Chou, D. B. Hume, J. C. J. Koelemeij, D. J. Wineland, and T. Rosenband, *Frequency comparison of two high-accuracy Al^+ optical clocks*, Phys. Rev. Lett. **104**, 70802 (2010).

[24] T. Ido and H. Katori, *Recoil-Free Spectroscopy of Neutral Sr Atoms in the Lamb-Dicke Regime*, Phys. Rev. Lett. **91**, 53001 (2003).

[25] H. Katori, M. Takamoto, V. G. Pal'Chikov, and V. D. Ovsiannikov, *Ultrastable optical clock with neutral atoms in an engineered light shift trap*, Phys. Rev. Lett. **91**, 173005 (2003).

[26] M. Takamoto and H. Katori, *Spectroscopy of the $^1S_0$-$^3P_0$ Clock Transition of ^{87}Sr in an Optical Lattice*, Phys. Rev. Lett. **91**, 223001 (2003).

[27] N. D. Lemke, A. D. Ludlow, Z. W. Barber, T. M. Fortier, S. A. Diddams, Y. Jiang, S. R. Jefferts, T. P. Heavner, T. E. Parker, and C. W. Oates, *Spin-1/2 optical lattice clock*, Phys. Rev. Lett. **103**, 63001 (2009).

[28] J. Lodewyck, P. Westergaard, A. Lecallier, L. Lorini, and P. Lemonde, *Frequency stability of optical lattice clocks*, New Journal of Physics **12**, 065026 (2010).

[29] S. Blatt, A. D. Ludlow, G. K. Campbell, J. W. Thomsen, T. Zelevinsky, M. M. Boyd, J. Ye, X. Baillard, M. Fouché, R. L. Targat, A. Brusch, P. Lemonde, M. Takamoto, F.-L. Hong, H. Katori, and V. V. Flambaum, *New limits on coupling of fundamental constants to gravity using ^{87}Sr optical lattice clocks*, Phys. Rev. Lett. **100**, 140801 (2008).

[30] O. Terra, G. Grosche, K. Predehl, R. Holzwarth, T. Legero, U. Sterr, B. Lipphardt, and H. Schnatz, *Phase-coherent comparison of two optical frequency standards over 146 km using a telecommunication fiber link*, Appl. Phys. B **97**, 541 (2009).

[31] G. Ferrari, P. Cancio, R. E. Drullinger, G. Giusfredi, N. Poli, M. Prevedelli, C. Toninelli, and G. M. Tino, *Precision frequency measurement of visible intercombination lines of strontium*, Phys. Rev. Lett. **91**, 243002 (2003).

[32] M. G. Tarallo, *Development of a Strontium optical lattice clock*. Ph.D. thesis. Università di Pisa, 2009.

[33] M. Takamoto, F. Hong, R. Higashi, and H. Katori, *An optical lattice clock*, Nature **435**, 321–324 (2005).

[34] A. D. Ludlow, *The Strontium Optical Lattice Clock: Optical Spectroscopy with Sub-Hertz Accuracy*. Ph.D. thesis at University of Colorado, 2008.

[35] M. M. Boyd, *High Precision Spectroscopy of Strontium in an Optical Lattice: Towards a New Standard for Frequency and Time*. Ph.D. thesis at University of Colorado, 2007.

[36] X. Baillard, M. Fouché, R. L. Targat, P. G. Westergaard, A. Lecallier, F. Chapelet, M. Abgrall, G. D. Rovera, P. Laurent, P. Rosenbusch, S. Bize, G. Santarelli, A. Clairon, P. Lemonde, G. Grosche, B. Lipphardt, and H. Schnatz, *An optical lattice clock with spin-polarized ^{87}Sr atoms*, The European Physical Journal D **48**, 11 (2008).

[37] T. Legero, J. Winfred, and F. Riehle, *Ultracold ^{88}Sr atoms for an optical lattice clock*, Symposium (2007).

[38] R. F. C. Vessot, M. W. Levine, E. M. Mattison, E. L. Blomberg, T. E. Hoffman, G. U. Nystrom, B. F. Farrel, R. Decher, P. B. Eby, and C. R. Baugher, *Test of relativistic gravitation with a space-borne hydrogen maser*, Phys. Rev. Lett. **45**, 2081 (1980).

[39] C. W. Chou, D. B. Hume, T. Rosenband, and D. J. Wineland, *Optical clocks and relativity*, Science **329**, 1630 (2010).

[40] B. D. Tapley, S. Bettadpur, J. C. Ries, P. F. Thompson, and M. M. Watkins, *Grace measurements of mass variability in the earth system*, Science **305**, 503 (2004).

[41] D. Kleppner, *Time too good to be true*, Physics Today **59**, 10–11 (2006).

[42] G. M. Tino, *Cold atoms physics in space*, Nuclear Physics B-Proceedings Supplements **113**, 289–296 (2002).

[43] G. M. Tino, L. Cacciapuoti, K. Bongs, C. J. Bordé, P. Bouyer, H. Dittus, W. Ertmer, A. Görlitz, M. Inguscio, A. Landragin, P. Lemonde, C. Lammerzahl, A. Peters, E. Rasel, J. Reichel, C. Salomon, S. Schiller, W. Schleich, K. Sengstock, U. Sterr, and M. Wilkens, *Atom interferometers and optical atomic clocks: New quantum sensors for fundamental physics experiments in space*, Nuclear Physics B Proceedings Supplements **166**, 159 (2007).

[44] S. Schiller, A. Görlitz, A. Nevsky, J. C. J. Koelemeij, A. Wicht, P. Gill, H. A. Klein, H. S. Margolis, G. Mileti, U. Sterr, F. Riehle, E. Peik, C. Tamm, W. Ertmer, E. Rasel, V. Klein, C. Salomon, G. M. Tino, P. Lemonde, R. Holzwarth, and T. W. Hänsch, *Optical clocks in space*, Nuclear Physics B Proceedings Supplements **166**, 300 (2007).

[45] L. Cacciapuoti, N. Dimarcq, G. Santarelli, P. Laurent, P. Lemonde, A. Clairon, P. Berthoud, A. Jornod, F. Reina, S. Feltham, and C. Salomon, *Atomic clock ensemble in space: Scientific objectives and mission status*, Nuclear Physics B Proceedings Supplements **166**, 303 (2007).

[46] *http://www.npl.co.uk/upload/pdf/atomic_ clocks_ space.pdf.*

[47] *http://sideshow.jpl.nasa.gov/mbh/series.html*.

[48] S. Schiller, G. M. Tino, P. Gill, C. Salomon, U. Sterr, E. Peik, A. Nevsky, A. Görlitz, D. Svehla, G. Ferrari, N. Poli, L. Lusanna, H. A. Klein, H. S. Margolis, P. Lemonde, P. Laurent, G. Santarelli, A. Clairon, W. Ertmer, E. Rasel, J. Müller, L. Iorio, C. Lämmerzahl, H. Dittus, M. Rothacher, F. Flechner, U. Schreiber, V. Flambaum, W.-T. Ni, L. Liu, X. Chen, J. Chen, K. Gao, L. Cacciapuoti, R. Holzwarth, M. P. Hess, and W. Schäfer, *Einstein gravity explorer-a medium-class fundamental physics mission*, Experimental Astronomy **23**, 573 (2009).

[49] S. Schiller, G. M. Tino, P. Lemonde, U. Sterr, A. Görlitz, N. Poli, A. Nevsky, C. Salomon, and the SOC team, *"The Space Optical Clocks Project", Proc. International Conference on Space Optics, (Rhodes, Greece, 2010), http://www.icsoproceedings.org/.*

[50] M. Schioppo, G. M. Tino, N. Poli, M. G. Tarallo, D. V. Sutyrin, C. Lisdat, J. S. R. V. Winfred, S. Falke, U. Sterr, T. Legero, F. Riehle, and L. Cacciapuoti, *"Development of a transportable laser cooled strontium source for future applications in space", Proceedings of EFTF 2010, http://www.congrex.nl/EFTF_Proceedings/.*

[51] C. Cohen-Tannoudji, *Atomic motion in laser light.* Les Houches Session LIII (1990), Systèmes Fondamentaux en Optique Quantique, Elsevier Science Publishers B.V. (1991).

[52] S. Stenholm, *The semiclassical theory of laser cooling*, Rev. Mod. Phys. **58**, 699 (1986).

[53] C. J.Foot, *Atomic Physics*, Oxford Master Series in Atomic, Optical and Laser Physics, 2006.

[54] W. D. Phillips, H. Metcalf, and H. Metcalf, *Laser deceleration of an atomic beam*, Phys. Rev. Lett. **48**, 596 (1982).

[55] J. V. Prodan, W. D. Phillips, and H. Metcalf, *Laser production of a very slow monoenergetic atomic beam*, Phys. Rev. Lett. **49**, 1149 (1982).

[56] T. W. Hänsch and A. Schawlow, *Cooling of gases by laser radiation*, Opt. Commun. **13**, 68-69 (1975).

[57] S. Chu, L. Hollberg, J. E. Bjorkholm, A. Cable, and A. Ashkin, *Three-dimensional viscous confinement and cooling of atoms by resonance radiation pressure*, Phys. Rev. Lett. **55**, 48 (1985).

[58] H. J. Metcalf and P. van der Straten, *Laser Cooling and Trapping*, Springer-Verlag, New York, 1999.

[59] J. Dalibard and C. Cohen-Tannoudji, *Laser cooling below the doppler limit by polarization gradients: Simple theoretical models*, Journal of the Optical Society of America B: Optical Physics **6**, 2023 (1989).

[60] Y. Castin, H. Wallis, and J. Dalibard, *Limit of doppler cooling*, J. Opt. Soc. Am. B **6**, 2046 (1989).

[61] E. L. Raab, M. Prentiss, A. Cable, S. Chu, and D. E. Pritchard, *Trapping of neutral sodium atoms with radiation pressure*, Physical Review Letters (ISSN 0031-9007) **59**, 2631 (1987).

[62] R. Grimm, M. Weidemüller, and Y. B. Ovchinnikov, *Optical dipole traps for neutral atoms*, Advances In Atomic, Molecular, and Optical Physics **42**, 95-170 (2000).

[63] V. V. Ivanov, A. Alberti, M. Schioppo, G. Ferrari, M. Artoni, M. L. Chiofalo, and G. M. Tino, *Coherent delocalization of atomic wave packets in driven lattice potentials*, Phys. Rev. Lett. **100**, 043602 (2008).

[64] F. Sorrentino, A. Alberti, G. Ferrari, V. V. Ivanov, N. Poli, M. Schioppo, and G. M. Tino, *Quantum sensor for atom-surface interactions below 10 μm*, Phys. Rev. A **79**, 13409 (2009).

[65] G. Ferrari, N. Poli, F. Sorrentino, and G. M. Tino, *Long-lived bloch oscillations with bosonic sr atoms and application to gravity measurement at the micrometer scale*, Phys. Rev. Lett. **97**, 60402 (2006).

[66] N. Poli, R. E. Drullinger, G. Ferrari, M. Prevedelli, F. Sorrentino, M. G. Tarallo, and G. M. Tino, *Prospect for a compact strontium optical lattice clock*, Proc. of SPIE **6673**, 66730F–1 (2007).

[67] M. G. Tarallo, N. Poli, M. Schioppo, D. V. Sutyrin, and G. M. Tino, *A high-stability semiconductor laser system for a ^{88}Sr-based optical lattice clock*, Appl. Phys. B , 445 (2010).

[68] N. Poli, G. Ferrari, M. Prevedelli, F. Sorrentino, R. E. Drullinger, and G. M. Tino, *Laser sources for precision spectroscopy on atomic strontium*, Spectrochimica Acta Part A: Molecular and Biomolecular Spectroscopy **63**, 981–986 (2006).

[69] T. Chanelière, J.-L. Meunier, R. Kaiser, C. Miniatura, and D. Wilkowski, *Extra-heating mechanism in doppler cooling experiments*, J. Opt. Soc. Am. B **22**, 1819 (2005).

[70] H. Katori, T. Ido, Y. Isoya, and M. Kuwata-Gonokami, *Magneto-optical trapping and cooling of strontium atoms down to the photon recoil temperature*, Phys. Rev. Lett. **82**, 1116 (1999).

[71] T. H. Loftus, T. Ido, A. D. Ludlow, M. M. Boyd, and J. Ye, *Narrow line cooling: Finite photon recoil dynamics*, Phys. Rev. Lett. **93**, 73003 (2004).

[72] T. H. Loftus, T. Ido, M. M. Boyd, A. D. Ludlow, and J. Ye, *Narrow line cooling and momentum-space crystals*, Phys. Rev. A **70**, 63413 (2004).

[73] T. Chanelière, L. He, R. Kaiser, and D. Wilkowski, *Three dimensional cooling and trapping with a narrow line*, Eur. Phys. J. D **46**, 507 (2008).

[74] T. Hong, C. Cramer, W. Nagourney, and E. N. Fortson, *Optical clocks based on ultranarrow three-photon resonances in alkaline earth atoms*, Phys. Rev. Lett. **94**, 50801 (2005).

[75] R. Santra, E. Arimondo, T. Ido, C. H. Greene, and J. Ye, *High-accuracy optical clock via three-level coherence in neutral bosonic ^{88}Sr*, Phys. Rev. Lett. **94**, 173002 (2005).

[76] A. V. Taichenachev, V. I. Yudin, C. W. Oates, C. W. Hoyt, Z. W. Barber, and L. W. Hollberg, *Magnetic field-induced spectroscopy of forbidden optical transitions with application to lattice-based optical atomic clocks*, Phys. Rev. Lett. **96**, 83001 (2006).

[77] Z. W. Barber, C. W. Hoyt, C. W. Oates, L. W. Hollberg, A. V. Taichenachev, and V. I. Yudin, *Direct excitation of the forbidden clock transition in neutral ^{174}Yb atoms confined to an optical lattice*, Phys. Rev. Lett. **96**, 83002 (2006).

[78] Z. Barber, *Ytterbium Optical Lattice Clock*. Ph.D. thesis at University of Colorado, 2007.

[79] N. Poli, Z. W. Barber, N. D. Lemke, C. W. Oates, L. S. Ma, J. E. Stalnaker, T. M. Fortier, S. A. Diddams, L. W. Hollberg, J. C. Bergquist, A. Brusch, S. R. Jefferts, T. P. Heavner, and T. E. Parker, *Frequency evaluation of the doubly forbidden $^1S_0 \rightarrow {}^3P_0$ transition in bosonic ^{174}Yb*, Phys. Rev. A **77**, 50501 (2008).

[80] T. Ido, T. H. Loftus, M. M. Boyd, A. D. Ludlow, K. W. Holman, and J. Ye, *Precision Spectroscopy and Density-Dependent Frequency Shifts in Ultracold Sr*, Phys. Rev. Lett. **94**, 153001 (2005).

[81] F. Riehle, J. Ishikawa, and J. Helmcke, *Suppression of a recoil component in nonlinear Doppler-free spectroscopy*, Phys. Rev. Lett. **61**, 2092 (1988).

[82] C. W. Oates, G. Wilpers, and L. Hollberg, *Observation of large atomic-recoil-induced asymmetries in cold atom spectroscopy*, Phys. Rev. A **71**, 23404 (2005).

[83] G. Wilpers, C. Degenhardt, T. Binnewies, A. Chernyshov, F. Riehle, J. Helmcke, and U. Sterr, *Improvement of the fractional uncertainty of a neutral-atom calcium optical frequency standard to 2×10^{-14}*, Appl. Phys. B **76**, 149 (2003).

[84] G. Wilpers, C. W. Oates, and L. Hollberg, *Improved uncertainty budget for optical frequency measurements with microkelvin neutral atoms: Results for a high-stability ^{40}Ca optical frequency standard*, Appl. Phys. B **85**, 31 (2006).

[85] R. H. Dicke, *The effect of collisions upon the doppler width of spectral lines*, Phys. Rev. **89**, 472 (1953).

[86] D. J. Wineland and W. M. Itano, *Laser cooling of atoms*, Phys. Rev. A **20**, 1521 (1979).

[87] D. J. Wineland, W. M. Itano, J. C. Bergquist, and R. G. Hulet, *Laser-cooling limits and single-ion spectroscopy*, Phys. Rev. A **36**, 2220 (1987).

[88] J. C. Bergquist, W. M. Itano, and D. J. Wineland, *Recoilless optical absorption and Doppler sidebands of a single trapped ion*, Phys. Rev. A **36**, 428 (1987).

[89] N. Poli, M. G. Tarallo, M. Schioppo, C. W. Oates, and G. M. Tino, *A simplified optical lattice clock*, Appl. Phys. B **97**, 27 (2009).

[90] N. Poli, M. G. Tarallo, M. Schioppo, C. W. Oates, and G. M. Tino, *An optical lattice clock based on bosonic Sr*, Frequency Control Symposium, 2009 Joint with the 22nd European Frequency and Time forum. IEEE International - DOI: 10.1109/FREQ.2009.5168199 , 347 (2009).

[91] M. Takamoto, F.-L. Hong, R. Higashi, Y. Fujii, M. Imae, and H. Katori, *Improved frequency measurement of a one-dimensional optical lattice clock with a spin-polarized fermionic ^{87}Sr isotope*, J. Phys. Soc. Jpn. **75**, 104302 (2006).

[92] A. Brusch, R. L. Targat, X. Baillard, M. Fouché, and P. Lemonde, *Hyperpolarizability Effects in a Sr Optical Lattice Clock*, Phys. Rev. Lett. **96**, 103003 (2006).

[93] J. A. Armstrong, N. Bloembergen, J. Ducuing, and P. S. Pershan, *Interactions between light waves in a nonlinear dielectric*, Phys. Rev. **127**, 1918 (1962).

[94] P. A. Franken and J. F. Ward, *Optical harmonics and nonlinear phenomena*, Rev. Mod. Phys. **35**, 23 (1963).

[95] J. Dziedzic, *Resonant optical second harmonic generation and mixing*, Quantum Electronics, IEEE Journal of **2**, 109– 124 (2003).

[96] *European STREP Project "Future inertial quantum sensors", NEST-2003-1.*

[97] *ESA MAP Project "Space Atom Interferometry" contract AO-2004-064/082.*

[98] T. Mukaiyama, H. Katori, T. Ido, Y. Li, and M. Kuwata-Gonokami, *Recoil-limited laser cooling of ^{87}Sr atoms near the fermi temperature*, Phys. Rev. Lett. **90**, 113002 (2003).

[99] *K. S. Krane, "Introductory nuclear physics", John Wiley & Sons, New York (1988).*

[100] E. R. Eliel, T. Olsson, L. R. Pendrill, and W. Hogervorst, *High resolution laser spectroscopy of low lying pstates in Sr I and Ba I*, Z. Phys. A. **311** (1983).

[101] X. Xu, T. H. Loftus, J. L. Hall, A. Gallagher, and J. Ye, *Cooling and trapping of atomic strontium*, J. Opt. Soc. Am. B **20**, 968 (2003).